
The Threshold to Prompt Collapse of Binary Neutron Star Mergers - The Effect of Mass Ratio

DISSERTATION

zur Erlangung des akademischen Grades
doctor rerum naturalium (Dr. rer. nat.)



**FRIEDRICH-SCHILLER-
UNIVERSITÄT
JENA**

vorgelegt dem Rat der

PHYSIKALISCH-ASTRONOMISCHEN FAKULTÄT

der

FRIEDRICH-SCHILLER-UNIVERSITÄT JENA

von

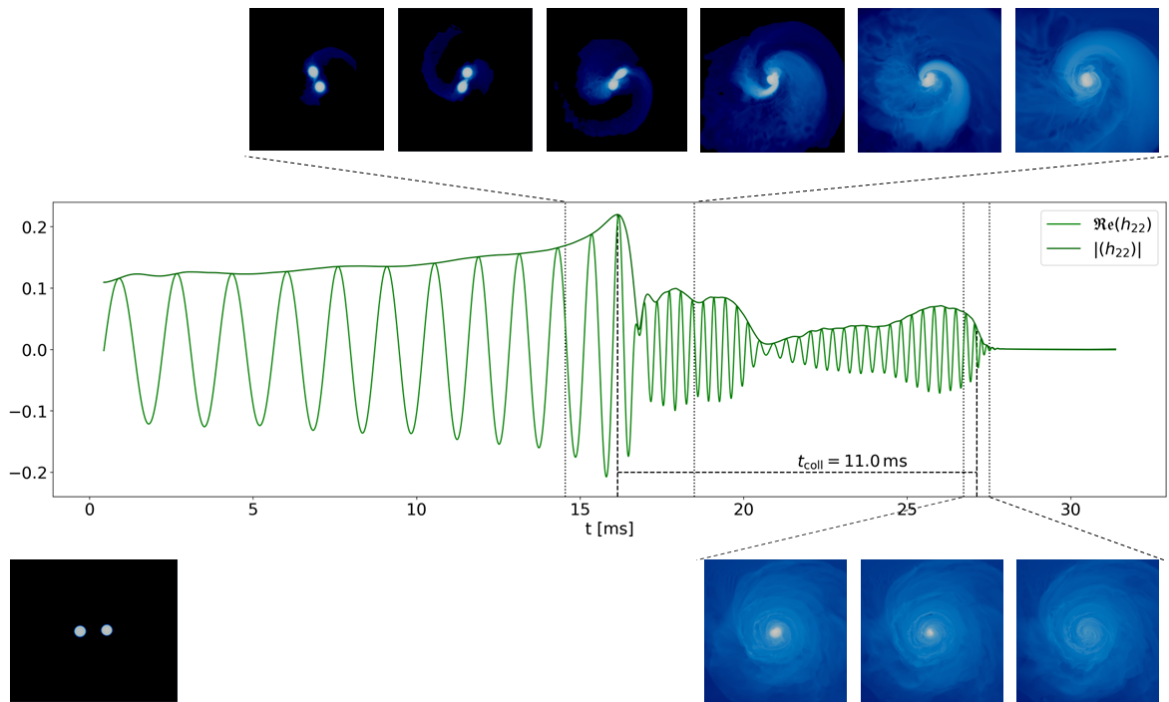
Maximilian Kölsch

geboren am 09.03.1990 in München

GUTACHTER:

1. PROF. DR. BERND BRÜGMANN (FRIEDRICH-SCHILLER-UNIVERSITÄT JENA)
2. PROF. DR. WOLFGANG TICHY (FLORIDA ATLANTIC UNIVERSITY)
3. PD. DR. ANDREAS BAUSWEIN (GSI HELMHOLTZZENTRUM FÜR SCHWERIONEN-
FORSCHUNG GMBH, DARMSTADT)

TAG DER DISPUATATION: 20.04.2023



Simulation of a BNS with $M = 2.8 M_{\odot}$, $q = 1.5$ and EOS ALF2:
 Gravitational wave signal and snapshots of the density ($\log_{10} \varrho$)
 in the case of a BNS merger followed by delayed collapse.
 Snapshots are taken at an early step in the simulation,
 and around the times of merger, and BH formation.
 11 ms after merger the remnant forms a BH,
 causing the ringdown signal to dissipate.

Abbreviations and Notation

Throughout this work, we typically use geometrized units with $c = G = M_{\odot} = 1$. However, in some cases, c , G , M_{\odot} are given explicitly for better understanding. We use Greek letters for four-dimensional indices running from 0 to 3, and Latin letters for three-dimensional indices running from 1 to 3.

The following abbreviations are used throughout the thesis, in most cases these abbreviations are also introduced in the text at their first appearance:

AH	Apparent horizon
ADM	Arnowitt-Deser-Misner
BAM	Bi-functional Adaptive Mesh (code name)
BBH	Binary black hole
BH	Black hole
BHNS	Black hole neutron star
BNS	Binary neutron star
BSSN	Baumgarte-Shapiro-Shibata-Nakamura
EFE	Einstein field equations
EM	Electromagnetic
EOS	Equation of state
GHG	Generalised harmonic gauge
GRHD	General relativistic hydrodynamics
GR	General relativity
GW	Gravitational wave
HMNS	Hypermassive neutron star
ID	Initial data
LIGO	Laser interferometer gravitational-wave observatory
MNS	Massive neutron star
NR	Numerical relativity
NS	Neutron star
pwp	Piecewise-polytropic
SGRB	Short gamma-ray burst

SMNS	Supramassive neutron star
TOV	Tolman-Oppenheimer-Volkoff

Abstract

Direct observations of binary neutron star mergers during the observation runs O2 (GW170817) and O3 (GW190425) of the gravitational-wave detectors Advanced LIGO and Advanced VIRGO raise expectations of numerous future observations with upgraded, more sensitive instruments in O4 and in following observation runs. Future observations of binary neutron star merger events and, in some cases, related multi-messenger observations will provide us with new data covering a variety of source parameters. This will further constrain models, and increase our understanding of dense matter. In this context, general-relativistic simulations of these merger events play a crucial role, not only in the development of gravitational-wave templates, but also in the understanding of the merger process. Subsequently to a binary neutron star coalescence, a black hole can form promptly after merger or with some delay. Dynamics at merger also determine the amount of ejected material that may power post-merger electromagnetic signals. Apart from the total mass of the binary, also the mass ratio can have a major influence on these dynamics, especially in the case of extreme mass ratios. Considering the existing binary neutron star merger observations, mass ratios determined for the sources of GW170817 and GW190425 were found to possibly deviate strongly from the equal-mass case.

In this thesis, we investigate 335 fully relativistic binary neutron star merger simulations, considering 165 different binary configurations, to determine the effect of mass ratio. The studied parameter space covers three equations of state, a broad range of seven mass ratios in the range of $1.0 \leq q \leq 1.75$, and broad ranges of total masses in each case. In our analysis, we are especially interested in mass-ratio effects on the threshold mass to prompt collapse, which separates the cases of prompt and delayed collapse, and in mass-ratio effects on properties of the remnant system. In order to determine the threshold mass, we consider an empirical relation based on the collapse-time, which measures the time interval between merger and collapse to a black hole. Furthermore, we investigate properties of the remnant system, and model effects of mass ratio and equation of state on tidal parameters of threshold configurations.

Contents

1	Introduction	3
2	Gravitational Waves	7
2.1	General Relativity	7
2.2	Linearized Gravity	9
2.3	Degrees of Freedom and Gauge Transformations	10
2.4	Extracting Gravitational Waves from Simulations	12
2.4.1	Newman-Penrose scalar	13
2.4.2	GW Modes	14
2.5	Integration of $r\Psi_4$ data	15
3	Simulation Campaign	19
3.1	BNSs in General-Relativistic Simulations	20
3.1.1	TOV Solution	20
3.1.2	EOSs: Properties, Constraints, Simulations	21
3.1.3	Tidal Polarizability	25
3.2	BNS Configurations and ID	27
3.3	BNS Merger Simulations and Results	31
3.3.1	Dynamical Evolutions with BAM and Clusters	31
3.3.2	Grid Configurations	32
3.3.3	Collapse Types, Properties of the Remnant System, Data	35
4	Threshold to Prompt Collapse	43
4.1	BNS Mergers	43
4.2	Collapse Time	44
4.3	Threshold Mass, Prompt and Delayed Collapse	49
4.3.1	Threshold Mass to Prompt Collapse	49
4.3.2	Prompt and Delayed Collapse in NR Simulations	50
4.3.3	Bracketing Method	51

4.4	Methods Based on Collapse-Time Fits	52
4.4.1	Threshold Collapse Time	53
4.4.2	Collapse-Time Fits	56
4.5	Threshold Mass Coefficient k_{thr}	57
4.6	Collapse Types	58
5	Collapse Time Fits and Threshold Mass	59
5.1	Collapse Time - The Effect of Mass Ratio	59
5.2	M_{thr} by Means of Interpolation of t_{coll} Data	61
5.2.1	Mass Interval	62
5.2.2	Fit Function	62
5.2.3	Fitting Procedure and Results	64
5.2.4	Proof of Principle and Conclusion	66
5.3	Discussion of Collapse-Time Methods	68
5.3.1	Method by Köppel et al.	69
5.3.2	Modification of Köppel's Method	70
5.3.3	Alternative Fitting Procedure	71
6	Modelling Properties of Threshold Configurations	73
6.1	Threshold Mass - The Effect of Mass Ratio	73
6.1.1	Recent Studies	74
6.1.2	Effect of Mass Ratio and Fits	75
6.1.3	Comparison of Results and Fits	77
6.1.4	Fits to Combined Sets of Data	80
6.2	Tidal Polarizability	83
6.3	Properties of Remnant Systems	87
6.3.1	Ejection Mechanisms and Mass-Ratio Effects	87
6.3.2	Remnant Properties - Qualitative Effects	90
6.3.3	Approximating Remnant Properties at Threshold	93
7	Conclusion	97
A	Waveforms, Minimum-Lapse, Maximum-Density	101
B	Stellar Parameters	111
	Additional Material	128

Chapter 1

Introduction

Over the last years, breakthroughs in the research on gravity have received a notable amount of attention - not only in the scientific community, but also among the public sphere. Roughly 100 years after Albert Einstein had published his theory of general relativity (GR) [Einstein, 1915b], which contained the famous Einstein field-equations (EFE) [Einstein, 1915a], and his prediction of the existence of gravitational waves (GW) [Einstein, 1916; Einstein, 1918], GWs were finally detected directly in September 2015 [Abbott et al., 2016]. Only two years later, in October 2017, Rainer Weiss, Barry C. Barish, and Kip S. Thorne were awarded the Nobel prize in physics for the direct detection of GWs. In 2020 yet another Nobel prize was awarded in connection with a phenomenon predicted by Einstein's theory, the existence of Black holes. In both cases, decades of efforts of hundreds of scientists, working in collaboration of both theory and observation, were honoured. Also in both cases, the Nobel prizes followed shortly after long awaited direct observations, that were preceded by indirect measurements and observations of the studied phenomena.

We want to retrace the history of GW detection, starting with the first detection of a pulsar in the year 1967 [Hewish et al., 1968]. A pulsar is the source of extremely regular radio signals. For this discovery, and for the interpretation that pulsars have to be rotating neutron stars (NSs) with extraordinarily strong magnetic fields that accelerate surrounding plasma causing the directed emission of large amounts of energy which can be detected from Earth as radio pulses, Sir Martin Ryle and Antony Hewish were awarded a Nobel prize in 1974. 1974 is also the year when the famous Hulse-Taylor binary was detected [Hulse et al., 1975]. Continued observations over the following decades [e.g. Weisberg et al., 2010] revealed a decline of the orbital period consistent with the loss of energy due to the emission of GWs [e.g. Taylor et al., 1982; Taylor et al., 1989]. For this indirect detection of GWs, Russel A. Hulse and Joseph H. Taylor Jr. were awarded the Nobel prize in physics in 1993.

One year later, in 1994, the National Science Foundation approved for the Laser Interferometer Gravitational-Wave Observatory (LIGO) project [e.g. Abbott et al., 2009] consisting of the two detectors in Hanford and Livingston. At this point, decades of pioneering experimental and theoretical efforts had already been undertaken. In the 2000s, a sequence of initial searches began with ever increasing sensitivity. The initial LIGO interferometers did not detect GW sources. The next generation of advanced interferometers started their first observations run (O1) [Abbott et al., 2019] under the name *Advanced LIGO* in September 2015, making the Nobel prize winning observation of GWs connected to a binary black hole (BBH) merger event shortly before the official start of O1 while the detectors were still in commissioning stage. With repeatedly increased sensitivity, two more observing runs have followed since then, providing many more observations of GWs connected to the coalescences of compact binaries: The O2 observing run (2016, Nov - 2017, Aug) [Abbott et al., 2021a; Abbott et al., 2021b] and the O3 observing run (2019, Apr - 2020, Mar) [Abbott et al., 2021c; Poggiani, 2022]. The observing run O4 is scheduled for March 2023.

During O2, related to the GW event GW170817 [Abbott et al., 2017c], the first multi-messenger observation of a binary NS (BNS) merger [Abbott et al., 2017b] took place, confirming BNS mergers as sources of short gamma-ray burst (SGRBs). In O3, two more events including at least one NS have been observed: the BNS merger event connected to GW190425 [Abbott et al., 2020a], and GWs from the coalescence of a $23 M_{\odot}$ BH with a $2.6 M_{\odot}$ compact object which is among the candidates for being the lightest BH or heaviest NS discovered so far [Abbott et al., 2020b]. In this context, two candidate events for BHNS mergers have to be mentioned: GW200105 and GW200115. Their primaries have masses that are well above the maximum mass of a NS, while their secondary components have masses of $1.9_{-0.2}^{+0.3} M_{\odot}$ and $1.5_{-0.3}^{+0.7} M_{\odot}$, respectively, which are well within the mass range of NSs [Abbott et al., 2021d].

Finding GW signals within the detectors' noise is no trivial task. On the one hand, large amounts of data have to be searched quickly and efficiently. On the other hand, signals can only be found if the search algorithms know what they are looking for. For this purpose accurate templates for the GWs are required. In the regime of sufficiently far separation, the post-Newtonian (PN) expansion can be applied. To extend the realm of validity of PN templates, effective-one-body approaches can be employed [Blanchet, 2014]. Close to merger and beyond, accurate templates are generated conducting GR simulations. Due to the high computational costs of GR simulations on full 3D spatial grids, numerical relativity simulations have only become feasible during

the last decades. In 2005 the first successful simulations of BBH inspirals were performed with the notable feature of GW extraction [Pretorius, 2005; Campanelli et al., 2006; Baker et al., 2006b]. To arrive at these breakthroughs, apart from computational feasibility, many more challenges had to be overcome, particularly with respect to simulations of BBH mergers [cf. Sperhake, 2015]. Concerning the formulation of the Einstein equations for example, the strongly hyperbolic Baumgarte-Shapiro-Shibata-Nakamura (BSSN) formulation, and the symmetric hyperbolic generalised harmonic gauge (GHG) replaced the previously used weakly hyperbolic Arnowitt, Deser and Misner (ADM) formulation [Arnowitt et al., 2008; York, 1978]. The moving puncture method [Campanelli et al., 2006] and improvements concerning the generation of initial data (ID) are among the contributions to the breakthroughs related to BBH simulations [Barack et al., 2019]. Considering simulations of BNSs, the pioneering work connected to the name Shibata [e.g. Shibata, 1999; Shibata et al., 2000b] is worth mentioning. Since the first successful fully general-relativistic simulations of equal-mass [Shibata et al., 2000a], and unequal-mass [Shibata et al., 2003] BNS mergers, where NSs were modelled with polytropic equations of state (EOSs), BNS simulations have improved particularly with respect to the employed EOSs and included physics. In recent works studying BNS mergers by means of relativistic simulations for a variety of EOSs, special consideration was given to the question under which conditions the merger remnant undergoes prompt collapse [e.g. Hotokezaka et al., 2011; Bauswein et al., 2013; Köppel et al., 2019; Bauswein et al., 2021; Tootle et al., 2021; Kashyap et al., 2021; Perego et al., 2021]. This phenomenon depends on properties of the binary, e.g. its total mass, its mass ratio and the components' spins. As stated by Baiotti [Baiotti et al., 2017], BNS mergers are a rich laboratory combining extreme gravity, GWs, electromagnetic (EM) processes and complex microphysics. Since many GW and multi-messenger observations of these events are expected to be observed in the coming observational runs, this laboratory is bound to reveal more about the physics of dense matter in the near future. These observations will further constrain models of dense matter [e.g. Kashyap et al., 2021]. With respect to the analysis of future observations, a clear understanding of the merger process and the possibility of prompt BH formation is important. Possible post-merger signals are affected by the amount of ejected material, which in turn is affected not only by the total mass of the binary, but also by its mass ratio.

In the following thesis, we explore a set of more than 300 general relativistic simulations conducted with the BAM code to investigate mass ratio effects on BNS mergers.

The structure of this thesis is as follows: In chapter 2, we discuss basic concepts of GWs as a phenomenon of GR, their treatment in simulations and post-processing steps employed to determine the GW strain, i.e., a method to integrate $r\Psi_4$ data twice in time. In chapter 3, we discuss properties of NSs and equations of state (EOSs) that are designed to model NS matter. As a tool utilized to compute static models of single NSs, we consider the Tolman-Oppenheimer-Volkoff (TOV) solution of the EFE and discuss constraints on EOSs deduced from astrophysical observations both in the EM and GW spectrum. Afterwards, we introduce our simulation campaign, discussing its composition, listing properties of the considered BNS configurations and presenting results of simulations presented in Ref. [Koe1]. In this context, we introduce some of the architecture of the BAM code and discuss the employed numerical resolutions.

In chapter 4, we consider BNS mergers, discussing possible scenarios with regards to the fate of the merger remnant. Focussing on the cases of prompt and delayed collapse, we discuss relevant definitions and criteria. Two important quantities in this context are the collapse time (t_{coll}) which measures the time between merger and collapse, and the threshold mass to prompt collapse (M_{thr}) which separates the cases of prompt and delayed collapse. Analysing our simulation results, we investigate the relationship of these quantities to define a threshold collapse time. This definition will allow us to determine M_{thr} by means of a new method which we introduce in chapter 5. This method is based on a fit of collapse time data and M_{thr} is determined by means of interpolation. In chapter 5, we describe the fitting procedure in detail. We compare our method to an existing method which is also based on a fit of collapse-time data. In the context of this method, M_{thr} is determined by means of extrapolation following a different definition of the threshold mass. As we shall show, these definitions are not equivalent. For further testing of our method, we compare it to the bracketing method. We conclude this chapter with the discussion of an idea for an alternative method.

In chapter 6, we model mass-ratio effects, starting with the threshold mass and tidal polarizability parameters. We discuss and refine existing models. In the case of M_{thr} , we also prepare fits of combined data sets basing them on a broader set of EOSs. After a discussion of mass-ratio effects on merger dynamics, we consider effects on properties of the remnant system consisting of a BH and a disk.

Chapter 2

Gravitational Waves

2.1 General Relativity

Einstein's theory of gravity unifies space, time, mass and energy. Gravitation is described as a geometric property of spacetime, which as a mathematical model fuses space and time in a four-dimensional manifold. The geometric properties of a spacetime are subject to any form of contained mass or energy. Due to Einstein's famous equation $E = mc^2$ mass and energy can be used equivalently. When we talk about geometric properties of spacetime, we think of curvature in terms of the metric $g_{\mu\nu}$ or the related line element

$$ds^2 = g_{\mu\nu} dx^\mu dx^\nu . \quad (2.1)$$

How spacetime has to behave in the presence of mass (energy), or reversely how matter has to behave in curved spacetime, is specified by a system of non-linear partial differential equations, the Einstein field equations (EFE),

$$R_{\mu\nu} - \frac{1}{2} g_{\mu\nu} R = 8\pi T_{\mu\nu} . \quad (2.2)$$

The right-hand side of Eq. (2.2) is proportional to the energy-momentum tensor $T_{\mu\nu}$, which describes the density and flux of energy and momentum of the matter model. The left-hand side of the EFE consists of the metric $g_{\mu\nu}$ and the metric-dependent tensors $R_{\mu\nu}$ and R . Let us quickly go through the related definitions without diving too deeply into the mathematical technicalities: The Ricci tensor $R_{\mu\nu}$ and the Ricci scalar R are defined by

$$R_{\mu\nu} = R^\lambda{}_{\mu\lambda\nu} \quad (2.3)$$

$$R = g^{\mu\nu} R_{\mu\nu} , \quad (2.4)$$

i.e., they are contractions of the Riemann tensor $R^\rho_{\sigma\mu\nu}$ which in turn is defined by

$$R^\rho_{\sigma\mu\nu} = \partial_\mu \Gamma^\rho_{\nu\sigma} - \partial_\nu \Gamma^\rho_{\mu\sigma} + \Gamma^\rho_{\mu\lambda} \Gamma^\lambda_{\nu\sigma} - \Gamma^\rho_{\nu\lambda} \Gamma^\lambda_{\mu\sigma} , \quad (2.5)$$

where $\Gamma^\rho_{\mu\nu}$ are the Christoffel symbols (or connection coefficients) given by

$$\Gamma^\rho_{\mu\nu} = \frac{1}{2} g^{\rho\lambda} (\partial_\mu g_{\nu\lambda} + \partial_\nu g_{\lambda\mu} - \partial_\lambda g_{\mu\nu}) . \quad (2.6)$$

There is only a small number of exact solutions to the EFE known - corresponding to very special cases characterized by high symmetry. One of these, to give an example, is the Schwarzschild metric [Schwarzschild, 1916] which, according to Birkhoff's theorem, is the unique spherically-symmetric and static vacuum solution to the EFE. The Schwarzschild metric describes the gravitational field outside a spherically symmetric and irrotational mass, e.g. a static black hole (BH). Typically, the Schwarzschild metric is presented in spherical coordinates $\{t, r, \theta, \phi\}$, where the line element takes the form

$$ds^2 = - \left(1 - \frac{2GM}{r}\right) dt^2 + \left(1 - \frac{2GM}{r}\right)^{-1} dr^2 + r^2 d\Omega^2 . \quad (2.7)$$

If we went one step back to retrace a possible derivation of the Schwarzschild solution, we may start off with the assumption of spherical symmetry, i.e. without demanding the metric to be static. However, it can be shown that the assumption of spherical symmetry already implies the metric to be static, and we may write it in the form

$$ds^2 = -e^{2\alpha(r)} dt^2 + e^{2\beta(r)} dr^2 + r^2 d\Omega^2 , \quad (2.8)$$

cf. for example Carroll, 2019. Therefore, Birkhoff's theorem also states that there are no time-dependent solutions of this form. With the additional assumption of vacuum, and by comparison to the weak-field limit, we may determine the variables $\alpha(r)$ and $\beta(r)$ in Eq. (2.8) such that we arrive at Eq. (2.7). Considering cosmological implications, Einstein added a parameter to his equations (2.2), to allow for static models of the universe. Later he removed it. In present cosmological models, this so-called cosmological constant is employed again - to model the accelerated expansion of the universe implied by observations. If we consider Einstein's theory of gravity in the limit of weak gravitational fields and static spacetimes, Newtonian physics are recovered. Assuming fields to be weak, but allowing for variations in time, Einstein's theory predicts phenomena such as gravitational lensing and gravitational waves (GW).

2.2 Linearized Gravity

In the presence of weak gravitational fields, spacetime is locally almost flat. Therefore, the metric can be decomposed into the flat Minkowski metric $\eta_{\mu\nu}$ and a small perturbation $h_{\mu\nu}$, i.e.,

$$g_{\mu\nu} = \eta_{\mu\nu} + h_{\mu\nu} , \quad (2.9)$$

with $|h_{\mu\nu}| \ll 1$. Ignoring terms of higher than first order in $h_{\mu\nu}$, we use $\eta_{\mu\nu}$ and $\eta^{\mu\nu}$ to raise and lower indices, and obtain

$$g^{\mu\nu} = \eta^{\mu\nu} - h^{\mu\nu} , \quad (2.10)$$

for the inverse metric and

$$\Gamma_{\mu\nu}^{\rho} = \frac{1}{2}\eta^{\rho\lambda} (\partial_{\mu}h_{\nu\lambda} + \partial_{\nu}h_{\lambda\mu} - \partial_{\lambda}h_{\mu\nu}) \quad (2.11)$$

for the Christoffel symbols. Since the Christoffel symbols are of first order, we will ignore quadratic contributions of the $\Gamma_{\mu\nu}^{\rho}$ to the Riemann tensor $R_{\mu\nu\rho\sigma}$. To first order, we obtain

$$R_{\mu\nu\rho\sigma} = \frac{1}{2} (\partial_{\rho}\partial_{\nu}h_{\mu\sigma} + \partial_{\sigma}\partial_{\mu}h_{\nu\rho} - \partial_{\sigma}\partial_{\nu}h_{\mu\rho} - \partial_{\rho}\partial_{\mu}h_{\nu\sigma}) \quad (2.12)$$

$$R_{\mu\nu} = \frac{1}{2} (\partial_{\lambda}\partial_{\nu}h^{\lambda}_{\mu} + \partial_{\lambda}\partial_{\mu}h^{\lambda}_{\nu} - \partial_{\mu}\partial_{\nu}h - \square h_{\nu\sigma}) \quad (2.13)$$

$$R = \partial_{\mu}\partial_{\nu}h^{\mu\nu} - \square h \quad (2.14)$$

$$G_{\mu\nu} = \frac{1}{2} (\partial_{\lambda}\partial_{\nu}h^{\lambda}_{\mu} + \partial_{\lambda}\partial_{\mu}h^{\lambda}_{\nu} - \partial_{\mu}\partial_{\nu}h - \square h_{\mu\nu} - \eta_{\mu\nu}\partial_{\rho}\partial_{\lambda}h^{\rho\lambda} - \eta_{\mu\nu}\square h) \quad (2.15)$$

for the Riemann tensor and for its contractions, the Ricci tensor and the Ricci scalar, and for the Einstein tensor

$$G_{\mu\nu} = R_{\mu\nu} - \frac{1}{2}\eta_{\mu\nu}R , \quad (2.16)$$

respectively. In Eqs. (2.13) to (2.15) h is the trace of the perturbation

$$h = \eta^{\mu\nu}h_{\mu\nu} , \quad (2.17)$$

and \square is the flat-space d'Alembertian $\square = -\partial_t^2 + \partial_x^2 + \partial_y^2 + \partial_z^2$.

2.3 Degrees of Freedom and Gauge Transformations

Seeking to determine the degrees of freedom of the metric perturbation $h_{\mu\nu}$, we consider transformations of the form

$$h_{\mu\nu} \rightarrow h_{\mu\nu} + 2\partial_{(\mu}\xi_{\nu)} \quad (2.18)$$

which are called gauge transformations. Eq. (2.18) shows the transformation of the metric perturbation $h_{\mu\nu}$ under an infinitesimal diffeomorphism along a small vector field ξ^μ . It can easily be shown that the Riemann tensor (2.12) is invariant with respect to this kind of transformation, i.e., the curvature of the physical spacetime remains unchanged. Referring the interested reader to chapter seven of Carroll, 2019, for a thorough derivation of the transformation in Eq. (2.18), we continue investigating the remaining degrees of freedom. Adopting the notation and following the approach presented in Carroll, 2019, further, we decompose $h_{\mu\nu}$ into its 00-component, its $0i$ -components, and its ij -components:

$$h_{00} = -2\Phi \quad (2.19)$$

$$h_{0i} = \omega_i \quad (2.20)$$

$$h_{ij} = 2s_{ij} - 2\Psi\delta_{ij} , \quad (2.21)$$

with

$$\Psi = -\frac{1}{6}\delta^{ij}h_{ij} \quad (2.22)$$

$$s_{ij} = \frac{1}{2} \left(h_{ij} - \frac{1}{3}\delta^{kl}h_{kl}\delta_{ij} \right) . \quad (2.23)$$

In Eq. (2.21), h_{ij} is written as the sum of a trace-term (Eq. (2.22)), and the symmetric and trace-free spatial tensor s_{ij} (Eq. (2.23)), i.e., $Tr(s_{ij}) = 0$. The tensor s_{ij} is called the *strain*. In this notation the linearized Einstein equations can be written as

$$\nabla^2\Psi = 4\pi GT_{00} - \frac{1}{2}\partial_k\partial_l s^{kl} \quad (2.24)$$

$$(\delta_{jk}\nabla^2 - \partial_j\partial_k)\omega^k = -16\pi GT_{0j} + 4\partial_0\partial_j\Psi + 2\partial_0\partial_k s_j^k \quad (2.25)$$

$$\begin{aligned} (\delta_{ij}\nabla^2 - \partial_i\partial_j)\Phi &= 8\pi GT_{ij} + (\delta_{ij}\nabla^2 - \delta_i\delta_j - 2\delta_{ij}\partial_0^2)\Psi \\ &\quad - \delta_{ij}\partial_0\partial_k\omega^k + \partial_0\partial_{(i}\omega_{j)} \\ &\quad + \square s_{ij} - 2\partial_k\partial_{(i}s_{j)}^k - \delta_{ij}\partial_k\partial_l s^{jl} \end{aligned} \quad (2.26)$$

Considering the system of equations (2.24) to (2.26), we find the propagating degrees of freedom to be those of the strain tensor s_{ij} , since Ψ can be determined from T_{00} and s_{ij} (cf. Eq. (2.24)), and ω^i can be determined from T_{0j} , Ψ and s_{ij} (cf. Eq. (2.25)). Taking into account its symmetric and traceless properties, we find s_{ij} to have 5 independent components. Considering that under a gauge transformation of the form given by Eq. (2.18), the quantities $(\Phi, \omega, \Psi, s_{ij})$ transform as

$$\Phi \rightarrow \Phi + \partial_0 \xi^0 \quad (2.27)$$

$$\omega_i \rightarrow \omega_i + \partial_0 \xi^i - \partial_i \xi^0 \quad (2.28)$$

$$\Psi \rightarrow \Psi - \frac{1}{3} \partial_i \xi^i \quad (2.29)$$

$$s_{ij} \rightarrow s_{ij} + \partial_{(i} \xi_{j)} - \frac{1}{3} \partial_k \xi^k \delta_{ij} , \quad (2.30)$$

we find that 3 of the 5 independent components of s_{ij} are subject to gauge transformations. Therefore, we count 2 propagating degrees of freedom for the strain tensor. To make these degrees of freedom visible in a GW solution, we are going to solve the system of equations (2.24) to (2.26), under the conditions of the so-called transverse-trace gauge. To that end, we demand the vectorfield χ^μ to satisfy the conditions

$$\nabla^2 \xi^j + \frac{1}{3} \partial_j \partial_i \xi^i = -2 \partial_i s^{ij} \quad \nabla^2 \xi^0 = \partial_i \omega^i + \partial_0 \partial_i \xi^i , \quad (2.31)$$

rendering s_{ij} and ω^i to be transverse, i.e.,

$$\partial_i s^{ij} = 0 \quad \partial_i \omega^i = 0 . \quad (2.32)$$

Under these conditions and the additional assumption of vacuum, i.e., $T_{\mu\nu} = 0$, the EFE ((2.24) to (2.26)) take the form

$$\nabla^2 \Psi = 0 \quad (2.33)$$

$$-\nabla^2 \omega^k - 4 \partial_0 \partial_j \Psi = 0 \quad (2.34)$$

$$(\delta_{ij} \nabla^2 - \partial_i \partial_j) (\Phi - \Psi) - \partial_0 \partial_{(i} \omega_{j)} + 2 \delta_{ij} \partial_0^2 \Psi - \square s_{ij} = 0 . \quad (2.35)$$

Solving the first two equations under the assumption of well-behaved boundary conditions, we obtain $\Psi = 0$ and therefore, $\omega_j = 0$, together with

$$(\delta_{ij} \nabla^2 - \partial_i \partial_j) \Phi - \square s_{ij} = 0 . \quad (2.36)$$

Exploiting that s_{ij} is traceless while taking the trace of Eq. (2.36), we deduce $\Phi = 0$ and therefore, $\square s_{ij} = 0$, or equivalently

$$\square h_{\mu\nu}^{\text{TT}} = 0. \quad (2.37)$$

Solving this equation with the plane-wave ansatz $h_{\mu\nu}^{\text{TT}} = C_{\mu\nu} e^{ik_\sigma x^\sigma}$ and considering a wave propagating in x^3 -direction, we eventually arrive at the famous GWs solution

$$h_{\mu\nu}^{\text{TT}} = \begin{pmatrix} 0 & 0 & 0 & 0 \\ 0 & h_+ & h_\times & 0 \\ 0 & h_\times & -h_+ & 0 \\ 0 & 0 & 0 & 0 \end{pmatrix}, \quad (2.38)$$

where h_+ and h_\times carry the two degrees of freedom. The notation h_+ and h_\times is chosen with respect to the individual effects that each part of the solution would have on a ring of test masses located in the x_1, x_2 plane: In the case $h_\times = 0$, the ring would be deformed periodically in direction of the x_1 and x_2 axes, being elongated in one direction while being squeezed in the other. In the case $h_+ = 0$, same behaviour would be observed in directions diagonal to those axes.

2.4 Extracting Gravitational Waves from Simulations

For the purpose of performing general-relativistic simulations, spacetime is decomposed in what is called the 3+1 formalism. The key idea of this formalism is the foliation of spacetime by a family of spacelike hypersurfaces, transforming the EFE into a Cauchy problem, that allows for the evolution of initial data in time, cf. for example Gourgoulhon, 2007. In this context, the concepts of lapse and shift by J. A. Wheeler play an important role. The lapse α and the shift β are measures of the time lapse and the shift of coordinates between spatial slices (cf. for example Fig. 2 of Centrella et al., 2010). They represent coordinate freedoms of the metric. Due to this freedom, different slicing conditions may be applied to the lapse function, for example for the purpose of avoiding singularities. One possible formulation of the EFE in terms of 3+1 formalism is the one presented by Arnowitt, Deser and Misner (ADM), Arnowitt et al., 2008, or their reformulation by York, 1978. However, as investigated by Kidder et al., 2001, the ADM equations are a formulation of the EFE that is only weakly hyperbolic. An improved system of equations, called the BSSNOK (or just

BSSN) formalism, allowing long term stable evolutions was introduced by Baumgarte et al., 1998, and Shibata et al., 1995. With respect to the simulations performed for this thesis, we name one more evolution system: The Z4c formalism introduces constraint damping terms into the system of equations that cause a reduction of constraint violations by between one and two orders of magnitude compared to simulations with BSSN, cf. Bernuzzi et al., 2010, and Hilditch et al., 2013. These efforts to improve the evolution system eventually led to the first stable binary black hole simulations that allowed for the extraction of convergent gravitational waveforms, cf. for example Fiske et al., 2005, and Baker et al., 2006a.

2.4.1 Newman-Penrose scalar

The Newman-Penrose scalar, or Weyl scalar, Ψ_4 is one out of five complex scalars, which can be formed by contractions of the Weyl tensor ${}^{(4)}C_{\mu\nu\rho\sigma}$ defined as

$$\begin{aligned} {}^{(4)}C_{\mu\nu\rho\sigma} = & {}^{(4)}R_{\mu\nu\rho\sigma} - \frac{1}{2} \left({}^{(4)}R_{\mu\rho} g_{\nu\sigma} - {}^{(4)}R_{\mu\sigma} g_{\nu\rho} + {}^{(4)}R_{\nu\sigma} g_{\mu\rho} - {}^{(4)}R_{\nu\rho} g_{\mu\sigma} \right) \\ & + \frac{1}{6} (g_{\mu\rho} g_{\nu\sigma} - g_{\mu\sigma} g_{\nu\rho}) {}^{(4)}R , \end{aligned} \quad (2.39)$$

with a complex null tetrad, l^μ , n^μ , m^μ , \bar{m}^μ . These vectors are chosen to satisfy orthogonality and normalization conditions,

$$l^\mu m_\mu = 0 = n^\mu m_\mu , \quad -l^\mu n_\mu = 1 = m^\mu \bar{m}_\mu . \quad (2.40)$$

Together the scalars, $\Psi_0 \dots \Psi_4$, cover the 10 independent components of the four-dimensional Weyl tensor, which can be expressed in terms of these scalars, cf. Newman et al., 1962. The Newman-Penrose scalar Ψ_4 is defined by

$$\Psi_4 = - {}^{(4)}C_{\mu\nu\rho\sigma} n^\mu \bar{m}^\nu n^\rho \bar{m}^\sigma , \quad (2.41)$$

which is equivalent to

$$\Psi_4 = - {}^{(4)}R_{\mu\nu\rho\sigma} n^\mu \bar{m}^\nu n^\rho \bar{m}^\sigma . \quad (2.42)$$

In a special subset of *transverse frames*, called *quasi-Kinnersley frames*, cf. Kinnersley, 1969, Ψ_4 measures the outgoing gravitational radiation, cf. for example Baumgarte et

al., 2010. In terms of the 3+1 decomposition of the EFE, Eq. (2.42) becomes

$$\Psi_4 = \left[{}^{(4)}R_{ijkl} + 2K_{i[k}K_{l]j} \right] n^i \bar{m}^j n^k \bar{m}^l \quad (2.43)$$

$$- 8 \left[K_{j[k,l]} + \Gamma_{j[k}^m K_{l]m} \right] n^{[0} \bar{m}^{j]} n^k \bar{m}^l \quad (2.44)$$

$$+ 4 \left[R_{jl} + K_{jm} K_l^m + K K_{jl} \right] n^{[0} \bar{m}^{j]} n^{[0} \bar{m}^{l]} , \quad (2.45)$$

cf. Baker et al., 2002. In the preceding equation, K_{ij} is the extrinsic curvature tensor

$$K_{\mu\nu} = -\gamma_\mu^\rho \gamma_\nu^\sigma \nabla_\rho n_\sigma , \quad (2.46)$$

with n^μ being the timelike normal vector, and $\gamma_{\mu\nu}$ being the spatial metric on a 3-dimensional hypersurface, cf. for example Baumgarte et al., 2010.

2.4.2 GW Modes

Following the approach taken in Brüggmann et al., 2008, we consider spin-weighted spherical harmonics Y_{lm}^s , as a means to determine modes A_{lm} of GWs by projection, i.e., evaluation of the scalar product

$$A_{lm} = \langle Y_{lm}^s, \Psi_4 \rangle = \int_0^{2\pi} \int_0^\pi \Psi_4 Y_{lm}^s \sin\theta d\theta d\phi . \quad (2.47)$$

Here $s = -2$, since Ψ_4 transforms as spin-weight -2 field, e.g. Maggiore, 2007. The spin-weighted spherical harmonics Y_{lm}^s are defined as

$$Y_{lm}^s(\vartheta, \varphi) = (-1)^s \sqrt{\frac{2l+1}{4\pi}} d_{m(-s)}^l(\vartheta) e^{im\varphi} , \quad (2.48)$$

where $d_{m(-s)}^l$ are Wigner d -functions

$$d_{m(-s)}^l(\vartheta) = \sum_{t=C_1}^{C_2} \frac{(-1)^t [(l+m)!(l-m)!(l+s)!(l-s)!]}{(l+m-t)!(l-s-t)!t!(t+s-m)!} \quad (2.49)$$

$$(\cos\vartheta/2)^{2l+m-s-2t} (\sin\vartheta/2)^{2t+s-m} , \quad (2.50)$$

with $C_1 = \max(0, m-s)$ and $C_2 = \min(l+m, l-s)$. Since Ψ_4 falls off as $1/r$,¹ often the product $r\Psi_4$ is considered instead of Ψ_4 , evaluated at high finite radius to

¹In the general case, Ψ_n falls off as r^{n-5} , cf. for example Bishop et al., 2016.

approximate the limit of $r \rightarrow \infty$, i.e., the case of a detector at large distance from the source.

2.5 Integration of $r\Psi_4$ data

We calculate the gravitational wave strain h from Ψ_4 data, considering only the dominant 22-mode, cf. Fig. 2.2, and utilizing the method of fixed frequency integration (FFI) from Ref. Reisswig et al., 2011. The FFI method reduces secular non-linear drifts in h that arise due to finite length and discrete sampling of the signal when integrating Ψ_4 twice in time, cf. Fig. 2.1. In the first and second panel of Fig. 2.1, we compare the FFI method to the naive integration utilizing Simpson's rule, applying both methods to $r\Psi_4$ data of a BNS merger simulation (EOS ALF2, $q = 1.25$, $M = 2.8M_\odot$). The results obtained with Simpson's rule do not oscillate about zero. Depending on the choice of the integration constants c_1 and c_2 of the first and second time integration, we may find drifts at the early or late times, cf. panels one and two of Fig. 2.1. Reisswig et al., 2011, integrate a Fourier-transformed signal, cutting off unphysical low-frequency components:

$$\tilde{F}(\omega) = \begin{cases} -i\tilde{f}(\omega)/\omega_0, & \omega \leq \omega_0 \\ -i\tilde{f}(\omega)/\omega, & \omega > \omega_0 \end{cases}. \quad (2.51)$$

Integrating twice, we obtain

$$\tilde{h}(\omega) = \begin{cases} -\tilde{\Psi}_4(\omega)/\omega_0^2, & \omega \leq \omega_0 \\ -\tilde{\Psi}_4(\omega)/\omega^2, & \omega > \omega_0 \end{cases}. \quad (2.52)$$

In the third panel of Fig. 2.1, we compare the FFI method to the naive integration without filtering of low frequencies. In the case of unfiltered integration, we find drifts at early and late times. Furthermore, the amplitude $|h_{22}^{\text{unfiltered}}(t)|$ oscillates about the result obtained with FFI. In the case of the 22-mode, we filter out frequencies lower than initial orbital frequency ω_{orbit} , i.e., $\omega_0 = \omega_{\text{orbit}}$. In the presented examples, the GW signal is shifted with respect to the observer position r_{extr} , i.e., we use the retarded time

$$u = t - r_* = t - r_{\text{extr}} - 2M \ln\left(\frac{r_{\text{extr}}}{2M} - 1\right), \quad (2.53)$$

cf. Dietrich et al., 2017. Here, the observer is located at $r_5 \approx 1034$ km.

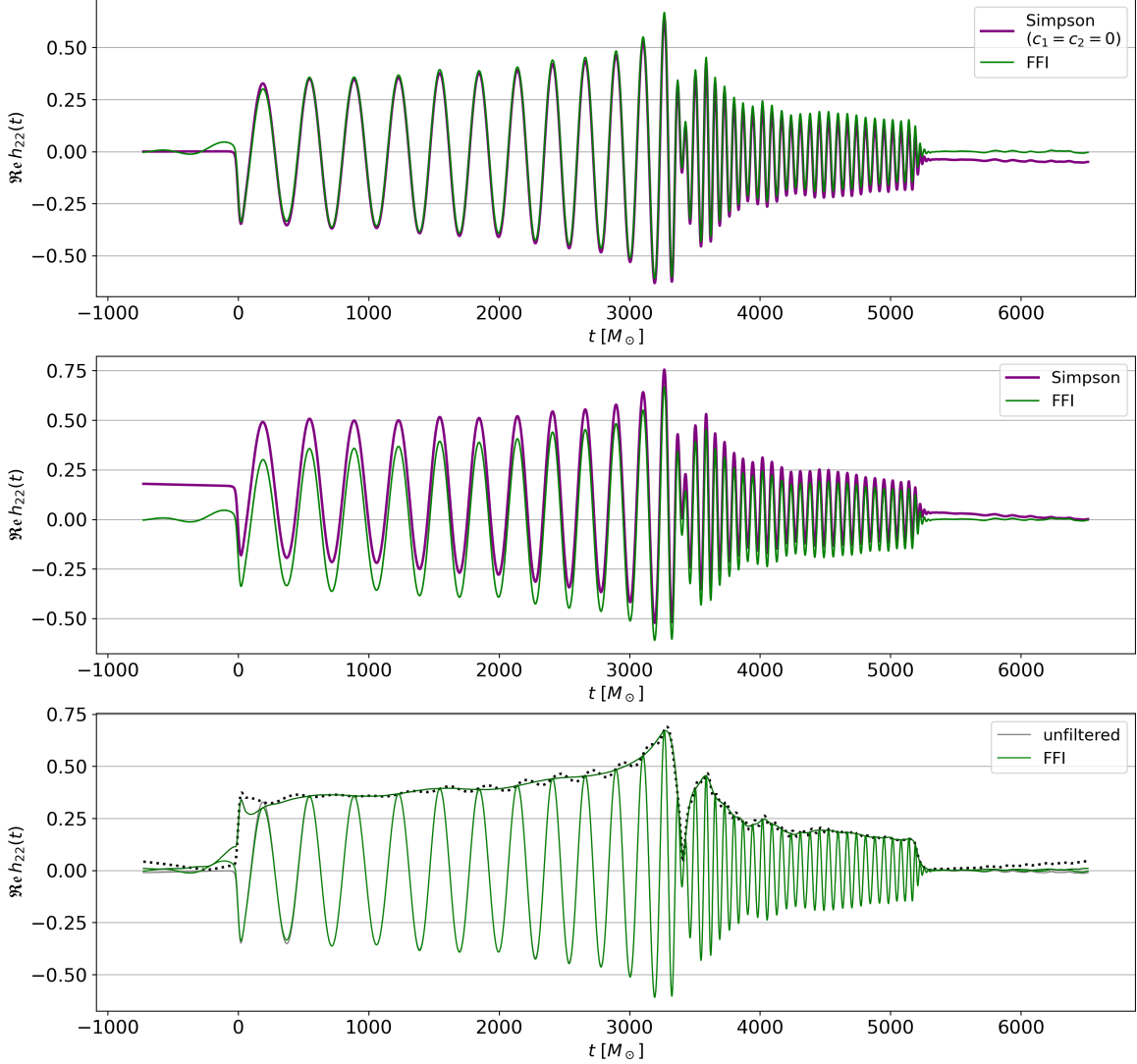


Figure 2.1: Real part of the 22-mode of the strain amplitude $h(t)$ calculated by means of different methods: Simpson's rule, frequency fixed integration, unfiltered integration of Fourier transformed Ψ_4 data, which stem from a BNS simulation with EOS ALF2, mass ratio $q = 1.25$, and total mass $M = 2.8 M_\odot$. In the upper panel, the frequency fixed integration is compared to the integration by Simpson's rule. Due to non-linear drift in the time-domain integration, the signal calculated by application of Simpson's rule does not oscillate about zero at late times. In the middle panel, a similar situation is presented: the integration constants are chosen such that the signal is zero at late times. This procedure leads to notable drift at early times. In the lower panel, the frequency fixed integration is compared to the naive integration of the Fourier transform where low frequencies are not filtered. In the case of the unfiltered integration, the amplitude $|h_{22}^{\text{unfiltered}}(t)|$ (dotted line) exhibits oscillations and drifts at early and late times.

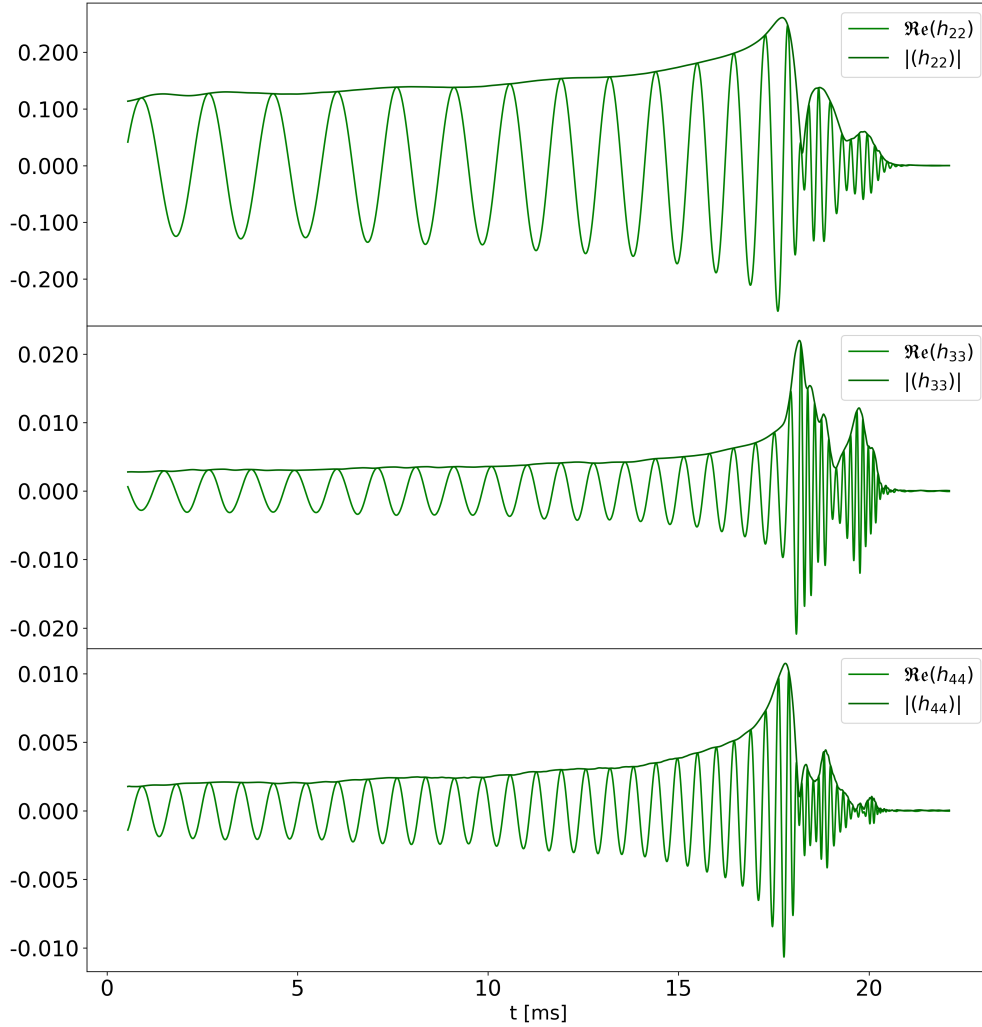


Figure 2.2: Sample of modes of the strain amplitude $h(t)$ with $l = m$. Depicted are the 22, 33 and 44 modes of the GW signal belonging to a BNS merger simulation with EOS SLy, $q = 1.25$ and $M = 2.8 M_{\odot}$. The signal is shifted in accordance with Eq. 2.53. The maximal amplitude decreases notably in the case of modes with $l > 2$.

Chapter 3

Simulation Campaign

In this thesis, we consider 335 relativistic simulations of BNSs conducted with the BAM code [Bernuzzi et al., 2016a; Dietrich et al., 2015b; Thierfelder et al., 2011; Brüggmann et al., 2008], for a total of 165 BNS configurations to study the effect of mass ratio on the threshold mass [cf. Chap. 5] and on properties of the remnant system [cf. Chap. 6]. The associated initial data (ID) exclusively include binaries of irrotational NSs. They have been constructed with the SGRID code [Tichy et al., 2019; Dietrich et al., 2015a; Tichy, 2009b; Tichy, 2009a; Tichy, 2006]. 295 of the considered simulations (145 BNS configurations) are part the simulation campaign of Ref. [Koe1], they will accompany us through this and the following chapters. These simulations cover a parameter space spanned by three equations of state (EOS) and seven mass ratios. In each case defined by a pair of parameters (EOS, q), a suitable range of total masses is considered. For one of these cases, namely ALF2 with $q = 1.5$, we have conducted 40 additional simulations of 20 configurations. We analyse this smaller set of simulations thoroughly in Chap. 4, examining the interesting regime close to threshold. The larger set of simulations is evaluated in Sects. 5 and 6. Our simulations were performed on HAWK at the High-Performance Computing Center Stuttgart (HLRS) and on the ARA cluster of the University of Jena. Depending on the numerical resolution, the BAM simulations took between one and several weeks to complete. In the case of ID construction the usual runtime was four to five days.

In this chapter, we examine EOSs selected for the simulation campaign of Ref. [Koe1], i.e., SLY, ALF2 and H4, in Sect. 3.1. For the characterization of EOSs, we consider properties of single TOV stars (e.g. maximum mass, mass-radius relations, or compactness) and properties of binary systems (e.g. tidal interaction). We discuss these properties in the light of recent constraints on the unknown EOS of nuclear matter, reviewing findings of studies conducted subsequently to the observations of

GW170817 and GW190425. With regard to the configurations considered in the simulation campaign, a broad set of characteristic properties is provided in Sect. 3.2. In Sect. 3.3, we discuss the process of conducting BNS-merger simulations with BAM, taking a glance at the employed strategies and numerical methods. Illustrating the chosen numerical setup, we take a closer look at the structure of BAM's numerical grid. Leaving the detailed analysis of the simulation data for later chapters, we conclude this chapter with a presentation of results in Figs. 3.5 and 3.6, and Tabs. 3.7 to 3.9.

3.1 BNSs in General-Relativistic Simulations

3.1.1 TOV Solution

The most simple general-relativistic model of a neutron star is the Tolman-Oppenheimer-Volkoff (TOV) solution. It can be derived presuming spherical symmetry (which already implies that the spacetime is static, cf. discussion in Sect. 2.1) and assuming for the matter to behave like a perfect fluid. Here, we will focus to the main steps, referring the interested reader to Carroll, 2019, for a detailed derivation. Inserting the metric of a spherically symmetric spacetime, Eq. (2.8), and the energy momentum tensor of a perfect fluid

$$T_{\mu\nu} = (\varrho + p) U_\mu U_\nu + p g_{\mu\nu} , \quad (3.1)$$

with ϱ , p and U^μ being the energy density, the pressure and the four-velocity, respectively, into the Einstein equations, Eq. (2.2), we obtain three independent equations. These are related to the components G_{tt} , G_{rr} and $G_{\theta\theta}$ (respectively $G_{\phi\phi}$) of the Einstein tensor. Employing the tt equation, the rr equations and the energy-momentum conservation $\nabla_\mu T^{\mu\nu} = 0$, we arrive at the TOV equation, Oppenheimer et al., 1939,

$$\frac{dp}{dr} = - \frac{(\varrho + p) [Gm(r) + 4\pi Gr^3 p]}{r [r - 2Gm(r)]} , \quad (3.2)$$

where $m(r)$ is defined as

$$m(r) = 4\pi \int_0^r \varrho(r') r'^2 dr' . \quad (3.3)$$

These equations only build a closed system in connection with an equation of state (EOS), $p = p(\varrho, T, S, \dots)$, which relates state variables. Here, the minimal set consists of the variables pressure and density, i.e.

$$p = p(\varrho) . \quad (3.4)$$

3.1.2 EOSs: Properties, Constraints, Simulations

EOSs are models which describe the state of matter under given physical conditions. In the case of dense NS matter, it is impossible to experimentally recreate conditions present in NSs in a laboratory on earth. Therefore, models of dense NS matter have to be tested with respect to astrophysical observations. Observations in the electromagnetic spectrum, GW and multi-messenger observations¹ put constraints on the yet unknown EOS of NSs. Constraints can also be inferred from heavy-ion collision experiments, cf. for example Danielewicz et al., 2002; Russotto et al., 2016. Models of NS matter may be based on different assumptions and theoretical approaches. To give an example, EOSs may be build upon different assumption concerning the dominant constituents of the NS core, e.g. nucleons, hyperons, pions or kaon condensates, cf. for example Read et al., 2009.

As indicated in the previous section, at the least pressure and density need to be set into relation to model NS matter. Usually, thermal effects can be neglected as the temperature of NSs is far below their constituent particles' Fermi energy, e.g. Read et al., 2009. EOSs that neglect influences of temperature are called zero-temperature EOSs. In BNS simulations, this description of NS matter becomes problematic after merger when temperatures above several tens of MeV are reached, cf. for example discussion by Köppel et al., 2019. This problem can be solved by the addition of a thermal pressure contribution

$$p_{\text{th}} = (\Gamma_{\text{th}} - 1) \rho \epsilon , \quad (3.5)$$

with an adiabatic constant of $\Gamma_{\text{th}} = 1.75$, cf. Shibata et al., 2005; Bauswein et al., 2010. The quantities ρ and ϵ are the rest-mass density and the specific internal energy, respectively. A simple example of zero-temperature EOSs are polytropic models

$$p = K \rho^\gamma . \quad (3.6)$$

Another model is given by the TOV solution with the extreme assumption of constant density throughout the NS. It provides an interesting relation with respect to the maximal mass that a NS may have. Given a radius R , the mass of a spherically

¹GW observations of BNSs Abbott et al., 2017c; Abbott et al., 2020a, Kilonova and GRB afterglow measurements of GW170817, e.g. Abbott et al., 2017a; Coughlin et al., 2019; Coughlin et al., 2018, X-ray measurements performed by the NICER [Neutron Star Interior Composition Explorer], cf. Miller et al., 2019; Riley et al., 2019; Miller et al., 2021; Riley et al., 2021,

symmetric object of that radius is constrained by

$$M_{\max} = \frac{4}{9G}R . \quad (3.7)$$

According to Buchdahl’s law, Buchdahl, 1959, any solution of the TOV equation has to obey the inequality

$$M_{\max} < \frac{4}{9G}R . \quad (3.8)$$

The maximum mass M_{\max} is an important characteristic of NS EOSs, which has to be compatible with observational data, e.g. masses determined from observations of massive radio pulsars, cf. Antoniadis et al., 2013; Arzoumanian et al., 2018; Fonseca et al., 2021. The most massive pulsars observed have masses of about $2 M_{\odot}$. According to Abbott et al., 2018, the maximum TOV mass is constrained by $M_{\max} > 1.97 M_{\odot}$. In Ref. [Koe1] and in this work, we employ three EOSs, i.e. SLy, ALF2, and H4 for our simulations. Their maximum masses, $2.06 M_{\odot}$, $1.99 M_{\odot}$, and $2.03 M_{\odot}$, respectively, are compatible with this constraint.

Table 3.1: Sample of properties characterizing the EOSs studied in this work, ordered by stiffness. Columns from left to right: M_{\max} and R_{\max} are the gravitational mass and radius of the maximum-mass TOV star. $R_{1.4}$ and $R_{1.6}$ are the radii of single $1.4 M_{\odot}$ and $1.6 M_{\odot}$ TOV stars, respectively. $C_{\max} = (GM_{\max})/(c^2 R_{\max})$ is the compactness of the maximum-mass TOV configuration and $C_{1.6}^* = (GM_{\max})/(c^2 R_{1.6})$ an alternative formula for the compactness as given by Bauswein et al., 2013. $\Lambda_{1.4}$ is the tidal deformability coefficient of a single $1.4 M_{\odot}$ star. Table taken from [Koe1].

EOS	M_{\max} [M_{\odot}]	R_{\max} [km]	$R_{1.6}$ [km]	$R_{1.4}$ [km]	C_{\max}	$C_{1.6}^*$	$\Lambda_{1.4}$	Literature
SLy	2.06	9.91	11.46	11.37	0.307	0.268	306.7	Douchin et al., 2001
ALF2	1.99	11.30	12.38	12.41	0.260	0.237	590.6	Alford et al., 2005
H4	2.03	11.62	13.54	13.46	0.258	0.223	885.6	Lackey et al., 2006

Associated with the NS radius, different stellar parameters are used to characterize an EOS. Typically, these are the radii of TOV stars with $M = 1.4 M_{\odot}$ and $1.6 M_{\odot}$, i.e., $R_{1.4}$ and $R_{1.6}$, and the radius of the maximum mass configuration R_{\max} . The radii of TOV stars constructed with SLy, ALF2, and H4 are reported in Tab. 3.1. In the case of $1.4 M_{\odot}$ stars these are 11.46 km, 12.38 km, and 13.54 km, respectively. For detailed information about the considered EOS models we refer to the references in column nine of Tab. 3.1. In Ref. [Koe1], we claim that the chosen EOSs are broadly compatible with recent maximum mass and radius constraints, referring to a sample

of studies that were conducted subsequently to the observations of GW170817 and GW190425, i.e., Bauswein et al., 2017; Annala et al., 2018; Most et al., 2018; Abbott et al., 2018; Radice et al., 2019; Capano et al., 2020; Dietrich et al., 2020; Legred et al., 2021; Miller et al., 2021; Raaijmakers et al., 2021; Huth et al., 2021. We are going to take a closer look at some of the mass and radius constraints determined in these studies, starting with Bauswein et al., 2017, who find constraints

$$R_{1.6} \geq 10.68_{-0.04}^{+0.15} \text{ km} , \quad R_{\text{max}} \geq 9.60_{-0.03}^{+0.14} \text{ km} \quad (3.9)$$

based on a lower estimate of the threshold mass (M_{thr} , cf. Sect. 4.3.1)

$$M_{\text{thr}} \geq 1.23 M_{\text{max}} , \quad (3.10)$$

determined in connection with the total mass measured for GW170817, see for example Abbott et al., 2017c, and a causal relation between M_{max} and R_{max}

$$M_{\text{max}} \leq \frac{1}{2.82} \frac{c^2 R_{\text{max}}}{G} \quad (3.11)$$

cf. Koranda et al., 1997; Lattimer et al., 2016. With respect to constraints on the tidal deformability $\tilde{\Lambda}$ associated with GW170817 (at a credence level of 90%), Annala et al., 2018, infer constraints on the radius of a $1.4 M_{\odot}$ NS, i.e.,

$$9.9 \text{ km} < R_{1.4} < 13.6 \text{ km} . \quad (3.12)$$

Similar, yet stricter constraints have been determined by Radice et al., 2019, who find the 90% credible interval to be

$$R_{1.4} = 12.2_{-0.8}^{+1.0} \text{ km} . \quad (3.13)$$

Although they indicate additional 0.2 km of systematic uncertainty, these tighter limits do not enclose the respective radius of H4 by a narrow margin. In defense of this EOS, we may put forward that Radice et al., 2019, expect higher systematic errors in association with an extension of their set of EOSs, which they consider large but still limited. In any case, we should consider H4 an extreme case, especially if we also consider its high tidal polarizability, that is higher than recent constraints, e.g. $\Lambda_{1.4} < 800$ according to Most et al., 2018, or Annala et al., 2018. Considering the $\Lambda_{1.4}$ values of our EOSs, we point out that a reasonably large range of tidal polarizabilities

is considered. According to a study by Radice et al., 2018b, both H4 and SLy are excluded EOSs with respect to constraints on the tidal parameter $\tilde{\Lambda}$ (cf. Sect. 3.1.3) inferred from the multi-messenger observations related to GW170817. Other works see the lower constraints on the tidal deformability of NSs at significantly lower levels, e.g. Annala et al., 2018 or Kashyap et al., 2021 with $\Lambda_{1.4} > 172$.

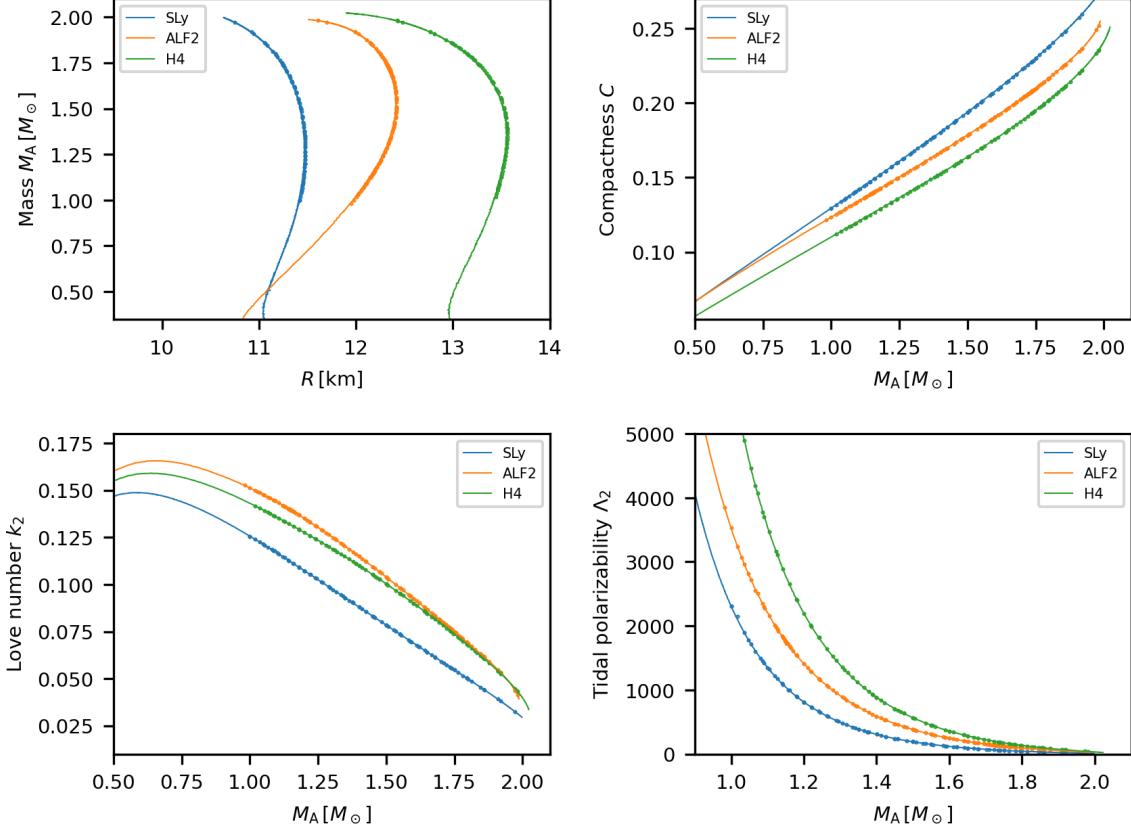


Figure 3.1: Properties of EOSs used within this thesis. Points mark components (TOV stars) of simulated binaries with varying mass ratio. Presented are relations between a single star’s mass M_A and its radius R (upper left), its compactness (upper right), the respective Love numbers k_2 (lower left) and the tidal polarizability Λ_2 (lower right). Plot in the lower right taken from [Koe1].

With respect to GW and multi-messenger observations of BNS mergers, future BNS merger events are expected to constrain another characteristic of the NS EOS: the threshold mass to prompt collapse. Following the coalescence of a BNS, the remnant may immediately collapse to a BH if its total mass exceeds this threshold mass, cf. Sect. 4.3. With respect to the two existing BNS merger observations, the threshold mass is directly constrained by the multi-messenger observations connected to GW170817, Abbott et al., 2017b, and the highly likely observation of a prompt-collapse merger

associated with GW190425, Abbott et al., 2020a, i.e.,

$$2.74_{-0.01}^{+0.04} M_{\odot} < M_{\text{thr}} < 3.3_{-0.1}^{+0.1} M_{\odot} . \quad (3.14)$$

Under the assumption that the final remnant associated with GW170817 was a BH [e.g. Margalit et al., 2017; Ruiz et al., 2018; Shibata et al., 2017], Rezzolla et al., 2018, have narrowed the maximum-mass constraint to

$$2.01_{-0.04}^{+0.04} M_{\odot} \leq M_{\text{max}} \leq 2.16_{-0.15}^{+0.17} M_{\odot} . \quad (3.15)$$

Regarding the use of EOSs in simulations, i.e., for the construction of ID, or in dynamical evolutions, EOSs are either implemented in tabulated form or as piecewise-polytropic (pwp) fits. In connection with simulations presented in this chapter, two codes were employed: SGRID (ID) and BAM (dynamical evolutions). In both cases, the treatment of EOSs is based on pwp fits determined by Read et al., 2009. These four-parameter fits consist of three polytropic pieces, defined by three adiabatic indices and Eq. (3.6), with the first dividing density as a fourth parameter. Characteristic quantities presented in Tab. 3.1 are computed based on these fits using a workframe created by Bernuzzi and Nagar.² The curves in Fig. 3.1 are determined in the same manner. Presented are the mass-radius relations, the compactness, and tidal quantities k_2 and Λ_2 as functions of a single NS's mass.

3.1.3 Tidal Polarizability

The emission of GWs in the late phase of BNS inspiral is influenced by tidal interactions of the involved NSs, and hence their tidal properties. A measure for a NS's response to external quadrupolar fields \mathcal{E}_{ij} is the constant Λ . Up to linear order it relates \mathcal{E}_{ij} to the quadrupole moment Q_{ij} developed in response to the external field, i.e.,

$$Q_{ij} = -\lambda \mathcal{E}_{ij} . \quad (3.16)$$

In the literature λ is sometimes referred to as the tidal Love number, sometimes this name is reserved for the dimensionless quantity k_2 which is related to λ by

$$k_2 = \frac{3G}{2R^5} \lambda . \quad (3.17)$$

²Matlab code solving TOV equations in GR, <https://bitbucket.org/bernuzzi/tov/src/master/>, based on Bernuzzi et al., 2008; Damour et al., 2009

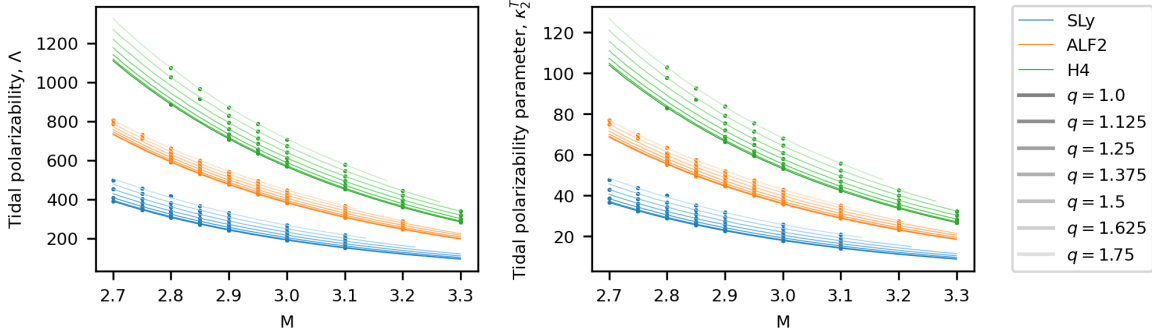


Figure 3.2: Tidal polarizability parameters $\tilde{\Lambda}$ (first column) and κ_2^{T} (second column) of EOSs used within this thesis. For each EOS the tidal polarizability parameters as a functions of M are given for a sample of seven mass-ratios, marked from dark ($q = 1$) to light ($q = 1.75$). In the case of high mass ratios, the allowed range of M is constraint by the condition, $M_1 < M_{\text{max}}$, where M_1 is the mass of the more massive component. Points mark simulated BNS configurations. $\kappa_2^{\text{T}}(M)$ and $\tilde{\Lambda}(M)$ are monotonously decreasing functions.

Tidal interactions in compact binaries can be treated as fundamental non-radial $l = 2$ oscillations, regarding the NSs as forced, damped harmonic oscillators, cf. for example Zhao et al., 2022; Damour et al., 2009; Bernuzzi et al., 2008; Flanagan et al., 2008; Hinderer, 2008. Love numbers k_2 of the EOSs considered in Ref. [Koe1], are reported in the lower left panel of Fig. 3.1. From the Love numbers and the compactness $C = GM_{\text{A}}/(R_{\text{A}}c^2)$ of a NS, we determine the quadrupolar tidal polarizability parameter

$$\Lambda_2^{\text{A}} = \frac{2}{3}k_2^{\text{A}} \left(\frac{c^2 R_{\text{A}}}{G M_{\text{A}}} \right)^5 = \frac{2}{3}k_2^{\text{A}} C^{-5}, \quad (3.18)$$

of a NS with mass M_{A} and radius R_{A} , e.g. Bernuzzi, 2020; Damour et al., 2010. Λ_2^{A} is a measure for the stiffness of a NS. In Tab. 3.1, taking $\Lambda_{1.4}$, i.e., the tidal polarizability of a $1.4M_{\odot}$ star as a reference, EOSs are ordered descending from soft to stiff with respect to their stiffness. With respect to the tidal polarizability of BNSs, we consider the quantities, κ_2^{T} and $\tilde{\Lambda}$, defined as

$$\kappa_2^{\text{T}} = \frac{3}{2} (\Lambda_2^{\text{A}} X_{\text{A}}^4 X_{\text{B}} + \Lambda_2^{\text{B}} X_{\text{B}}^4 X_{\text{A}}) \quad (3.19)$$

$$\tilde{\Lambda} = \frac{16}{13} (X_{\text{A}} + 12X_{\text{B}}) X_{\text{A}}^4 \Lambda_2^{\text{A}} + (\text{A} \leftrightarrow \text{B}) \quad (3.20)$$

with $X_{\text{A}} = M_{\text{A}}/M$, e.g., Bernuzzi, 2020. In Fig. 3.2, κ_2^{T} and $\tilde{\Lambda}$ are given for mass ratios considered in this work (lines). The tidal polarizability parameters $\tilde{\Lambda}$ and κ_2^{T} of the considered binary configurations (points) stretch over a broad range. They depend primarily on the total mass of the binary, secondarily there is a systematic effect of

the mass ratio. For given M , the tidal parameters increase with increasing q .³ $\tilde{\Lambda}$ and κ_2^{T} are decreasing functions of M .

3.2 BNS Configurations and ID

In this section, we consider the 145 configurations of Ref. [Koe1]. These configurations cover a parameter space spanned by three EOSs (SLy, ALF2, H4), seven mass ratios ($q \in \{1.0, 1.125, 1.25, 1.375, 1.5, 1.625, 1.75\}$), and adapted ranges of total masses. In the case of ALF2 and $M = 2.8 M_{\odot}$, three additional configurations were simulated, to examine $t_{\text{coll}}(q)$ at intermediate mass ratios, i.e., $q \in \{1.3125, 1.4375, 1.5625\}$. Usually six to seven configurations of varying total mass are considered per case of given EOS and mass ratio. In total these are 46, 55, and 44 configurations in the cases of SLy, ALF2, and H4, respectively, cf. Tabs. 3.2 to 3.4.

The business of constructing ID containing binaries in GR is not trivial. Due to the non-linearity of the EFE, solutions cannot simply be superposed. Consequently, properties of the binary's components are not unambiguously defined. In SGRID the single-star masses are estimated from an integral resembling the ADM mass computation, and running over only one star, cf. Tichy et al., 2019. Similarly, quantities like linear or angular momentum need to be estimated. Preparing ID, the SGRID code has been our weapon of choice. All of the considered configurations contain binaries of irrotational NSs with an initial separation of $16 M_{\odot}$ ($\approx 23.6 \text{ km}$) on quasi-circular orbits with residual eccentricities of the order of 10^{-2} , cf. column five of Tabs. 3.7 to 3.9. Saving computational resources and due to the short inspiral, we did not apply any additional eccentricity reduction. In the dynamical evolutions, with respect to the EOS, the mass ratio and the total mass, the chosen initial separation does not always lead to the same number of orbits, N_{orbit} , up to merger. In almost all cases a minimal number of $N_{\text{orbit}} \gtrsim 4$ has been reached. To find an initial separation corresponding to this requirement, and parameter settings for SGRID that provide quasi-circular orbits, we have conducted a set of test simulations which are not listed in the following. Properties of the considered binaries and their individual components are given in Tabs. 3.2 to 3.4.

³ $\tilde{\Lambda}$ and κ_2^{T} depend on the total mass, and on the component's individual masses M_i and tidal polarizability coefficients Λ_2^i , cf. Eqs. (3.20) and (3.19). In regions, where the compactness C and Love numbers k_2 are approximately linear in M_A , cf. Fig. 3.1, this dependence can be estimated to be roughly of the form $Z_{\text{tidal}} \approx a \cdot q + b/q + c$, with $Z_{\text{tidal}} \in \{\tilde{\Lambda}, \kappa_2^{\text{T}}\}$.

Table 3.2: BNS configurations with EOS SLy. Mass ratio q and total mass M (columns two and three) directly determine the gravitational masses, M_1 and M_2 , of the stars (columns four and five). The chirp mass $\mathcal{M} = (M_1 M_2)^{3/5} / M^{1/5}$ of the binary is given in column six. The baryonic masses, M_1^b and M_2^b (columns seven and eight), as well as the radii, R_1 and R_2 (columns nine and ten), of the individual stars are provided by SGRID. The stars' compactnesses, C_1 and C_2 (columns eleven and twelve), are calculated as $C_i = (GM_i)/(c^2 R_i)$. The tidal polarizability quantities, $\Lambda_2^{(1)}$, $\Lambda_2^{(2)}$, $\tilde{\Lambda}$ and κ_2^T (columns thirteen to sixteen), are calculated using formulas (3.18) to (3.20). Table taken from Ref. [Koe1].

EOS	q	M [M_\odot]	M_1 [M_\odot]	M_2 [M_\odot]	\mathcal{M} [M_\odot]	M_1^b [M_\odot]	M_2^b [M_\odot]	R_1 [km]	R_2 [km]	C_1	C_2	$\Lambda_2^{(1)}$	$\Lambda_2^{(2)}$	$\tilde{\Lambda}$	κ_2^T
SLy	1.000	2.70	1.350	1.350	1.175	1.495	1.495	11.47	11.47	0.1738	0.1738	389	389	389	36.5
SLy	1.000	2.75	1.375	1.375	1.197	1.526	1.526	11.47	11.47	0.1771	0.1771	345	345	345	32.3
SLy	1.000	2.80	1.400	1.400	1.219	1.557	1.557	11.46	11.46	0.1804	0.1804	307	307	307	28.8
SLy	1.000	2.85	1.425	1.425	1.241	1.588	1.588	11.46	11.46	0.1837	0.1837	272	272	272	25.5
SLy	1.000	2.90	1.450	1.450	1.262	1.620	1.620	11.45	11.45	0.1870	0.1870	242	242	242	22.7
SLy	1.000	3.00	1.500	1.500	1.306	1.683	1.683	11.43	11.43	0.1938	0.1938	191	191	191	17.9
SLy	1.000	3.10	1.550	1.550	1.349	1.747	1.747	11.41	11.41	0.2007	0.2007	151	151	151	14.1
SLy	1.125	2.75	1.456	1.294	1.195	1.627	1.426	11.45	11.48	0.1878	0.1665	235	511	351	32.9
SLy	1.125	2.80	1.482	1.318	1.216	1.661	1.455	11.44	11.48	0.1914	0.1696	207	455	311	29.2
SLy	1.125	2.85	1.509	1.341	1.238	1.695	1.484	11.43	11.47	0.1950	0.1726	183	405	276	25.9
SLy	1.125	2.90	1.535	1.365	1.260	1.729	1.513	11.42	11.47	0.1986	0.1757	161	363	246	23.1
SLy	1.125	3.00	1.588	1.412	1.303	1.797	1.572	11.38	11.46	0.2060	0.1819	125	290	194	18.2
SLy	1.125	3.10	1.641	1.459	1.347	1.867	1.631	11.35	11.45	0.2136	0.1882	97	233	154	14.4
SLy	1.250	2.70	1.500	1.200	1.167	1.683	1.312	11.43	11.47	0.1938	0.1545	191	813	409	38.5
SLy	1.250	2.75	1.528	1.222	1.188	1.719	1.338	11.42	11.48	0.1976	0.1573	167	727	364	34.3
SLy	1.250	2.80	1.556	1.244	1.210	1.755	1.365	11.40	11.48	0.2015	0.1601	147	651	323	30.5
SLy	1.250	2.85	1.583	1.267	1.231	1.791	1.392	11.39	11.48	0.2054	0.1630	128	583	288	27.1
SLy	1.250	2.90	1.611	1.289	1.253	1.827	1.419	11.37	11.48	0.2093	0.1659	112	523	256	24.1
SLy	1.250	3.00	1.667	1.333	1.296	1.900	1.474	11.32	11.48	0.2174	0.1716	86	422	203	19.2
SLy	1.250	3.10	1.722	1.378	1.339	1.975	1.529	11.27	11.47	0.2257	0.1774	65	341	161	15.2
SLy	1.375	2.75	1.592	1.158	1.179	1.802	1.261	11.38	11.47	0.2066	0.1491	123	999	381	36.0
SLy	1.375	2.80	1.621	1.179	1.200	1.840	1.286	11.36	11.47	0.2107	0.1518	107	901	340	32.2
SLy	1.375	2.85	1.650	1.200	1.222	1.878	1.312	11.34	11.47	0.2149	0.1545	93	813	304	28.8
SLy	1.375	2.90	1.679	1.221	1.243	1.917	1.337	11.31	11.48	0.2192	0.1572	81	731	271	25.7
SLy	1.375	3.00	1.737	1.263	1.286	1.995	1.388	11.25	11.48	0.2280	0.1625	60	594	216	20.5
SLy	1.375	3.10	1.795	1.305	1.329	2.074	1.439	11.17	11.48	0.2372	0.1680	45	484	173	16.4
SLy	1.500	2.70	1.620	1.080	1.147	1.839	1.169	11.36	11.45	0.2106	0.1393	108	1,499	452	42.9
SLy	1.500	2.75	1.650	1.100	1.168	1.878	1.192	11.34	11.45	0.2149	0.1418	93	1,349	403	38.3
SLy	1.500	2.80	1.680	1.120	1.189	1.918	1.216	11.31	11.46	0.2194	0.1444	80	1,218	361	34.3
SLy	1.500	2.85	1.710	1.140	1.211	1.958	1.240	11.28	11.46	0.2239	0.1469	69	1,101	323	30.7
SLy	1.500	2.90	1.740	1.160	1.232	1.999	1.264	11.25	11.47	0.2285	0.1494	59	993	289	27.5
SLy	1.500	3.00	1.800	1.200	1.274	2.081	1.312	11.17	11.47	0.2381	0.1545	43	813	232	22.1
SLy	1.500	3.10	1.860	1.240	1.317	2.165	1.360	11.06	11.48	0.2484	0.1596	31	666	186	17.7
SLy	1.625	2.75	1.702	1.048	1.156	1.948	1.131	11.29	11.44	0.2227	0.1353	72	1,784	429	40.9
SLy	1.625	2.80	1.733	1.067	1.177	1.990	1.153	11.26	11.45	0.2275	0.1377	61	1,601	382	36.5
SLy	1.625	2.85	1.764	1.086	1.198	2.032	1.176	11.22	11.45	0.2323	0.1400	52	1,453	343	32.8
SLy	1.625	2.90	1.795	1.105	1.219	2.074	1.198	11.17	11.46	0.2373	0.1424	44	1,321	309	29.6
SLy	1.625	3.00	1.857	1.143	1.261	2.161	1.243	11.07	11.46	0.2479	0.1472	31	1,083	249	23.8
SLy	1.625	3.10	1.919	1.181	1.303	2.249	1.289	10.92	11.47	0.2595	0.1521	22	893	201	19.3
SLy	1.750	2.70	1.750	1.000	1.143	2.013	1.075	11.24	11.42	0.2301	0.1293	56	2,311	499	47.8
SLy	1.750	2.75	1.750	1.000	1.143	2.013	1.075	11.24	11.42	0.2301	0.1293	56	2,311	455	43.6
SLy	1.750	2.80	1.782	1.018	1.164	2.056	1.096	11.19	11.43	0.2351	0.1316	48	2,150	418	40.1
SLy	1.750	2.85	1.814	1.036	1.184	2.100	1.118	11.14	11.44	0.2404	0.1339	40	1,896	367	35.2
SLy	1.750	2.90	1.845	1.055	1.205	2.144	1.139	11.09	11.44	0.2458	0.1361	34	1,720	330	31.7
SLy	1.750	3.00	1.909	1.091	1.247	2.235	1.182	10.95	11.45	0.2576	0.1407	23	1,418	267	25.7
SLy	1.750	3.10	1.973	1.127	1.288	2.327	1.225	10.75	11.46	0.2711	0.1453	15	1,173	217	20.9

Table 3.3: Same as Tab. 3.2, but for ALF2. Table taken from Ref. [Koe1].

EOS	q	M [M_\odot]	M_1 [M_\odot]	M_2 [M_\odot]	\mathcal{M} [M_\odot]	M_1^b [M_\odot]	M_2^b [M_\odot]	R_1 [km]	R_2 [km]	C_1	C_2	$\Lambda_2^{(1)}$	$\Lambda_2^{(2)}$	$\tilde{\Lambda}$	κ_2^T
ALF2	1.0000	2.80	1.400	1.400	1.219	1.549	1.549	12.39	12.39	0.1669	0.1669	589	589	589	55.3
ALF2	1.0000	2.85	1.425	1.425	1.241	1.579	1.579	12.40	12.40	0.1697	0.1697	529	529	529	49.6
ALF2	1.0000	2.90	1.450	1.450	1.262	1.610	1.610	12.41	12.41	0.1726	0.1726	475	475	475	44.5
ALF2	1.0000	2.95	1.475	1.475	1.284	1.641	1.641	12.41	12.41	0.1755	0.1755	427	427	427	40.0
ALF2	1.0000	3.00	1.500	1.500	1.306	1.672	1.672	12.42	12.42	0.1784	0.1784	381	381	381	35.8
ALF2	1.0000	3.10	1.550	1.550	1.349	1.735	1.735	12.42	12.42	0.1844	0.1844	307	307	307	28.8
ALF2	1.0000	3.20	1.600	1.600	1.393	1.798	1.798	12.41	12.41	0.1904	0.1904	246	246	246	23.1
ALF2	1.1250	2.80	1.482	1.318	1.216	1.650	1.448	12.42	12.34	0.1763	0.1577	414	843	594	55.8
ALF2	1.1250	2.85	1.509	1.341	1.238	1.683	1.477	12.42	12.36	0.1794	0.1603	367	760	532	50.0
ALF2	1.1250	2.90	1.535	1.365	1.260	1.716	1.506	12.42	12.37	0.1826	0.1629	328	687	479	45.0
ALF2	1.1250	2.95	1.562	1.388	1.281	1.750	1.534	12.42	12.38	0.1858	0.1656	292	621	430	40.3
ALF2	1.1250	3.00	1.588	1.412	1.303	1.783	1.563	12.41	12.39	0.1890	0.1682	259	560	385	36.2
ALF2	1.1250	3.10	1.641	1.459	1.347	1.851	1.621	12.39	12.41	0.1956	0.1736	204	458	310	29.1
ALF2	1.1250	3.20	1.694	1.506	1.390	1.919	1.680	12.36	12.42	0.2024	0.1791	159	372	248	23.3
ALF2	1.2500	2.80	1.556	1.244	1.210	1.742	1.361	12.42	12.28	0.1850	0.1497	300	1,155	601	56.6
ALF2	1.2500	2.85	1.583	1.267	1.231	1.777	1.387	12.41	12.30	0.1884	0.1521	265	1,054	543	51.1
ALF2	1.2500	2.90	1.611	1.289	1.253	1.812	1.414	12.41	12.32	0.1918	0.1545	234	954	487	45.9
ALF2	1.2500	2.95	1.639	1.311	1.275	1.848	1.441	12.40	12.34	0.1953	0.1570	206	868	439	41.3
ALF2	1.2500	3.00	1.667	1.333	1.296	1.884	1.468	12.38	12.35	0.1988	0.1594	181	786	394	37.1
ALF2	1.2500	3.10	1.722	1.378	1.339	1.956	1.522	12.34	12.38	0.2062	0.1644	140	650	319	30.0
ALF2	1.2500	3.20	1.778	1.422	1.383	2.028	1.576	12.28	12.40	0.2138	0.1694	106	536	257	24.2
ALF2	1.3125	2.80	1.589	1.211	1.205	1.784	1.320	12.41	12.25	0.1891	0.1460	258	1,344	609	57.4
ALF2	1.3750	2.80	1.621	1.179	1.200	1.825	1.283	12.40	12.21	0.1930	0.1426	223	1,547	615	58.0
ALF2	1.3750	2.85	1.650	1.200	1.222	1.862	1.308	12.39	12.24	0.1967	0.1448	196	1,413	555	52.5
ALF2	1.3750	2.90	1.679	1.221	1.243	1.899	1.333	12.37	12.26	0.2004	0.1471	171	1,284	499	47.2
ALF2	1.3750	2.95	1.708	1.242	1.265	1.937	1.358	12.35	12.28	0.2042	0.1494	150	1,167	449	42.5
ALF2	1.3750	3.00	1.737	1.263	1.286	1.975	1.383	12.33	12.30	0.2081	0.1517	130	1,068	406	38.4
ALF2	1.3750	3.10	1.795	1.305	1.329	2.051	1.434	12.26	12.33	0.2163	0.1563	98	889	329	31.2
ALF2	1.3750	3.20	1.853	1.347	1.372	2.128	1.485	12.16	12.36	0.2250	0.1610	72	741	267	25.3
ALF2	1.4375	2.80	1.651	1.149	1.195	1.864	1.247	12.39	12.18	0.1969	0.1393	195	1,770	622	58.9
ALF2	1.5000	2.80	1.680	1.120	1.189	1.901	1.213	12.37	12.14	0.2006	0.1362	170	2,016	630	59.7
ALF2	1.5000	2.85	1.710	1.140	1.211	1.940	1.237	12.35	12.17	0.2045	0.1384	148	1,841	568	53.9
ALF2	1.5000	2.90	1.740	1.160	1.232	1.979	1.260	12.32	12.19	0.2086	0.1405	128	1,687	514	48.8
ALF2	1.5000	2.95	1.770	1.180	1.253	2.018	1.284	12.29	12.21	0.2127	0.1427	111	1,543	465	44.1
ALF2	1.5000	3.00	1.800	1.200	1.274	2.058	1.308	12.25	12.24	0.2170	0.1448	95	1,413	420	39.9
ALF2	1.5000	3.10	1.860	1.240	1.317	2.138	1.355	12.15	12.28	0.2262	0.1492	69	1,178	342	32.5
ALF2	1.5000	3.20	1.920	1.280	1.359	2.220	1.403	11.99	12.31	0.2365	0.1536	48	993	279	26.6
ALF2	1.5625	2.80	1.707	1.093	1.183	1.936	1.181	12.35	12.11	0.2042	0.1333	150	2,279	636	60.5
ALF2	1.6250	2.70	1.671	1.029	1.135	1.890	1.107	12.38	12.02	0.1994	0.1264	177	3,073	788	74.9
ALF2	1.6250	2.75	1.702	1.048	1.156	1.930	1.129	12.36	12.05	0.2035	0.1285	154	2,815	714	67.9
ALF2	1.6250	2.80	1.733	1.067	1.177	1.970	1.151	12.33	12.07	0.2077	0.1305	133	2,551	641	61.0
ALF2	1.6250	2.85	1.764	1.086	1.198	2.011	1.173	12.30	12.10	0.2119	0.1325	114	2,355	584	55.6
ALF2	1.6250	2.90	1.795	1.105	1.219	2.052	1.195	12.26	12.12	0.2163	0.1346	97	2,160	529	50.4
ALF2	1.6250	2.95	1.826	1.124	1.240	2.093	1.218	12.21	12.15	0.2209	0.1366	83	1,979	478	45.7
ALF2	1.6250	3.00	1.857	1.143	1.261	2.134	1.240	12.15	12.17	0.2257	0.1387	70	1,818	434	41.4
ALF2	1.6250	3.10	1.919	1.181	1.303	2.219	1.285	11.99	12.22	0.2364	0.1428	48	1,537	356	34.1
ALF2	1.6250	3.20	1.981	1.219	1.345	2.305	1.330	11.61	12.26	0.2520	0.1469	27	1,295	287	27.6
ALF2	1.7500	2.70	1.718	0.982	1.122	1.950	1.053	12.34	11.95	0.2056	0.1214	143	3,845	806	76.9
ALF2	1.7500	2.75	1.750	1.000	1.143	1.992	1.074	12.31	11.98	0.2099	0.1233	122	3,529	731	69.8
ALF2	1.7500	2.80	1.782	1.018	1.164	2.034	1.095	12.27	12.00	0.2144	0.1253	104	3,237	663	63.4
ALF2	1.7500	2.85	1.814	1.036	1.184	2.076	1.116	12.23	12.03	0.2190	0.1272	89	2,964	600	57.4
ALF2	1.7500	2.90	1.845	1.055	1.205	2.119	1.137	12.18	12.06	0.2239	0.1292	75	2,716	543	52.0
ALF2	1.7500	2.95	1.877	1.073	1.226	2.162	1.158	12.11	12.08	0.2290	0.1311	63	2,509	495	47.5
ALF2	1.7500	3.00	1.909	1.091	1.247	2.205	1.179	12.03	12.11	0.2345	0.1331	51	2,294	447	42.9
ALF2	1.7500	3.10	1.973	1.127	1.288	2.294	1.222	11.70	12.15	0.2490	0.1370	30	1,947	366	35.2

Table 3.4: Same as Tab. 3.2, but for H4. Table taken from Ref. [Koe1].

EOS	q	M [M_\odot]	M_1 [M_\odot]	M_2 [M_\odot]	\mathcal{M} [M_\odot]	M_1^b [M_\odot]	M_2^b [M_\odot]	R_1 [km]	R_2 [km]	C_1	C_2	$\Lambda_2^{(1)}$	$\Lambda_2^{(2)}$	$\tilde{\Lambda}$	κ_2^T
H4	1.000	2.80	1.400	1.400	1.219	1.528	1.528	13.56	13.56	0.1525	0.1525	886	886	886	83.0
H4	1.000	2.90	1.450	1.450	1.262	1.589	1.589	13.55	13.55	0.1581	0.1581	707	707	707	66.3
H4	1.000	2.95	1.475	1.475	1.284	1.619	1.619	13.54	13.54	0.1609	0.1609	634	634	634	59.4
H4	1.000	3.00	1.500	1.500	1.306	1.649	1.649	13.53	13.53	0.1638	0.1638	568	568	568	53.3
H4	1.000	3.10	1.550	1.550	1.349	1.711	1.711	13.50	13.50	0.1696	0.1696	452	452	452	42.4
H4	1.000	3.20	1.600	1.600	1.393	1.772	1.772	13.46	13.46	0.1756	0.1756	359	359	359	33.6
H4	1.000	3.30	1.650	1.650	1.436	1.835	1.835	13.40	13.40	0.1818	0.1818	283	283	283	26.6
H4	1.125	2.90	1.535	1.365	1.260	1.693	1.486	13.51	13.56	0.1679	0.1486	483	1,039	716	67.2
H4	1.125	2.95	1.562	1.388	1.281	1.725	1.514	13.49	13.56	0.1710	0.1512	428	935	641	60.1
H4	1.125	3.00	1.588	1.412	1.303	1.758	1.543	13.47	13.56	0.1742	0.1538	378	842	573	53.8
H4	1.125	3.10	1.641	1.459	1.347	1.824	1.599	13.41	13.54	0.1807	0.1591	296	686	459	43.1
H4	1.125	3.20	1.694	1.506	1.390	1.890	1.657	13.35	13.53	0.1875	0.1644	229	551	364	34.2
H4	1.125	3.30	1.747	1.553	1.433	1.958	1.714	13.26	13.50	0.1946	0.1699	176	445	288	27.1
H4	1.250	2.90	1.611	1.289	1.253	1.786	1.396	13.45	13.55	0.1770	0.1405	340	1,459	733	69.0
H4	1.250	2.95	1.639	1.311	1.275	1.821	1.423	13.42	13.56	0.1804	0.1428	299	1,320	657	61.9
H4	1.250	3.00	1.667	1.333	1.296	1.856	1.449	13.38	13.56	0.1839	0.1452	262	1,195	589	55.5
H4	1.250	3.10	1.722	1.378	1.339	1.926	1.502	13.30	13.56	0.1912	0.1501	200	980	472	44.5
H4	1.250	3.20	1.778	1.422	1.383	1.997	1.555	13.20	13.55	0.1990	0.1550	150	803	378	35.6
H4	1.250	3.30	1.833	1.467	1.426	2.069	1.609	13.06	13.54	0.2073	0.1600	111	658	301	28.4
H4	1.375	2.90	1.679	1.221	1.243	1.871	1.317	13.37	13.53	0.1855	0.1332	247	1,994	761	72.0
H4	1.375	2.95	1.708	1.242	1.265	1.908	1.341	13.32	13.54	0.1893	0.1355	214	1,818	685	64.8
H4	1.375	3.00	1.737	1.263	1.286	1.945	1.366	13.28	13.55	0.1932	0.1377	185	1,642	612	58.0
H4	1.375	3.10	1.795	1.305	1.329	2.019	1.416	13.16	13.56	0.2014	0.1422	137	1,357	494	46.8
H4	1.375	3.20	1.853	1.347	1.372	2.095	1.466	13.01	13.56	0.2104	0.1468	99	1,121	397	37.6
H4	1.375	3.30	1.911	1.389	1.415	2.171	1.516	12.81	13.56	0.2204	0.1514	69	927	318	30.2
H4	1.500	2.90	1.740	1.160	1.232	1.949	1.246	13.27	13.51	0.1937	0.1268	182	2,659	794	75.4
H4	1.500	2.95	1.770	1.180	1.253	1.987	1.269	13.21	13.52	0.1979	0.1289	156	2,411	712	67.7
H4	1.500	3.00	1.800	1.200	1.274	2.026	1.292	13.15	13.53	0.2022	0.1310	133	2,195	640	60.9
H4	1.500	3.10	1.860	1.240	1.317	2.104	1.339	12.98	13.54	0.2116	0.1353	95	1,825	519	49.4
H4	1.500	3.20	1.920	1.280	1.359	2.184	1.386	12.77	13.55	0.2221	0.1395	65	1,521	420	40.1
H4	1.500	3.30	1.980	1.320	1.402	2.265	1.433	12.43	13.56	0.2353	0.1438	40	1,269	338	32.3
H4	1.625	2.80	1.733	1.067	1.177	1.940	1.138	13.28	13.47	0.1927	0.1170	189	4,189	1,026	97.8
H4	1.625	2.85	1.764	1.086	1.198	1.980	1.160	13.22	13.48	0.1970	0.1190	161	3,775	915	87.3
H4	1.625	2.90	1.795	1.105	1.219	2.020	1.182	13.16	13.49	0.2015	0.1210	137	3,465	830	79.2
H4	1.625	2.95	1.826	1.124	1.240	2.060	1.204	13.08	13.50	0.2062	0.1230	115	3,162	748	71.5
H4	1.625	3.00	1.857	1.143	1.261	2.100	1.226	12.99	13.50	0.2111	0.1250	96	2,886	675	64.5
H4	1.625	3.10	1.919	1.181	1.303	2.183	1.270	12.77	13.52	0.2220	0.1290	65	2,398	546	52.4
H4	1.625	3.20	1.981	1.219	1.345	2.267	1.314	12.42	13.53	0.2355	0.1330	40	2,011	444	42.7
H4	1.750	2.80	1.782	1.018	1.164	2.002	1.083	13.19	13.44	0.1996	0.1119	147	5,375	1,074	102.9
H4	1.750	2.85	1.814	1.036	1.184	2.044	1.104	13.11	13.45	0.2043	0.1138	124	4,892	967	92.7
H4	1.750	2.90	1.845	1.055	1.205	2.085	1.125	13.03	13.46	0.2092	0.1157	103	4,459	872	83.7
H4	1.750	2.95	1.877	1.073	1.226	2.127	1.145	12.93	13.47	0.2145	0.1176	85	4,070	787	75.6
H4	1.750	3.00	1.909	1.091	1.247	2.169	1.166	12.81	13.48	0.2201	0.1195	70	3,701	707	68.0
H4	1.750	3.10	1.973	1.127	1.288	2.255	1.208	12.48	13.50	0.2335	0.1234	43	3,112	579	55.8

3.3 BNS Merger Simulations and Results

In the simulation campaign of Ref. [Koe1], we focus on BNS mergers for which the merger remnant collapses to a BH shortly after merger, to investigate the effect of mass ratio on the threshold mass and properties of remnant systems. For our analysis, we extract quantities characterizing the remnant system 5 ms after BH formation, and determine the collapse time in connection with our efforts to locate the threshold mass (cf. Chaps. 4 and 5 for a discussion of the method). Hence, we run our simulations until the GW signal has propagated beyond the furthest observer position (here $r_{10} \approx 1770$ km). Due to the large number of simulations, processing the simulation output had to be automated. For this purpose, we build and employ a workframe tailored specifically for the output of this simulation campaign and the related analysis. It processes and collects data of all simulations, preparing them for further analysis. If required, this code automatically prepares plots of some or all processed data, allowing for a quick investigation of new simulations.

3.3.1 Dynamical Evolutions with BAM and Clusters

Prior to performing simulations, proper parameters and initial conditions have to be established. With respect to the speed of the computations on different clusters, and due to the hybrid structure of BAM, i.e., the combined use of MPI and OpenMP parallelization, this especially involves determining the optimal ratio of cores hosting MPI processes to cores sharing work in OpenMP threads. Further, an appropriate number of nodes has to be established with respect to the workload of the simulations, which primarily depends on the size of the numerical grid. In the example of our typical high resolution runs (i.e. R3, cf. Sect. 3.3.2), the typical setup would be 8 nodes with 4 MPI/node and 9 OpenMP/MPI on one of ARA's partitions which has 36 cores per node. In practice, different aspects have to be taken into account to establish the number of nodes to be employed per simulation. Especially constraints and rules with respect to the usage of computational resources on a cluster have to be taken into account. These constraints may include a maximum number of nodes used by a single user per time. On another cluster one may be challenged with a limited budget of assigned CPU-hours. In general, the computational speed of parallel algorithms does not grow ideally (i.e., linearly) with the employed computational resources. Therefore, increasing the number of employed CPUs in order to increase computational speed and to reduce the total time spent on a simulation, may become an uneconomical solution.

In the example above, no upper limit is set on the available CPU-hour budget, but the maximum number of nodes per user and the maximum time per job are limited. If a simulation remains unfinished, it has to be resubmitted, continuing from the last saved checkpoint. On a practical note, choosing the number of nodes used per simulation may also be seen as a strategic choice, since large jobs may be disfavoured in terms of rules regulating the distribution of computational resources between users, while jobs requiring small numbers of nodes might pass through the queue more quickly. In a scenario of high usage rate on a cluster, users compete for the available resources. Seeking to efficiently acquire resources in this scenario, one may be required to adjust strategies in order to minimize the time between the end of one job and the start of the next job, this way minimizing idle waiting times.

As discussed in Sect. 3.2, we choose initial conditions such that the binaries would perform a minimal number of four revolutions on quasi-circular orbits. To that end, test runs have to be performed to find an adequate initial separation and adequate settings of SGRID parameters for which the eccentricity will be sufficiently small. In the practice of performing BNS merger simulations, an obstacle that would sometimes emerge, is that evolutions crash in connection with numerical fluxes and high velocities at the time of merger. Regarding the construction of numerical fluxes, BAM can locally switch from a 5th order weighted-essentially-non-oscillatory (WENOZ) scheme, Borges et al., 2008, to a more robust 2nd order local Lax-Friedrich method. On the one hand, this hybrid algorithm, introduced in Ref. [Bernuzzi et al., 2016a], handles artificial atmosphere. On the other hand, the 2nd order method proves to be more stable at merger, provided that the switch (which is based on the lapse function) is properly adjusted. Permanently switching to the low order flux usually makes it possible to continue crashed simulations from checkpoint. Another BAM feature that is important performing BNS merger simulations is the apparent-horizon finder, which we set to a high search frequency to determine the time of BH formation with high accuracy.

3.3.2 Grid Configurations

The BAM code solves the EFE and the equations of general relativistic hydrodynamics (GRHD) to evolve ID in time, employing an algorithm based on the method of lines with an explicit Runge-Kutta scheme. BAM uses finite differencing and is capable of adaptive mesh-refinement. Computations take place on a hierarchically structured grid. The computational domain contains L nested refinement levels, denominated $l = 0, \dots, L - 1$. Each grid on a level $l > 0$ is completely covered by a grid on level

$l - 1$, cf. Fig. 3.3. The regular Cartesian grids on each level are characterized by the number of points n in each direction, and a constant grid spacing h_l on level l which is two times finer than the spacing of level $l - 1$, i.e., the grid spacing on each level is determined by the grid spacing h_0 of the coarsest level:

$$h_l = \frac{h_0}{2^l} . \quad (3.21)$$

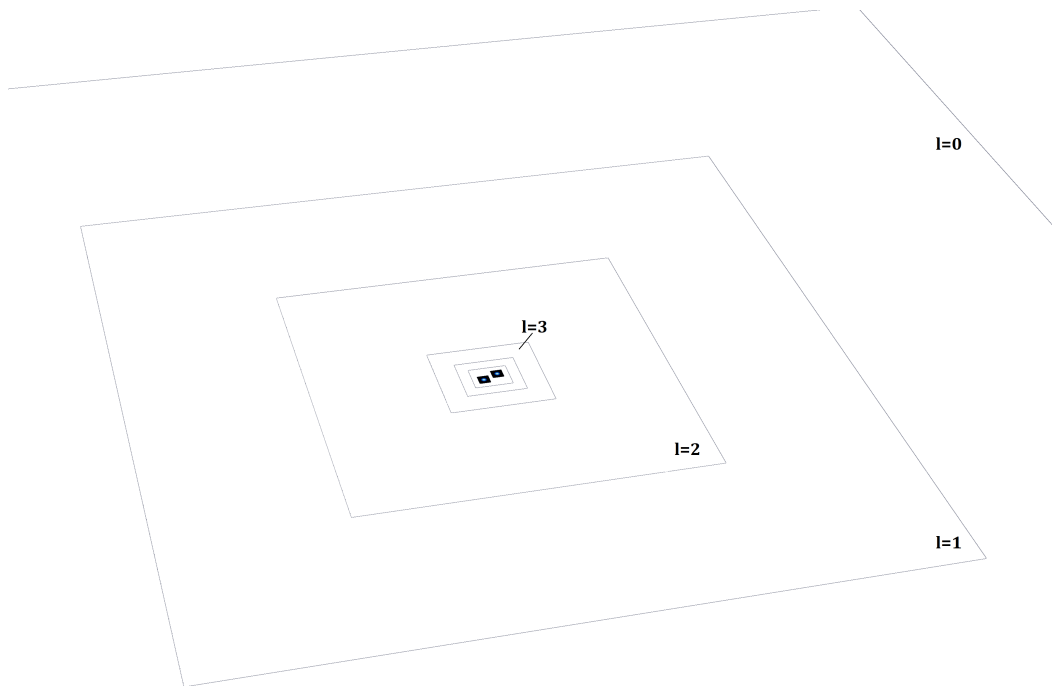


Figure 3.3: Illustration of BAM's grid structure - example one (number of fixed and moving grid levels as used for all simulations presented in Tabs. 3.7 to 3.9 and 4.1). Depicted is the x, y -plane of a domain which is covered by seven levels of grids, denominated $l = 0$ (innermost grid), ... $l = 6$ (outermost grid). On level $l = 6$ each star is placed in each own moving box. Moving boxes belonging to single stars on the levels $l = 3$, $l = 4$ and $l = 5$ would overlap due to insufficiently large separation of the stars. Therefore these boxes are merged to single grids covering both stars. The grids on the levels $l = 0$, $l = 1$ and $l = 2$ are non-moving. Each grid on level $l > 0$ is covered by a grid on level $l - 1$. On level six the density ρ is included in the illustration.

There are two types of grids: moving and non-moving grids. Grids on levels $l \leq l^{\text{mv}}$ are single non-moving cubic boxes, and possess a large coordinate extent intended for GW extraction. On levels $l \geq l^{\text{mv}}$ on the other hand, more than one grid may be placed, each covering one of the simulated compact objects. In cases where the individual moving grids on a level would overlap, they are replaced by a single rectangular

bounding box. This is illustrated in Figs. 3.3 and 3.4. The outlines in Fig. 3.3 show the relative extent of grids. In all of our simulations, the same number of levels, i.e., $L = 7$, is used. On level $l = 6$, each of the two individual grids contain a NS. On levels with $l \in \{3, 4, 5\}$, individual grids are replaced with rectangular boxes. Due to the small initial separation of the stars, they are never split during our simulations. To show the case of separated grids on more than one level, we present the example of a grid with $L = 11$ levels in Fig. 3.4. It contains well separated grids on the levels $l = 9$ and $l = 10$, each of them centred at the respective component of the binary. Each of the grids on level $l = 10$ is fully covered by grids on level $l = 9$.

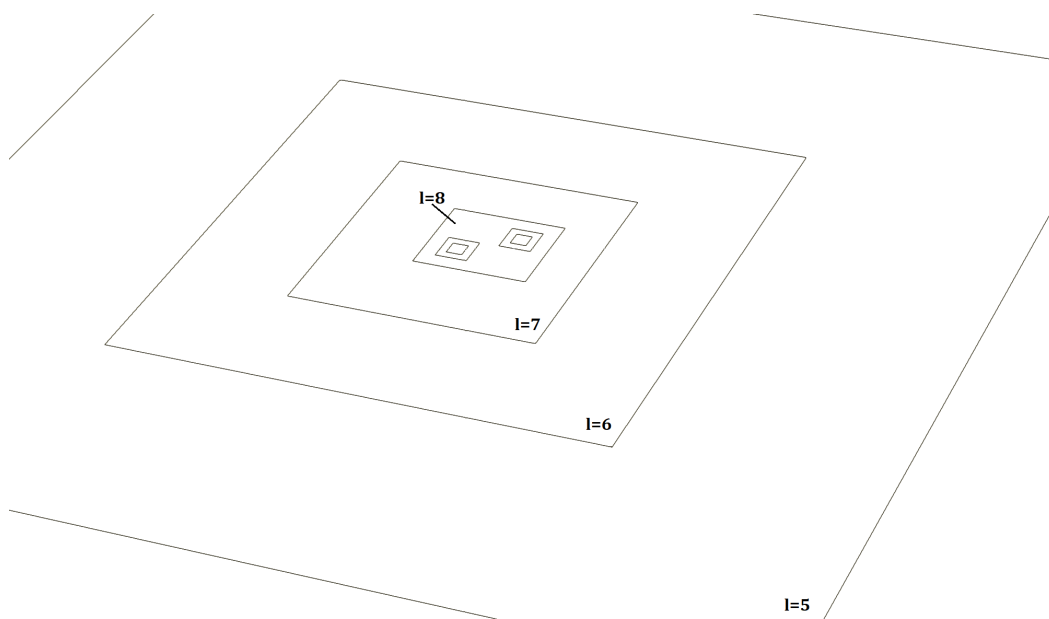


Figure 3.4: Illustration of BAM's grid structure - example two. Innermost levels ($l = 5, \dots, l = 10$) of a grid with eleven levels. On levels $l = 9$ and $l = 10$ separate grids cover the components of the binary systems. The moving grids on level $l = 8$ are merged, grids on levels with $l \leq 7$ are non-moving.

In our simulations, grids on four of the seven levels are moving boxes, three are non-moving. In Ref. [Koe1], we distinguish four resolutions R1 to R4, based on the number of grid points in each direction, cf. Tab. 3.5. Typically, simulations have been conducted with only two of the specified resolutions, i.e., R2 and R3, cf. Tabs. 3.7 to 3.9. In the case of R3, for example, non-moving boxes have 320 points in each direction, moving boxes have 160. The grid spacing has to be chosen such that the innermost boxes fully cover the stars which they contain. In the case of SLy and ALF2 the grid spacing on the finest level of a R3 grid is 185 m, in the case of the H4 it is 196 m. Due to this difference, which compensates for the larger radii of H4 stars

(cf. Fig. 3.1), we distinguish between two otherwise equally constructed resolutions, denominating the highest resolution R4 in the case of SLy and ALF2, and R4* in the case of H4. The extent of the innermost grids covering the stars determines the size of all (non-fused) grids. The overall extent of the numerical domain additionally depends on L . Unlike the grid spacings on each level, the outer boundary position does not depend on the number of grid points. Properties of the used numerical resolutions are collected in Tab. 3.5.

Table 3.5: Grid configurations. As the number of levels is the same for all used resolutions, the names in the first column primarily refer to the number of grid points. However, the resolutions used for H4 are marked with a '*', as a different grid spacing was needed to fully cover the stars on the finest level. The numerical domain contains L grid levels of which L_{mv} are moving box levels. The number of grid points in each direction are n and n_{mv} respectively. The grid spacing on the finest level (innermost boxes covering the NSs), h_6 , is 2^6 times finer than the spacing on the coarsest level, h_0 . The last column refers to the outer boundary position R_0 . Table taken from [Koe1].

Name	L	L_{mv}	n	n_{mv}	EOS	h_6 [m]	h_0 [km]	R_0 [km]
R4	7	4	384	192	ALF2, SLy	154	9.847	3781.1
R4*	7	4	384	192	H4	163	10.437	4008.0
R3	7	4	320	160	ALF2, SLy	185	11.816	3781.1
R3*	7	4	320	160	H4	196	12.525	4008.0
R2	7	4	256	128	ALF2, SLy	231	14.770	3781.1
R2*	7	4	256	128	H4	245	15.656	4008.0
R1	7	4	192	96	ALF2, SLy	308	19.693	3781.1
R1*	7	4	192	96	H4	326	20.875	4008.0

3.3.3 Collapse Types, Properties of the Remnant System, Data

We conclude this chapter, presenting results and data of our simulation campaign that we are going to analyse in the following chapters. We begin by considering once again the parameter space covered by our simulations. With respect to a categorization of the BNS mergers, Tab. 3.6 gives insight into this parameter space. Rows are defined with respect to the mass ratio, each of them being subdivided with respect to the considered EOSs. Columns refer to the binaries total masses M . Depending on q and the EOS, different ranges of M have been studied. Each entry in Tab. 3.6 stands for one considered configuration, which usually has been simulated using two different resolutions. The merger simulations are categorized based on a criterion related to

the collapse time, cf. Sect. 4.6. In cases where different results were obtained for different numerical resolutions, more than one type is given, marked with the respective resolution as an index. We will motivate the employed criterion in Chap. 4, leaving the evaluation for Chap. 5.

Table 3.6: Summary of simulations and collapse types: Columns are ordered by increasing total mass of the binaries, rows are ordered by increasing mass ratio and subdivided by the EOSs. The collapse types (cf. Sect. 4.6) may differ between resolutions. In these cases, all types are given with reference to their respective resolution. In cases where a configuration has only been simulated with one resolution, the respective resolution is given as an index. Table taken from Ref. [Koe1].

q	EOS	M										
		2.7	2.75	2.8	2.85	2.9	2.95	3.0	3.1	3.2	3.3	
1.0	SLy	IV_{R3}	II	I_{R3}/II_{R2}	I	I		I	I	I		
	ALF2			III	II_{R3}/III_{R2}	II	II		I	I	I	
	H4			III_{R2*}		III	III_{R3*}/II_{R2*}	$I_{R3,R2}/II_{R1}$	I	I	I	I
1.125	SLy		III	III_{R3}/II_{R2}	I	I		I	I	I		
	ALF2			III	III	II	II	I	I	I	I	
	H4				III	III	III	II	I	I	I	I
1.25	SLy	IV_{R3}	$III_{R4,R3}/IV_{R2}$	$II_{R4,R2}/III_{R3}$	I	I		I	I	I		
	ALF2			III	II	II	II	I	I	I	I	
	H4				III	III	III	II	I	I	I	I
1.375	SLy		III	II	I	I		I	I	I		
	ALF2			III	II	II	I	I	I	I	I	
	H4				III	III	III	II	I	I	I	I
1.5	SLy	IV_{R3}	IV_{R3}/III_{R2}	I	I	I		I	I	I		
	ALF2			III	II	I	I	I	I	I	I	
	H4					III	$II_{R4*}/I_{R3*}/III_{R2*}$	I	I	I	I	I
1.625	SLy		II_{R3}/IV_{R2}	I	I	I		I	I	I		
	ALF2	IV_{R3}	III	II_{R3}/III_{R2}	I	I	I	I	I	I	I	
	H4			IV_{R2*}	IV_{R3*}/III_{R2*}	I	I	I	I	I	I	
1.75	SLy	IV_{R3}	I	I	I	I		I	I	I		
	ALF2	IV	III	I	I	I	I	I	I	I		
	H4			IV_{R2*}	II_{R3*}/I_{R2*}	I	I	I	I	I		

Taking a first look at the data, we consider Tabs. 3.7 to 3.9, which list results of our simulations. Each simulation is identified by EOS, resolution, mass ratio and total mass. Error estimates were computed based on differences between results obtained for the highest available resolutions - typically R3 and R2. Presented are residual eccentricities, the final status of the simulation (i.e., whether or not a BH formed within simulation time), the merger type, collapse time and properties of the remnant system (i.e., BH mass, BH spin and disk mass). Our finding for the collapse time will be the subject of discussions in chapters 4 and 5. Data related to properties of the remnant system are portrayed in Figs. 3.5 and 3.6, plotted against q in the case of Fig. 3.5, and plotted against M in Fig. 3.6. We will examine these results in Sect. 6.3.

Table 3.7: Summary of results - SLy subset. Columns one to four characterize the simulations in terms of EOS, resolution (res), mass ratio (q) and total mass (M). Residual eccentricities are given in column five. Whether or not a BH formed within simulation time is answered in column six, in accordance with the merger types reported in column seven. If the merger type deviates between resolutions, both of the classifications are reported. Results for the collapse time t_{coll} are given in column seven. In cases where a BH was formed its (gravitational) mass M_{BH} , its spin χ_{BH} , and the (baryonic) mass of the disk M_{disk} , are reported in columns eight to ten. Table adapted from Ref. [Koe1].

EOS	res	q	M [M_{\odot}]	ecc [10^{-2}]	BH	Type	t_{coll} [ms]	M_{BH} [M_{\odot}]	χ_{BH}	M_{disk} [$10^{-2} M_{\odot}$]
SLy	R3	1.000	2.70	1.51	no	IV				
SLy	R3, R2	1.000	2.75	1.50	yes	II	2.15 ± 0.10	2.642 ± 0.010	0.708 ± 0.012	2.365 ± 0.4
SLy	R3, R2	1.000	2.80	1.47	yes	II/I	1.28 ± 1.18	2.716 ± 0.040	0.749 ± 0.063	0.159 ± 2.4
SLy	R3, R2	1.000	2.85	1.53	yes	I	0.85 ± 0.01	2.780 ± 0.010	0.768 ± 0.012	0.195 ± 0.1
SLy	R3, R2	1.000	2.90	1.74	yes	I	0.73 ± 0.02	2.831 ± 0.009	0.768 ± 0.009	0.056 ± 0.0
SLy	R3, R2	1.000	3.00	1.95	yes	I	0.63 ± 0.00	2.930 ± 0.003	0.760 ± 0.005	0.007 ± 0.0
SLy	R3, R2	1.000	3.10	2.00	yes	I	0.56 ± 0.00	3.025 ± 0.003	0.750 ± 0.004	0.004 ± 0.0
SLy	R(4,3,2)	1.125	2.75	1.50	yes	III	12.12 ± 4.18	2.514 ± 0.027	0.550 ± 0.018	13.200 ± 2.8
SLy	R3, R2	1.125	2.80	1.47	yes	III/II	6.26 ± 1.31	2.616 ± 0.015	0.613 ± 0.016	8.051 ± 1.1
SLy	R3, R2	1.125	2.85	1.52	yes	I	0.91 ± 0.04	2.766 ± 0.012	0.752 ± 0.014	1.370 ± 0.4
SLy	R3, R2	1.125	2.90	1.72	yes	I	0.78 ± 0.01	2.823 ± 0.007	0.758 ± 0.009	0.904 ± 0.2
SLy	R3, R2	1.125	3.00	1.94	yes	I	0.65 ± 0.00	2.928 ± 0.004	0.757 ± 0.006	0.319 ± 0.0
SLy	R3, R2	1.125	3.10	1.98	yes	I	0.57 ± 0.01	3.025 ± 0.002	0.749 ± 0.004	0.080 ± 0.0
SLy	R3	1.250	2.70	1.54	no	IV				
SLy	R(4,3,2)	1.250	2.75	1.52	yes	III/(IV)	17.97 ± 3.87	2.450 ± 0.033	0.488 ± 0.034	20.209 ± 4.1
SLy	R(4,3,2)	1.250	2.80	1.47	yes	III/II	2.46 ± 12.92	2.652 ± 0.163	0.677 ± 0.171	7.799 ± 13.4
SLy	R3, R2	1.250	2.85	1.49	yes	I	1.04 ± 0.04	2.710 ± 0.009	0.693 ± 0.009	7.292 ± 0.5
SLy	R3, R2	1.250	2.90	1.69	yes	I	0.85 ± 0.03	2.784 ± 0.005	0.717 ± 0.006	5.346 ± 0.2
SLy	R3, R2	1.250	3.00	1.94	yes	I	0.66 ± 0.02	2.915 ± 0.005	0.743 ± 0.006	2.057 ± 0.3
SLy	R3, R2	1.250	3.10	1.98	yes	I	0.58 ± 0.01	3.022 ± 0.003	0.745 ± 0.004	0.936 ± 0.1
SLy	R(4,3,2)	1.375	2.75	1.53	yes	III	12.76 ± 2.92	2.495 ± 0.013	0.531 ± 0.014	17.122 ± 1.4
SLy	R3, R2	1.375	2.80	1.49	yes	II	2.40 ± 0.27	2.639 ± 0.003	0.653 ± 0.001	9.594 ± 0.3
SLy	R3, R2	1.375	2.85	1.47	yes	I	1.05 ± 0.05	2.691 ± 0.009	0.666 ± 0.011	10.582 ± 1.0
SLy	R3, R2	1.375	2.90	1.66	yes	I	0.85 ± 0.04	2.760 ± 0.004	0.687 ± 0.004	8.364 ± 0.3
SLy	R3, R2	1.375	3.00	1.92	yes	I	0.68 ± 0.02	2.884 ± 0.006	0.708 ± 0.008	5.997 ± 0.5
SLy	R3, R2	1.375	3.10	2.00	yes	I	0.58 ± 0.01	2.994 ± 0.005	0.715 ± 0.006	4.614 ± 0.4
SLy	R3	1.500	2.70	1.54	no	IV				
SLy	R3, R2	1.500	2.75	1.53	?	III/IV	24.05	2.442	0.474	24.423
SLy	R3, R2	1.500	2.80	1.50	yes	I	1.44 ± 0.10	2.622 ± 0.002	0.632 ± 0.004	13.055 ± 0.2
SLy	R3, R2	1.500	2.85	1.46	yes	I	0.99 ± 0.03	2.677 ± 0.008	0.640 ± 0.009	12.867 ± 0.5
SLy	R3, R2	1.500	2.90	1.63	yes	I	0.85 ± 0.03	2.741 ± 0.007	0.657 ± 0.010	11.454 ± 0.5
SLy	R3, R2	1.500	3.00	1.96	yes	I	0.67 ± 0.02	2.866 ± 0.006	0.681 ± 0.008	8.536 ± 0.4
SLy	R3, R2	1.500	3.10	2.03	yes	I	0.57 ± 0.03	2.968 ± 0.002	0.682 ± 0.004	7.969 ± 0.2
SLy	R3, R2	1.625	2.75	1.54	?	IV/II	2.83	2.527	0.566	18.343
SLy	R3, R2	1.625	2.80	1.52	yes	I	1.11 ± 0.01	2.622 ± 0.010	0.618 ± 0.010	13.807 ± 0.8
SLy	R3, R2	1.625	2.85	1.46	yes	I	0.94 ± 0.02	2.670 ± 0.009	0.618 ± 0.010	14.112 ± 0.7
SLy	R3, R2	1.625	2.90	1.59	yes	I	0.81 ± 0.04	2.726 ± 0.005	0.627 ± 0.007	13.531 ± 0.2
SLy	R3, R2	1.625	3.00	1.96	yes	I	0.66 ± 0.01	2.846 ± 0.006	0.648 ± 0.007	11.012 ± 0.6
SLy	R3, R2	1.625	3.10	2.07	yes	I	0.56 ± 0.01	2.946 ± 0.007	0.648 ± 0.007	10.661 ± 0.8
SLy	R3	1.750	2.70	1.54	no	IV				
SLy	R3, R2	1.750	2.75	1.55	yes	I	1.26 ± 0.03	2.560 ± 0.009	0.585 ± 0.011	15.589 ± 0.7
SLy	R3, R2	1.750	2.80	1.53	yes	I	1.02 ± 0.02	2.615 ± 0.008	0.591 ± 0.008	15.036 ± 0.7
SLy	R3, R2	1.750	2.85	1.47	yes	I	0.89 ± 0.01	2.660 ± 0.004	0.591 ± 0.006	15.431 ± 0.4
SLy	R3, R2	1.750	2.90	1.52	yes	I	0.80 ± 0.01	2.712 ± 0.004	0.595 ± 0.004	15.141 ± 0.4
SLy	R3, R2	1.750	3.00	1.94	yes	I	0.63 ± 0.01	2.830 ± 0.002	0.616 ± 0.003	12.992 ± 0.1
SLy	R3, R2	1.750	3.10	2.09	yes	I	0.50 ± 0.01	2.930 ± 0.007	0.618 ± 0.009	12.553 ± 1.1

Table 3.8: Same as Tab. 3.7, but for ALF2. Table adapted from Ref. [Koe1].

EOS	res	q	M [M_{\odot}]	ecc	BH	Type	t_{coll} [ms]	M_{BH} [M_{\odot}]	χ_{BH}	M_{disk} [$10^{-2} M_{\odot}$]
ALF2	R(3,2,1)	1.000	2.80	1.63	yes	III	7.47 ± 1.46	2.652 ± 0.034	0.642 ± 0.035	5.981 ± 3.5
ALF2	R3, R2	1.000	2.85	1.77	yes	III/II	4.76 ± 1.29	2.730 ± 0.020	0.680 ± 0.015	3.259 ± 2.4
ALF2	R(3,2,1)	1.000	2.90	1.83	yes	II	3.41 ± 0.04	2.788 ± 0.005	0.708 ± 0.003	3.189 ± 1.0
ALF2	R3, R2	1.000	2.95	1.85	yes	II	2.25 ± 0.03	2.849 ± 0.003	0.737 ± 0.000	2.456 ± 0.6
ALF2	R(3,2,1)	1.000	3.00	1.85	yes	I	1.20 ± 0.46	2.927 ± 0.019	0.776 ± 0.022	0.240 ± 1.3
ALF2	R(3,2,1)	1.000	3.10	1.83	yes	I	0.84 ± 0.02	3.036 ± 0.000	0.786 ± 0.002	0.205 ± 0.0
ALF2	R3, R2	1.000	3.20	1.72	yes	I	0.74 ± 0.01	3.134 ± 0.000	0.778 ± 0.001	0.090 ± 0.0
ALF2	R3, R2	1.125	2.80	1.59	yes	III	10.74 ± 1.52	2.548 ± 0.023	0.558 ± 0.022	18.283 ± 2.6
ALF2	R3, R2	1.125	2.85	1.75	yes	III	5.12 ± 1.01	2.719 ± 0.030	0.680 ± 0.030	5.212 ± 3.2
ALF2	R3, R2	1.125	2.90	1.82	yes	II	3.76 ± 0.13	2.791 ± 0.014	0.710 ± 0.021	2.984 ± 1.2
ALF2	R3, R2	1.125	2.95	1.87	yes	II	2.32 ± 0.02	2.852 ± 0.008	0.739 ± 0.013	2.791 ± 0.3
ALF2	R3, R2	1.125	3.00	1.89	yes	I	1.10 ± 0.15	2.916 ± 0.010	0.765 ± 0.014	2.024 ± 0.4
ALF2	R3, R2	1.125	3.10	1.86	yes	I	0.84 ± 0.02	3.022 ± 0.003	0.771 ± 0.004	1.834 ± 0.4
ALF2	R3, R2	1.125	3.20	1.73	yes	I	0.72 ± 0.02	3.129 ± 0.001	0.772 ± 0.001	0.841 ± 0.1
ALF2	R(3,2,1)	1.250	2.80	1.55	yes	III	9.44 ± 1.17	2.546 ± 0.002	0.555 ± 0.006	18.609 ± 0.1
ALF2	R3, R2	1.250	2.85	1.73	yes	II	4.99 ± 0.31	2.661 ± 0.006	0.624 ± 0.005	11.760 ± 1.3
ALF2	R(3,2,1)	1.250	2.90	1.84	yes	II	3.56 ± 0.14	2.745 ± 0.003	0.653 ± 0.000	7.452 ± 0.7
ALF2	R3, R2	1.250	2.95	1.89	yes	II	2.55 ± 0.14	2.796 ± 0.001	0.671 ± 0.000	7.961 ± 0.3
ALF2	R(3,2,1)	1.250	3.00	1.91	yes	I	1.02 ± 0.07	2.858 ± 0.010	0.707 ± 0.011	8.963 ± 0.8
ALF2	R3, R2	1.250	3.10	1.90	yes	I	0.79 ± 0.04	2.983 ± 0.010	0.731 ± 0.010	6.690 ± 1.0
ALF2	R3, R2	1.250	3.20	1.74	yes	I	0.69 ± 0.02	3.105 ± 0.008	0.748 ± 0.009	3.936 ± 0.9
ALF2	R3	1.3125	2.80	1.54	yes	III	5.82	2.585	0.584	14.500
ALF2	R3, R2	1.375	2.80	1.52	yes	III	5.86 ± 0.29	2.577 ± 0.000	0.573 ± 0.011	15.868 ± 0.3
ALF2	R3, R2	1.375	2.85	1.72	yes	II	3.39 ± 1.17	2.651 ± 0.009	0.600 ± 0.009	12.879 ± 0.8
ALF2	R3, R2	1.375	2.90	1.83	yes	II	2.53 ± 0.69	2.712 ± 0.018	0.633 ± 0.039	12.926 ± 0.3
ALF2	R3, R2	1.375	2.95	1.89	yes	I	1.10 ± 0.08	2.761 ± 0.007	0.649 ± 0.005	14.319 ± 0.9
ALF2	R3, R2	1.375	3.00	1.92	yes	I	0.93 ± 0.06	2.827 ± 0.005	0.668 ± 0.007	12.954 ± 0.3
ALF2	R3, R2	1.375	3.10	1.89	yes	I	0.75 ± 0.04	2.943 ± 0.002	0.686 ± 0.004	11.342 ± 0.1
ALF2	R3, R2	1.375	3.20	1.74	yes	I	0.64 ± 0.02	3.061 ± 0.001	0.700 ± 0.003	9.212 ± 0.2
ALF2	R3	1.4375	2.80	1.52	yes	III	7.37	2.549	0.540	18.960
ALF2	R(3,2,1)	1.500	2.80	1.53	yes	III	10.99 ± 3.69	2.554 ± 0.001	0.542 ± 0.006	19.203 ± 0.7
ALF2	R3, R2	1.500	2.85	1.73	yes	II	4.00 ± 0.21	2.632 ± 0.012	0.589 ± 0.001	17.356 ± 1.9
ALF2	R(3,2,1)	1.500	2.90	1.84	yes	I	1.23 ± 0.08	2.702 ± 0.004	0.625 ± 0.008	16.247 ± 0.4
ALF2	R3, R2	1.500	2.95	1.89	yes	I	0.97 ± 0.04	2.758 ± 0.003	0.634 ± 0.004	15.411 ± 0.4
ALF2	R(3,2,1)	1.500	3.00	1.92	yes	I	0.84 ± 0.03	2.817 ± 0.007	0.644 ± 0.008	14.731 ± 0.0
ALF2	R(3,2,1)	1.500	3.10	1.87	yes	I	0.69 ± 0.02	2.924 ± 0.002	0.654 ± 0.003	13.420 ± 0.2
ALF2	R3, R2	1.500	3.20	1.73	yes	I	0.58 ± 0.00	3.034 ± 0.001	0.665 ± 0.001	12.433 ± 0.5
ALF2	R3	1.5625	2.80	1.55	yes	II	4.86	2.573	0.558	18.336
ALF2	R3	1.625	2.70	1.47	no	IV				
ALF2	R3, R2	1.625	2.75	1.43	yes	III	19.21 ± 7.86	2.428 ± 0.027	0.452 ± 0.022	27.695 ± 2.6
ALF2	R3, R2	1.625	2.80	1.52	yes	II/III	4.73 ± 0.93	2.570 ± 0.010	0.553 ± 0.011	19.241 ± 1.0
ALF2	R3, R2	1.625	2.85	1.70	yes	I	1.03 ± 0.35	2.652 ± 0.011	0.582 ± 0.008	17.069 ± 0.1
ALF2	R3, R2	1.625	2.90	1.87	yes	I	1.00 ± 0.05	2.706 ± 0.005	0.610 ± 0.006	16.133 ± 0.3
ALF2	R3, R2	1.625	2.95	1.92	yes	I	0.86 ± 0.04	2.753 ± 0.008	0.609 ± 0.010	16.450 ± 0.9
ALF2	R3, R2	1.625	3.00	1.91	yes	I	0.76 ± 0.01	2.807 ± 0.005	0.615 ± 0.006	15.895 ± 0.7
ALF2	R3, R2	1.625	3.10	1.88	yes	I	0.63 ± 0.04	2.915 ± 0.007	0.626 ± 0.007	14.790 ± 0.9
ALF2	R3, R2	1.625	3.20	1.77	yes	I	0.46 ± 0.01	3.020 ± 0.005	0.633 ± 0.004	13.747 ± 0.0
ALF2	R3, R2	1.750	2.70	1.48	no	IV				
ALF2	R3, R2	1.750	2.75	1.44	yes	III	15.27 ± 4.42	2.441 ± 0.021	0.461 ± 0.009	27.672 ± 2.0
ALF2	R3, R2	1.750	2.80	1.47	yes	I	1.33 ± 0.07	2.596 ± 0.005	0.571 ± 0.005	17.814 ± 0.6
ALF2	R3, R2	1.750	2.85	1.74	yes	I	1.25 ± 0.16	2.654 ± 0.008	0.604 ± 0.029	16.516 ± 1.2
ALF2	R3, R2	1.750	2.90	1.86	yes	I	0.88 ± 0.01	2.696 ± 0.007	0.579 ± 0.007	17.401 ± 1.0
ALF2	R3, R2	1.750	2.95	1.93	yes	I	0.77 ± 0.04	2.747 ± 0.008	0.582 ± 0.010	17.381 ± 0.9
ALF2	R3, R2	1.750	3.00	1.96	yes	I	0.68 ± 0.01	2.796 ± 0.003	0.583 ± 0.005	17.260 ± 0.5
ALF2	R3, R2	1.750	3.10	1.95	yes	I	0.50 ± 0.02	2.900 ± 0.003	0.591 ± 0.004	16.533 ± 0.5

Table 3.9: Same as Tab. 3.7, but for H4. Table adapted from Ref. [Koe1].

EOS	res	q	M [M_{\odot}]	ecc [10^{-2}]	BH	Type	t_{coll} [ms]	M_{BH} [M_{\odot}]	χ_{BH}	M_{disk} [$10^{-2} M_{\odot}$]
H4	R2*	1.000	2.80	1.76	?	III	14.15	2.586	0.567	11.745
H4	R3*, R2*	1.000	2.90	1.87	yes	III	6.34 ± 1.34	2.758 ± 0.004	0.666 ± 0.010	4.738 ± 0.0
H4	R3*, R2*	1.000	2.95	1.90	yes	III/II	5.29 ± 0.32	2.805 ± 0.000	0.674 ± 0.010	5.493 ± 1.2
H4	R3*, R2*	1.000	3.00	1.88	yes	II	3.70 ± 0.02	2.888 ± 0.016	0.727 ± 0.017	3.023 ± 1.2
H4	R3*, R2*	1.000	3.10	1.81	yes	I	1.36 ± 0.07	3.024 ± 0.004	0.784 ± 0.006	0.190 ± 0.1
H4	R3*, R2*	1.000	3.20	1.62	yes	I	0.91 ± 0.01	3.130 ± 0.004	0.788 ± 0.007	0.157 ± 0.0
H4	R3*, R2*	1.000	3.30	1.40	yes	I	0.77 ± 0.00	3.229 ± 0.005	0.780 ± 0.006	0.079 ± 0.0
H4	R3*, R2*	1.125	2.90	1.87	yes	III	7.83 ± 2.48	2.730 ± 0.057	0.637 ± 0.048	7.867 ± 6.2
H4	R3*, R2*	1.125	2.95	1.88	yes	III	5.17 ± 0.04	2.796 ± 0.003	0.676 ± 0.015	7.197 ± 0.8
H4	R3*, R2*	1.125	3.00	1.88	yes	II	4.09 ± 0.16	2.866 ± 0.022	0.706 ± 0.028	5.353 ± 1.5
H4	R3*, R2*	1.125	3.10	1.80	yes	I	1.17 ± 0.05	2.992 ± 0.006	0.756 ± 0.008	4.177 ± 0.0
H4	R3*, R2*	1.125	3.20	1.59	yes	I	0.89 ± 0.01	3.112 ± 0.006	0.771 ± 0.007	2.187 ± 0.2
H4	R3*, R2*	1.125	3.30	1.39	yes	I	0.76 ± 0.02	3.218 ± 0.004	0.771 ± 0.005	1.244 ± 0.1
H4	R3*, R2*	1.250	2.90	1.89	yes	III	6.28 ± 1.36	2.693 ± 0.031	0.612 ± 0.036	12.869 ± 2.8
H4	R3*, R2*	1.250	2.95	1.90	yes	III	5.14 ± 0.04	2.737 ± 0.012	0.615 ± 0.010	13.836 ± 1.2
H4	R3*, R2*	1.250	3.00	1.87	yes	II	4.17 ± 0.30	2.804 ± 0.002	0.647 ± 0.006	12.518 ± 0.4
H4	R3*, R2*	1.250	3.10	1.78	yes	I	1.10 ± 0.06	2.917 ± 0.005	0.685 ± 0.007	12.975 ± 0.0
H4	R3*, R2*	1.250	3.20	1.55	yes	I	0.86 ± 0.02	3.052 ± 0.005	0.715 ± 0.005	8.974 ± 0.2
H4	R3*, R2*	1.250	3.30	1.36	yes	I	0.74 ± 0.02	3.172 ± 0.002	0.730 ± 0.002	7.043 ± 0.3
H4	R3*, R2*	1.375	2.90	1.90	yes	III	8.96 ± 2.84	2.654 ± 0.032	0.567 ± 0.022	17.884 ± 3.1
H4	R3*, R2*	1.375	2.95	1.90	yes	III	6.93 ± 1.47	2.718 ± 0.006	0.595 ± 0.009	17.093 ± 0.1
H4	R3*, R2*	1.375	3.00	1.88	yes	II	3.04 ± 0.04	2.785 ± 0.005	0.628 ± 0.008	16.103 ± 0.1
H4	R3*, R2*	1.375	3.10	1.76	yes	I	1.02 ± 0.02	2.913 ± 0.007	0.671 ± 0.010	14.414 ± 0.3
H4	R3*, R2*	1.375	3.20	1.50	yes	I	0.82 ± 0.01	3.029 ± 0.007	0.687 ± 0.009	12.339 ± 0.5
H4	R3*, R2*	1.375	3.30	1.30	yes	I	0.67 ± 0.01	3.146 ± 0.005	0.700 ± 0.006	10.345 ± 0.5
H4	R3*, R2*	1.500	2.90	1.90	yes	III	10.97 ± 2.70	2.611 ± 0.032	0.529 ± 0.025	23.979 ± 3.4
H4	R(4,3,2)*	1.500	2.95	1.90	yes	I/II	2.10 ± 0.20	2.725 ± 0.002	0.612 ± 0.002	19.098 ± 0.3
H4	R3*, R2*	1.500	3.00	1.88	yes	I	1.26 ± 0.06	2.794 ± 0.009	0.633 ± 0.010	16.900 ± 0.8
H4	R3*, R2*	1.500	3.10	1.75	yes	I	0.91 ± 0.02	2.903 ± 0.006	0.647 ± 0.008	15.627 ± 0.4
H4	R3*, R2*	1.500	3.20	1.42	yes	I	0.73 ± 0.02	3.012 ± 0.006	0.655 ± 0.007	14.699 ± 0.5
H4	R3*, R2*	1.500	3.30	1.45	yes	I	0.57 ± 0.01	3.116 ± 0.000	0.660 ± 0.002	14.033 ± 0.0
H4	R2*	1.625	2.80	1.82	?	IV				
H4	R3*, R2*	1.625	2.85	1.87	?	III/IV	51.79	2.492	0.446	29.693
H4	R3*, R2*	1.625	2.90	1.90	yes	I	1.81 ± 0.11	2.666 ± 0.008	0.580 ± 0.008	20.552 ± 0.5
H4	R3*, R2*	1.625	2.95	1.90	yes	I	1.31 ± 0.03	2.730 ± 0.009	0.598 ± 0.009	18.850 ± 0.3
H4	R3*, R2*	1.625	3.00	1.87	yes	I	1.10 ± 0.02	2.785 ± 0.003	0.605 ± 0.004	18.304 ± 0.1
H4	R3*, R2*	1.625	3.10	1.71	yes	I	0.79 ± 0.03	2.888 ± 0.008	0.613 ± 0.008	17.771 ± 0.7
H4	R3*, R2*	1.625	3.20	1.35	yes	I	0.57 ± 0.05	2.991 ± 0.005	0.617 ± 0.004	17.290 ± 0.3
H4	R2*	1.750	2.80	1.84	?	IV				
H4	R3*, R2*	1.750	2.85	1.89	yes	II/I	2.03 ± 0.07	2.608 ± 0.006	0.548 ± 0.006	21.656 ± 0.4
H4	R3*, R2*	1.750	2.90	1.91	yes	I	1.38 ± 0.05	2.673 ± 0.003	0.566 ± 0.003	19.938 ± 0.1
H4	R3*, R2*	1.750	2.95	1.91	yes	I	1.20 ± 0.02	2.724 ± 0.003	0.570 ± 0.004	19.712 ± 0.1
H4	R3*, R2*	1.750	3.00	1.87	yes	I	0.94 ± 0.02	2.777 ± 0.007	0.576 ± 0.007	19.309 ± 0.6
H4	R3*, R2*	1.750	3.10	1.66	yes	I	0.65 ± 0.05	2.877 ± 0.003	0.580 ± 0.003	19.156 ± 0.2

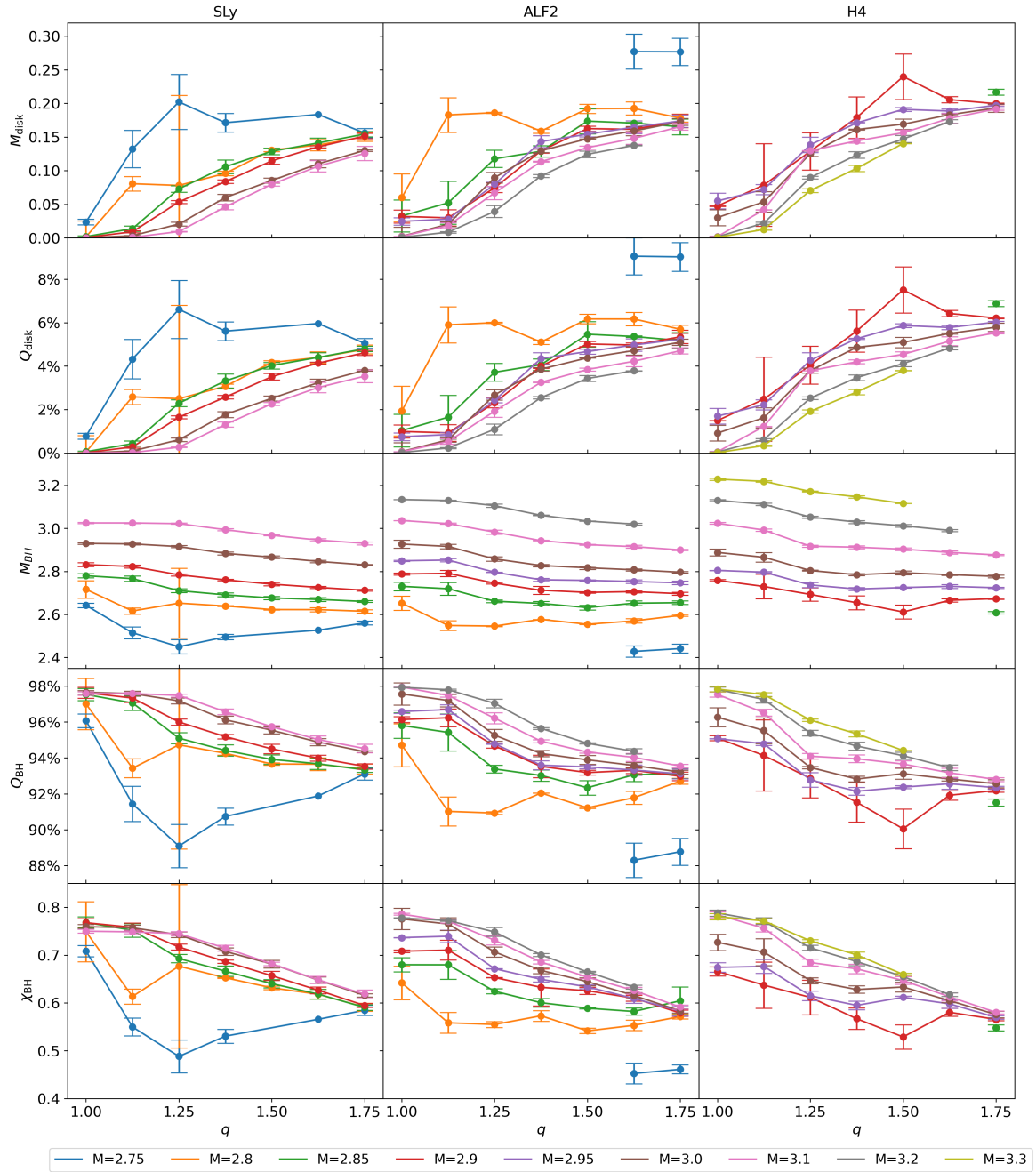


Figure 3.5: Properties of the remnant system. Displayed are the following quantities (rows): disk mass M_{disk} , the mass ratio $Q_{\text{disk}} = M_{\text{disk}}/M^b$, the BH mass M_{BH} , the mass ratio $Q_{\text{BH}} = M_{\text{BH}}/M$, and the BH spin χ_{BH} . Data are presented separately for different EOSs (columns). In each panel data for fix values of M are plotted against q . Second, third and fifth row taken from [Koe1].

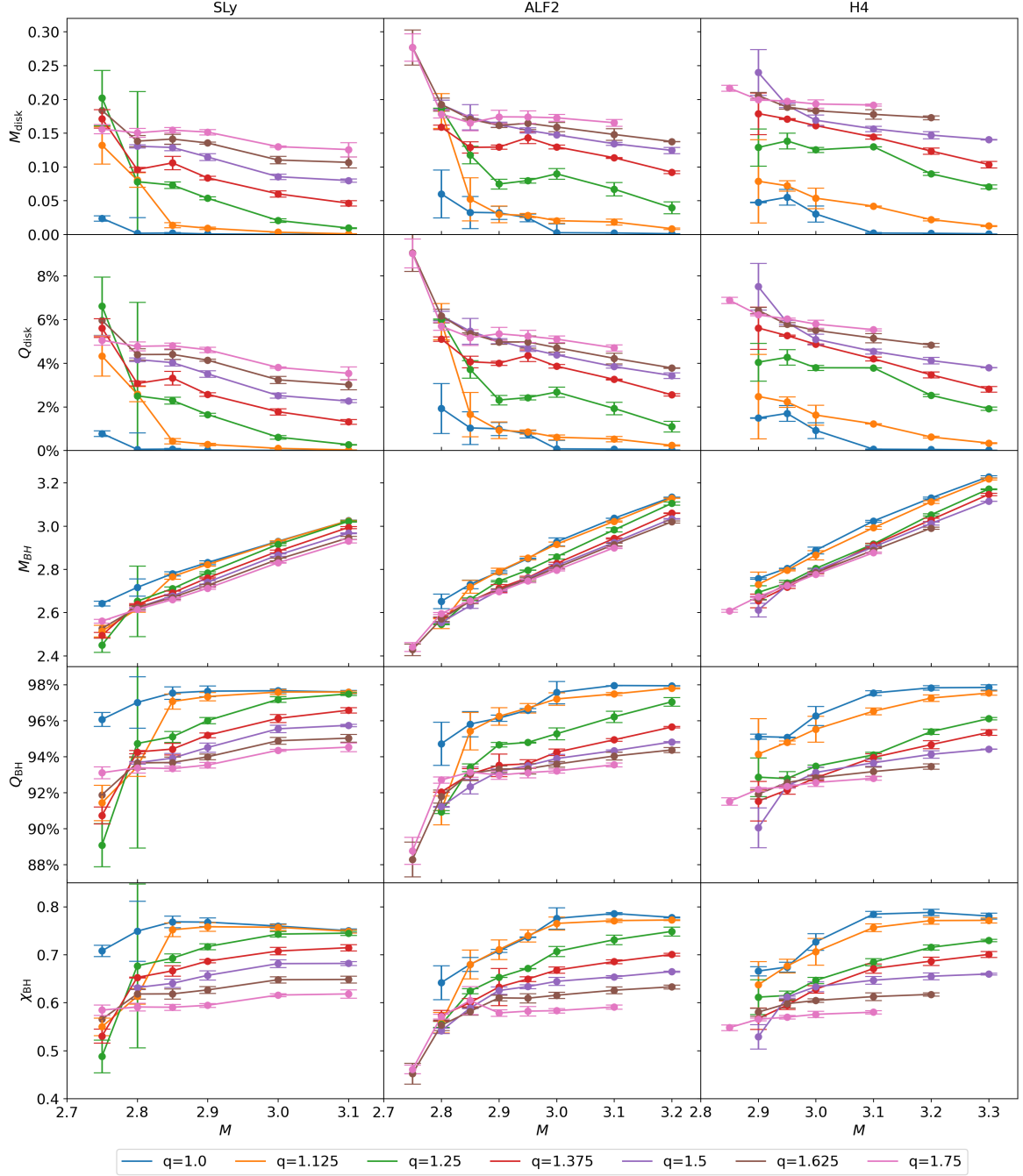


Figure 3.6: Properties of the remnant system. Columns and rows are organized as in Fig. 3.5. In each panel, data for fix values of q are plotted against M .

Chapter 4

Threshold to Prompt Collapse

4.1 BNS Mergers

Compact objects orbiting each other in a binary system, e.g. binary black holes (BBH), black hole-neutron star (BHNS) or BNS, slowly lose angular momentum due to the emission of gravitational waves, causing their orbital separation and their orbital periods to shrink over the course of millions of years. Towards the end of the inspiral phase, the process speeds up as frequency and amplitude of the emitted GWs increase, until the binary's components merge and the so-called *chirp* of the GW signal is followed by the *ringdown*. In the case of BNSs, the merger is usually accompanied by the release of NS matter which, in parts, is accumulated in a disk around the remnant or ejected from the system. Considering the remnant itself, we sketch three possible scenarios:

1. prompt collapse: The remnant collapses immediately after merger forming a BH.
2. delayed collapse: The differentially rotating NS remnant temporarily withstands its own gravitational pull before it eventually collapses.
3. long-lived/stable remnant: If the BNS's components are of sufficiently small mass, the differentially rotating remnant may transition to a uniformly rotating stable NS.

In this work, the first and second scenario will be of particular interest to us, i.e. we focus on scenarios in which the remnant collapses to a BH. In this context, we will consider a quantity studied with increasing interest and by means of numerous NR simulations (e.g. Hotokezaka et al., 2011; Bauswein et al., 2013; Köppel et al., 2019): the *threshold mass to prompt collapse*. The third scenario is not a subject of this work. For more detailed discussions of the third scenario, we refer the interested reader to Shibata et al., 2019 and Baiotti et al., 2017.

The dynamics of BNS mergers, the fate and properties of the merger remnant depend on a variety of factors. Primarily they are affected by the total mass of the prior binary, which is defined as the sum of the gravitational masses of the individual components

$$M = M_1 + M_2 , \quad (4.1)$$

and properties of dense matter. Other factors are the individual components' spins and their mass ratio

$$q = \frac{M_1}{M_2} \geq 1 . \quad (4.2)$$

While we exclusively consider non-spinning stars, i.e., leaving aside spin effects, the core topic of this work is the effect of mass ratio on BNS mergers. In this chapter we review relevant definitions and literature, criteria developed to distinguish between prompt and delayed collapse, and methods to determine the threshold mass to prompt collapse.

4.2 Collapse Time

Throughout this thesis, we usually examine BNS configurations which lead to BH formation within a few tens of milliseconds after merger. In the case of collapsing merger remnants, the remnant's *lifetime* is enclosed by two events: the onset of merger and the formation of a BH. We refer to the corresponding time interval, i.e., the time interval between the time of merger t_{mrg} , and the time of BH formation t_{BH} , as the *collapse time* t_{coll} ,

$$t_{\text{coll}} = t_{\text{BH}} - t_{\text{mrg}} . \quad (4.3)$$

While this definition is straightforward, it is less trivial to measure the collapse time. As discussed by Köppel et al., 2019, within numerical simulations, there is more than one way to determine either one the two times, t_{BH} and t_{mrg} . To give a rough idea of the possibilities: the different approaches may be based on GW data, i.e., the GW strain amplitude h (or the Weyl scalar Ψ_4), proper separation, the lapse α , or the first appearance of an apparent horizon, cf. Köppel et al., 2019. In this section, we discuss different possible approaches with respect to their automated and reliable applicability to a set of BNS simulations characterized by a broad range of mass ratios and total masses, in order to select a method for our analysis.

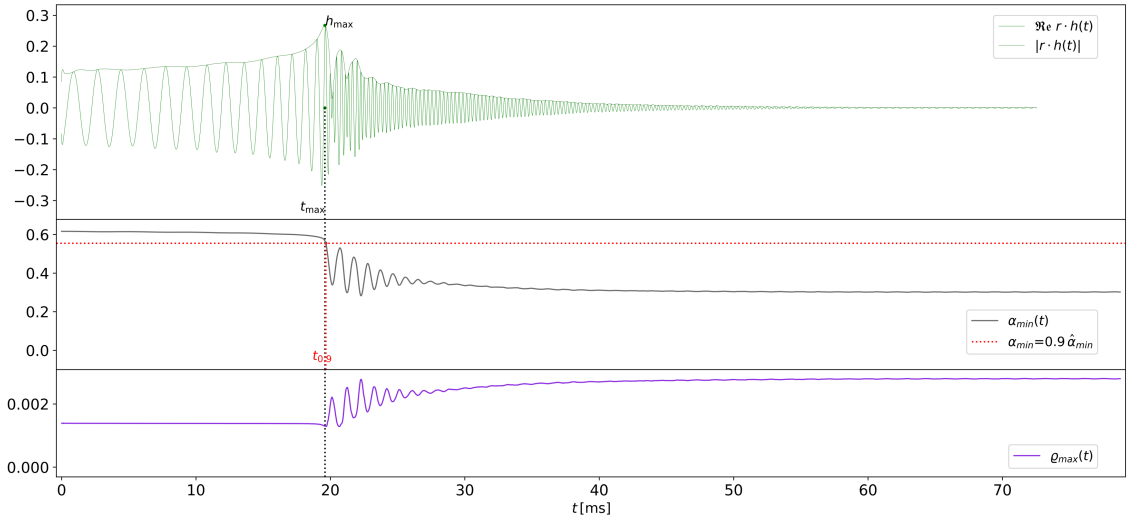
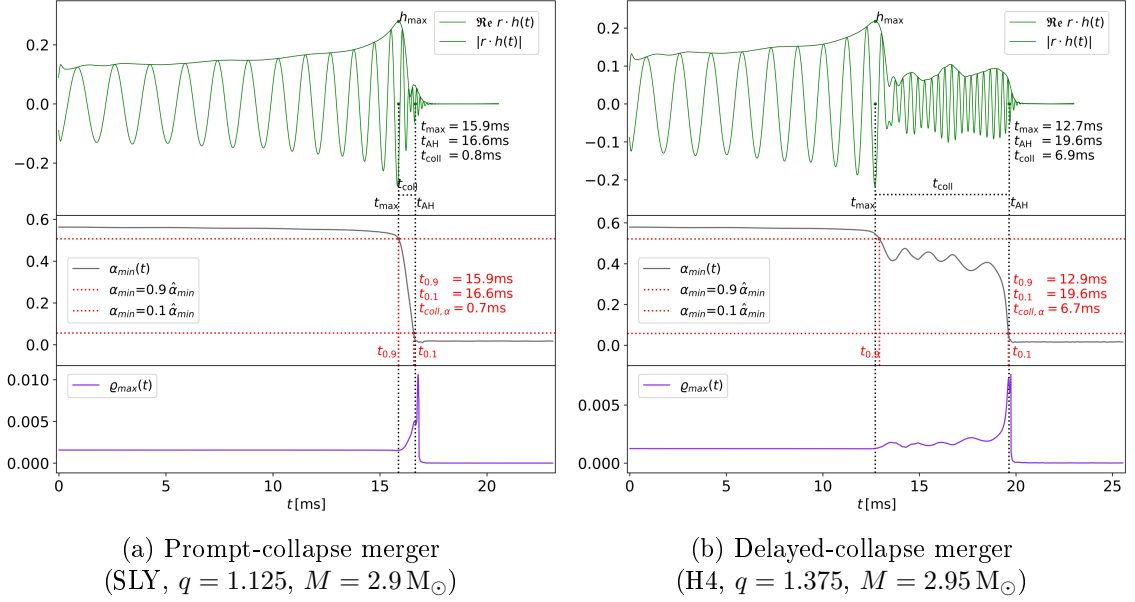


Figure 4.1: Subfigures (a)-(c): Examples for the cases of prompt and delayed collapse, and a stable remnant, respectively. In each of the subfigures (a)-(c), the top panel shows the 22-mode of the GW strain amplitude h (shifted according to an observer distance of 1477 km). Marked by black dotted lines are the time of first maximum t_{\max} , and the apparent horizon time t_{AH} . The middle panel shows the minimum-lapse function $\alpha_{\min}(t)$. Red dotted lines mark the times where $\alpha_{\min}(t)$ has fallen to 90% and 10% of the maximum value $\hat{\alpha}_{\min}$. Given in the bottom panel is the maximum-density function $\varrho_{\max}(t)$. Plots in subfigures (a) and (b) taken, (c) adapted from [Koe1].

To illustrate their perspective on this topic, we point out that Köppel et al., 2019, focussed on equal-mass binaries with masses close to the threshold mass. Since we study a parameter space covering broader ranges of q and M (cf. Chap. 3), we sometimes consider methods suggested in Köppel et al., 2019 from a different perspective.

Measuring the time of merger based on proper distance: As suggested by Köppel et al., 2019, the time of merger could be measured as the time when the stars' separation falls below a fraction of the initial diameter, or generalized to the case of unequal mass binaries: below a fraction of the sum of the components' radii. However, Köppel et al. point out, that this method would be very sensitive to properties of the EOS. As we consider unequal mass binaries, we are also confronted with tidal effects, i.e., tidal elongation or tidal disruption of the less massive component (cf. Sect. 6.3). These effects may affect this method strongly, as they can cause the localization of the stars' centres to decrease in reliability.

Estimating the time of collapse as the time when the ring-down signal starts: As pointed out by Köppel et al., the beginning of the ring-down is somewhat arbitrary and may be modified by infalling matter. This approach does not provide a reliable measure for the time of collapse. Measuring the time of merger on the other hand, a clear criterion for the onset of merger can be formulated based on the GW strain h , cf. Köppel et al., 2019. In this approach, which for example has also been taken by Agathos et al., 2020, the time of merger is identified with the time of first maximum of h or ψ_4 .

In this thesis, as in [Koe1], we choose the same path to determine the time of merger, identifying it with the time of first maximum of the dominant 22-mode of the GW strain. When it comes to the time of BH formation, we place our trust in BAM's apparent horizon finder, setting the search-frequency to a reasonably high rate. In summary, we calculate the collapse time (cf. Eq. 4.3) as the time interval between the time of first maximum t_{\max} of h_{22} , and the time t_{AH} when an apparent horizon is found for the first time, i.e.,

$$t_{\text{coll}} = t_{\text{AH}} - t_{\max} . \quad (4.4)$$

This method is illustrated in the upper panels of subfigures 4.1a and 4.1b, which show the 22-mode of h . In each of the figures, both the time of the GW strain's first maximum t_{\max} and the apparent horizon time t_{AH} are marked. To make a comparison of these times possible, the GW signal has been shifted according to the observer's distance r_{extr} from the source, cf. Eq. (2.53).

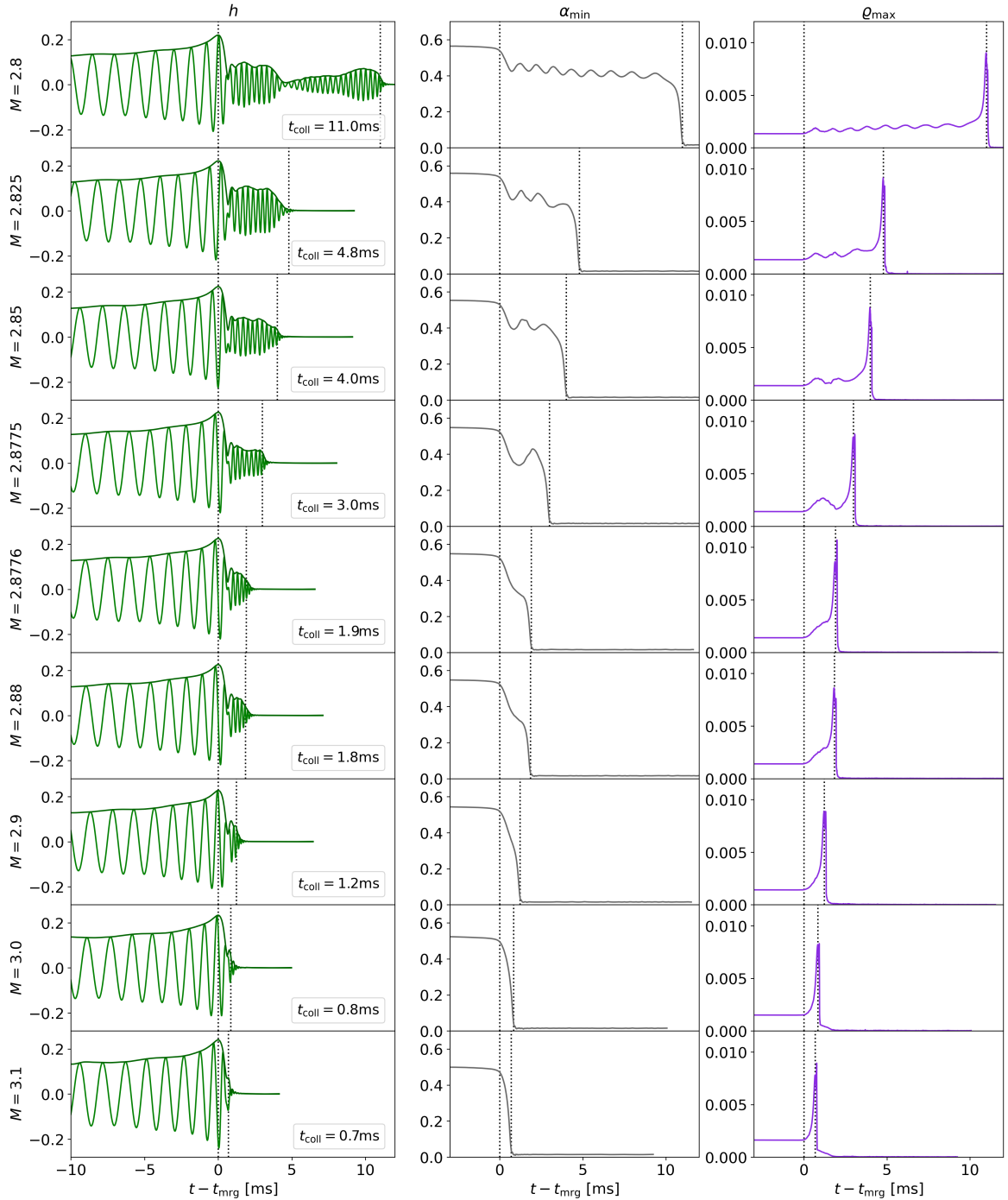


Figure 4.2: 22-mode of the gravitational wave strain, $h_{22}(t)$, minimum-lapse function $\alpha_{\min}(t)$ and maximum-density function $\rho_{\max}(t)$ for a sample of total masses M in the example case of ALF2 and a mass ratio of $q = 1.5$. Data of the complete set of simulations resolving the vicinity of the threshold mass, are given in Tab. 4.1. $h_{22}(t)$, $\alpha_{\min}(t)$ and $\rho_{\max}(t)$ are presented for a time interval covering about 10 ms before and after the onset of merger. Dotted vertical lines mark the time of merger t_{mrg} and the first time t_{AH} an apparent horizon was found. In the case of delayed-collapse mergers, minimum-lapse and maximum-density function show oscillations between t_{mrg} and t_{AH} . With increasing total mass, the number of oscillations decreases. Prompt collapse mergers are characterized by the absence of oscillations in these quantities.

For completeness, we discuss one more method to determine t_{coll} . The method used by Köppel et al., 2019, is based on the lapse. For irrotational equal-mass binaries, and in the context of 1+log slicing, they define two constant values, $\alpha_{\text{min}} = \alpha_{\text{merg}} = 0.35$, and $\alpha_{\text{min}} = \alpha_{\text{BH}} = 0.2$, corresponding to the times of merger and BH formation, respectively. Considering the examples given in the second column of Fig. 4.2, a naked-eye inspection reveals that, the lapse-method by Köppel et al. would systematically produce smaller collapse times compared to the collapse times given in the first column of Fig. 4.2, although we have used the same slicing conditions in our simulations. Since one may point out that data presented in Fig. 4.2 were not obtained for equal-mass binaries, we also refer to data of equal-mass binaries given in the first columns of Figs. A.2, A.5 and A.8, to support this argument.

The lack of applicability of the lapse-method to our data may be due to other differences in the NR codes used. Avoiding further speculation, we instead discuss an updated, more general, version of the lapse-method, which has been presented in a follow-up study by Tootle et al., 2021. Instead of absolute values for α_{min} , they consider the minimum-lapse function normalized to its maximum $\hat{\alpha}_{\text{min}}$, relating the time of merger and BH formation to $\alpha_{\text{min}}/\hat{\alpha}_{\text{min}} = 0.9$ and $\alpha_{\text{min}}/\hat{\alpha}_{\text{min}} = 0.1$, respectively. In the middle panels of subfigures 4.1a and 4.1b, this method is illustrated in comparison to the method used in [Koe1]. The comparison shows negligible differences of about 0.1 ms in the presented examples. Considering the set of simulations presented in [Koe1], we find the two methods to be consistent within this margin of error.

To conclude the discussion of lapse-based methods, we consider the two exemplary sets of data presented in Fig. 4.3. These data sets show the maximum of the minimum-lapse function and its value at $t = t_{\text{max}}$ in simulations of a given EOS (H4) and resolution (R3*, cf. Tab. 3.5). Over a broad range of total masses and mass ratios, the minimum-lapse function varies notably. Therefore, constant values of α_{min} cannot be used to determine the time of merger consistently over broad intervals of q and M . As Tootle et al., 2021, also considered unequal-mass binaries, they had to refine the method. Fig. 4.3 illustrates that the minimum-lapse function behaves similarly with respect to its maximum and to its value at $t = t_{\text{mrg}}$, making a fix value of the fraction $\alpha_{\text{min}}/\hat{\alpha}_{\text{min}}$ better suited to relate t_{mrg} to the minimum-lapse function. For the time of BH formation on the other hand, a connection to a fixed value of α_{min} is less problematic. t_{BH} would be insensitive to small changes of α_{BH} , since the minimum-lapse function decreases steeply when the remnant collapses, cf. middle panels of subfigures 4.1a and 4.1b.

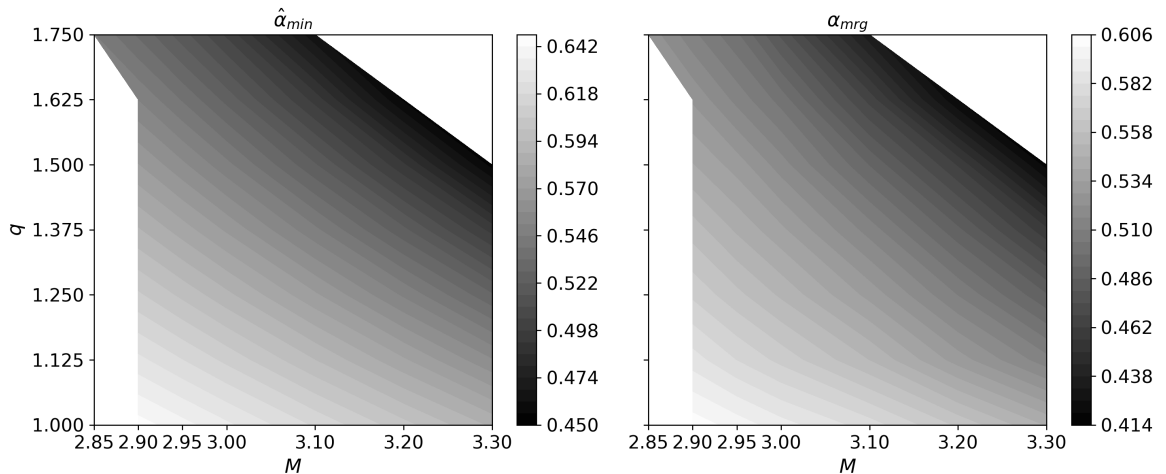


Figure 4.3: Contours of the minimum-lapse function α in the (M, q) -plane for two exemplary cases. Presented are data for the case of H4 with resolution R3*. The first column shows the maximum value $\hat{\alpha}_{min}$ of $\alpha_{min}(t)$, the second column shows the value α_{mrg} at the time of merger (given by $t = t_{max}$).

4.3 Threshold Mass, Prompt and Delayed Collapse

4.3.1 Threshold Mass to Prompt Collapse

As defined by Bauswein et al., 2013, the threshold mass M_{thr} separates the two scenarios of prompt and delayed collapse, i.e., M_{thr} is the smallest total mass for which the remnant of a BNS merger collapses promptly after the onset of merger. Total masses $M < M_{thr}$ either lead to delayed-collapse scenarios, in which an unstable NS remnant collapses to a BH after angular momentum losses and cooling (e.g. Hotokezaka et al., 2011), or they lead to the formation of a stable MNS in case of sufficiently small M . M_{thr} depends both on properties of dense matter, i.e., on the EOS, and on properties of the binary system like the mass ratio q (e.g. Bauswein et al., 2021), NS spins χ_i (e.g. Tootle et al., 2021), and possibly also spin orientation or eccentricity, i.e.

$$M_{thr} = M_{thr}(\text{EOS}, q, \chi_i, \dots) . \quad (4.5)$$

The effect of mass ratio (e.g. Ref. [Koe1], Bauswein et al., 2021; Perego et al., 2021) and the effect of spin (Tootle et al., 2021) have been found a minor factor compared to the EOS-dependence of M_{thr} , which has first been studied in the case of equal mass binaries (e.g. Hotokezaka et al., 2011; Bauswein et al., 2013; Köppel et al., 2019). Throughout this thesis, we focus on the effects of the mass ratio, i.e., typically the following dependencies are implied, *i.e.*, $M_{thr} = M_{thr}(\text{EOS}, q)$.

The EOS dependence of the threshold mass makes BNS mergers a unique lab for the study of dense matter. How future GW detections of BNS mergers will further constrain the EOS of NSs based on the distinction between prompt and delayed collapse, has recently been investigated thoroughly in a study by Kashyap et al., 2021. Their study is based on simulations of irrotational equal-mass binaries and data from millions of piecewise polytropic EOSs.

4.3.2 Prompt and Delayed Collapse in NR Simulations

In the context of NR simulations, the scenarios of prompt and delayed collapse are distinguished based on the behaviour of the density (e.g. Hotokezaka et al., 2011; Bernuzzi, 2020), or the lapse, Bauswein et al., 2021. The case of prompt collapse is characterized by the absence of oscillations in the maximum-density function $\varrho_{\max}(t)$, i.e., the monotonous increase of the central density, in the time interval between merger and collapse to a BH (cf. Fig. 4.1a, bottom panel). This is equivalent to defining prompt-collapse mergers as those in which the collision of the NSs' cores has no bounce, cf. discussion in Bernuzzi, 2020 or Radice et al., 2018a. In the case of delayed-collapse mergers on the other hand, the cores' bounce is followed by oscillations of the remnant visible in the maximum-density function (cf. Fig. 4.1b, bottom panel). A criterion similar to the one for the maximum-density can be formulated for the minimum-lapse function, e.g. Bauswein et al., 2021. Considering the minimum-lapse function $\alpha_{\min}(t)$ instead of the central density, we find α_{\min} to decrease monotonously in the time interval between merger and BH formation, showing the same number of oscillations that are found in the maximum-density function (cf. Figs. 4.1b and 4.1a, bottom and middle panel). In summary, we refer to a collapse as prompt if, on a dynamical time scale, there are no oscillations of $\varrho_{\max}(t)$ or $\alpha_{\min}(t)$ in the time interval between t_{mrg} and t_{BH} , and delayed in the complementary case.

A distinction between prompt and delayed collapse may also be based on the collapse time (cf. for example Agathos et al., 2020 or Ref. [Koe1]), i.e., BNS mergers are considered prompt if the collapse time is smaller than a threshold value. If the collapse time is larger than the threshold value, it is considered a delayed collapse. We motivate this approach in Sect. 4.4.1. In this context, we need to mention Bauswein et al., 2013, who relate prompt (delayed) collapse to a *dynamical* (*secular*) time scale, respectively. Considering also NS remnants which do not collapse promptly, different cases can be distinguished. Radice et al., 2018c, categorize remnant NSs with respect

to the maximum baryonic mass of a rigidly rotating NS $M_{\max}^{\text{b,rot}}$, and the maximum baryonic mass of a non-rotating NS M_{\max}^{b} :

$$\text{HMNS: } M^{\text{b}} > M_{\max}^{\text{b,rot}}$$

$$\text{SMNS: } M_{\max}^{\text{b,rot}} > M^{\text{b}} > M_{\max}^{\text{b}}$$

$$\text{MNS: } M_{\max}^{\text{b}} > M^{\text{b}}$$

The BNSs which we consider in this work have gravitational masses with $M > M_{\max}^{\text{rot}}$. So their remnants are likely to collapse within simulation time. In a minority of cases, we encounter long-lived remnants like the one portrayed in Fig. 4.1c. In these cases, we find oscillations of the remnant to wear off, and $\varrho_{\max}(t)$ and $\alpha_{\min}(t)$ to stabilize. The initial levels of $\varrho_{\max}(t)$ and $\alpha_{\min}(t)$ are related to the mass of the primary component, the respective stable levels after merger are connected to the mass of the coalesced NS. Therefore, the maximum-density function stabilizes at a notably higher value, the minimum-lapse function on a notably smaller value, as compared to the respective initial values. In accordance with this stabilization, we find the amplitude of h_{22} to subside over a course of tens of milliseconds.

4.3.3 Bracketing Method

The threshold-mass definition by Bauswein et al., 2013, cf. Sect. 4.3.1, provides a natural means to localize M_{thr} : The bracketing method is the approach which is typically used to determine the threshold mass to prompt collapse, e.g. Hotokezaka et al., 2011; Bauswein et al., 2013; Bauswein et al., 2021; Kashyap et al., 2021; Perego et al., 2021. Leaving other parameters constant, the total mass is varied to narrow down the interval between the smallest total mass inducing prompt collapse M_{\min}^{prompt} , and the highest total mass leading to delayed collapse $M_{\max}^{\text{delayed}}$, i.e.,

$$M_{\max}^{\text{delayed}} \leq M_{\text{thr}} < M_{\min}^{\text{prompt}} . \quad (4.6)$$

In the context of the bracketing method, the threshold mass $M_{\text{thr}}^{[\]}$ is defined as the mean value

$$M_{\text{thr}}^{[\]} = 0.5(M_{\max}^{\text{delayed}} + M_{\min}^{\text{prompt}}) , \quad (4.7)$$

cf. for example Bauswein et al., 2013. As in Eq. (4.5), the quantities in inequality (4.6) and equation (4.7) may depend on the EOS and properties of the binary.

4.4 Methods Based on Collapse-Time Fits

Apart from the bracketing method, we will review two more approaches to determine M_{thr} . Concluding this section, we will first review the method by Köppel et al., 2019, which has also been used by Tootle et al., 2021. In Sect. 4.4.1, we will compare this method to the one introduced in Ref. [Koe1]. However, since both of these methods are based on fits of collapse-time data, we should first consider Fig. 4.4a, which shows the collapse-time as a function of the total mass for the case of ALF2 with $q = 1.5$. Overall we find t_{coll} to decrease for increasing M , with a change of slope between roughly $M = 2.8 M_{\odot}$ and $M = 2.95 M_{\odot}$. For now, we limit our focus to this range. At roughly $M \approx 2.88 M_{\odot}$ the collapse time decreases steeply over a narrow interval in M . This sensitivity of $t_{\text{coll}}(M)$ to small changes of M has also been described by Bauswein et al., 2013. Köppel et al., 2019, use data points from this regime of steep changes of t_{coll} to fit M/M_{TOV} as a function of $t_{\text{coll}}/\tau_{\text{TOV}}$, where for a given EOS the constants M_{TOV} and τ_{TOV} are the mass and the free-fall time of a maximum-mass TOV configuration, cf. Fig. 2 of Köppel et al., 2019. This fit is then used to extrapolate to $t_{\text{coll}}/\tau_{\text{TOV}} = 1$, which is why Tootle et al., 2021, call this method the *free-fall method*. Köppel et al. motivate this procedure by stating that for BNSs with $M = M_{\text{thr}}$ the merger remnant would collapse over the shortest possible time scale, given by the free-fall time, i.e., $t_{\text{coll}}(M = M_{\text{thr}}) = \tau_{\text{TOV}}$. In this context, they define the threshold mass by the condition

$$M \rightarrow M_{\text{thr}} \text{ for } t_{\text{coll}} \rightarrow \tau_{\text{TOV}} . \quad (4.8)$$

As pointed out in Ref. [Koe1], typical free-fall times of maximum-mass TOV stars (about 0.1 ms) are noticeably smaller than the smallest collapse times found in simulations, even in the case of binaries with $M \gg M_{\text{thr}}$. Nevertheless, this method locates M_{thr} at masses slightly larger than the highest mass of the steep regime considered for the fit. As we discuss in Sect. 5.3, the threshold mass $M_{\text{thr}}^{\text{ff}}$ as determined by the free-fall method, is systematically placed at masses higher than the threshold mass M_{thr}^{\square} , determined by application of the bracketing method to the same set of data, i.e.,

$$M_{\text{thr}}^{\text{ff}} > M_{\text{thr}}^{\square} . \quad (4.9)$$

However, considering threshold masses determined for EOSs used in either work, a direct comparison of results by Köppel et al., 2019 to results by Bauswein et al., 2021 shows only small differences, cf. discussion in [Koe1].

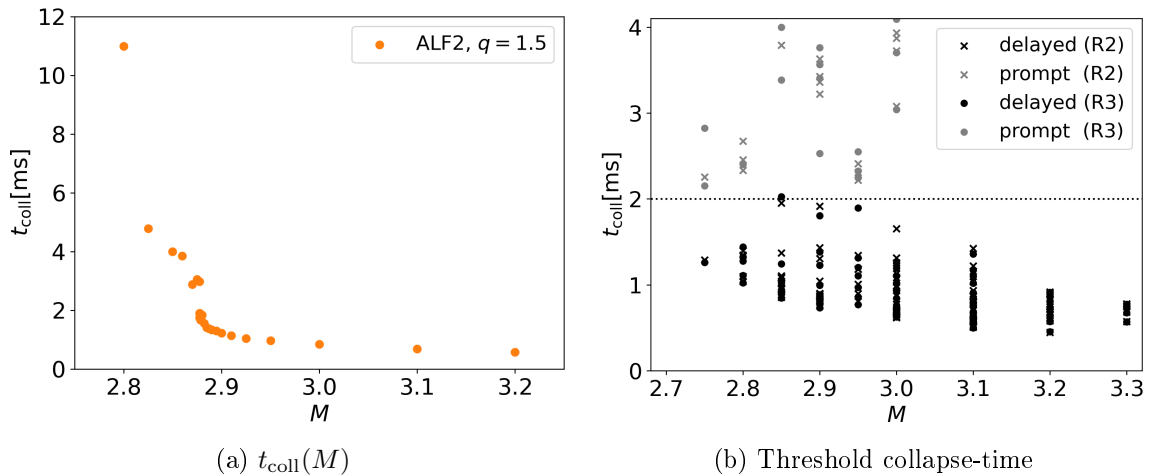


Figure 4.4: Subfigure (A): Collapse time against total mass for the case of ALF2 with $q = 1.5$. For increasing M , t_{coll} decreases, levelling off for high total masses. Between roughly $M = 2.8 M_{\odot}$ and $M = 2.95 M_{\odot}$ the collapse time changes its slope, decreasing steeply at $M \sim 2.88 M_{\odot}$. Subfigure (B): Close-up to a subset of more than 260 BNS simulations from [Koe1] in which a BH formed within simulation time. Depicted is the collapse-time interval $2 \text{ ms} \pm 2 \text{ ms}$. Data are distinguished with respect to resolution (cf. Tab. 3.5, i.e., R2/R2* (crosses) and R3/R3* (points)), and whether the collapse was prompt (black) or delayed (gray) according to the lapse and density criteria. Independent of resolution and EOS (not highlighted: SLy, ALF2, H4), the cases of prompt collapse and delayed collapse are separated by the dashed line at $t_{\text{coll}} = 2 \text{ ms}$. Plot in subfigure (A) adapted from [Koe1].

4.4.1 Threshold Collapse Time

We are going to consider once more the finely resolved collapse-time curve $t_{\text{coll}}(M)$ shown in Fig. 4.4a, focussing our attention on the steeply decreasing regime at $M \approx 2.88 M_{\odot}$. As implied in the previous section, this is where the threshold mass is localized by application of the bracketing method to the portrayed set of data. In fact this steep decent marks the transition from delayed to prompt collapse. We are going to show this, giving a thorough analysis of the related data and refining the respective discussion of Ref. [Koe1].

We begin by categorizing the related BNS mergers in terms of prompt and delayed collapse, applying the criteria from Sect. 4.3.2 to the minimum-lapse and maximum-density curves. A sample of these curves is presented in Fig. 4.2 next to the related h_{22} data. Data of the full set of simulations conducted for the case of ALF2 with $q = 1.5$ are given in Tab. 4.1, where the number of maxima N_{max} between merger and collapse, and the consequential categorization of the BNS mergers are reported in columns nine and ten, respectively.

In this Tab. 4.1, the transition from delayed-collapse to prompt-collapse mergers is marked by dashed lines enclosing an interval of inconclusive cases which lead to prompt collapse simulated with R3 resolution and to delayed collapse simulated with R2 resolution. Attempting to honour results of both resolutions, we localize M_{thr} between $M_{\text{max}}^{\text{delayed}} = 2.8775 M_{\odot}$ and $M_{\text{min}}^{\text{prompt}} = 2.885 M_{\odot}$ based on the bracketing method, cf. dotted lines in Tab. 4.1.

We point out that, within the presented set of simulations, the case of prompt collapse is always related to a collapse time smaller than 2 ms, while in the case of delayed collapse, the collapse time is always higher than 2 ms. The same observation is true for the data set presented in Ref. [Koe1]. To highlight this relation, we show collapse-time data of R3 and R2 simulations in Fig. 4.4b, distinguishing between prompt-collapse and delayed-collapse mergers based on the lapse/density criteria. Irrespective of the mass ratio, the resolution, or the EOS, we find collapse-times smaller than 2 ms related to prompt-collapse simulations, while collapse-times larger than 2 ms are connected to delayed-collapse data.

Further, we note that in the vicinity of the threshold mass, the collapse-time curve changes its slope noticeably. Reversely to the steep decrease of t_{coll} at $M \approx M_{\text{thr}}$, M is insensitive to change of t_{coll} . Therefore, within a certain tolerance, it is possible to define a *threshold collapse-time* τ_{thr} characterized by

$$t_{\text{coll}}(M_{\text{thr}}) = \tau_{\text{thr}} , \quad (4.10)$$

which separates the cases of prompt and delayed collapse based on t_{coll} . In Ref. [Koe1], we defined this threshold collapse-time to be 2 ms, i.e.,

$$\tau_{\text{thr}} = 2 \text{ ms} , \quad (4.11)$$

which is a choice, that has also been made by Agathos et al., 2020. Concluding from Fig. 4.4b, we may as well draw this line at a collapse time slightly larger than 2 ms. However, due to the insensitivity of M_{thr} to small changes of this value, we do not attempt to determine τ_{thr} more precisely, nor do we imply that there is an exact value of τ_{thr} universal for all EOSs.

Table 4.1: Series of simulations resolving the vicinity of the threshold to prompt collapse in the case of $q = 1.5$ with EOS ALF2. Additional to the simulations conducted for the simulation campaign presented in chapter 3, 20 configurations have been simulated with two resolutions (R3 and R2). Adding configurations, new total masses were chosen based on previous simulations seeking to narrow down the interval between prompt-collapse and delayed-collapse cases. Columns one to four characterize the simulations in terms of EOS, resolution (res), mass ratio (q) and total mass (M). Residual eccentricities are given in column five. Column six: Formation of a BH within simulation time. The categorization of the merger types in column eight is based on the collapse times given in column seven, cf. Sect. 4.6. Column ten: Categorization of mergers as prompt or delayed based on N_{\max} , the number of minima of the minimum-lapse/ maxima of the maximum-density function within the time interval between t_{mrg} and t_{AH} , given in column nine.

EOS	res	q	M [M_{\odot}]	ecc [10^{-2}]	BH	$t_{\text{coll}}^{\text{R3}}$ [ms]	$t_{\text{coll}}^{\text{R2}}$ [ms]	Type	N_{\max}	Collapse
ALF2	R3, R2	1.5	2.80000	1.53	yes	10.99	7.29	III	8/5	delayed
ALF2	R3, R2	1.5	2.82500	1.63	yes	4.79	6.07	II/III	3/4	delayed
ALF2	R3, R2	1.5	2.85000	1.73	yes	4.00	3.79	II	2	delayed
ALF2	R3, R2	1.5	2.86000	1.76	yes	3.85	4.31	II	2	delayed
ALF2	R3, R2	1.5	2.87000	1.78	yes	2.88	2.71	II	1	delayed
ALF2	R3, R2	1.5	2.87500	1.78	yes	3.05	3.02	II	1	delayed
ALF2	R3, R2	1.5	2.87750	1.79	yes	2.98	2.82	II	1	delayed
ALF2	R3, R2	1.5	2.87760	1.79	yes	1.90	2.63	I/II	0/1	?
ALF2	R3, R2	1.5	2.87770	1.79	yes	1.75	2.84	I/II	0/1	?
ALF2	R3, R2	1.5	2.87780	1.79	yes	1.90	2.65	I/II	0/1	?
ALF2	R3, R2	1.5	2.87790	1.79	yes	1.73	3.24	I/II	0/1	?
ALF2	R3, R2	1.5	2.87800	1.79	yes	1.74	2.86	I/II	0/1	?
ALF2	R3, R2	1.5	2.87850	1.79	yes	1.66	2.67	I/II	0/1	?
ALF2	R3, R2	1.5	2.87900	1.79	yes	1.69	2.78	I/II	0/1	?
ALF2	R3, R2	1.5	2.88000	1.80	yes	1.84	2.61	I/II	0/1	?
ALF2	R3, R2	1.5	2.88250	1.81	yes	1.56	2.59	I/II	0/1	?
ALF2	R3, R2	1.5	2.88500	1.82	yes	1.41	1.85	I	0	prompt
ALF2	R3, R2	1.5	2.88750	1.82	yes	1.38	1.77	I	0	prompt
ALF2	R3, R2	1.5	2.89000	1.83	yes	1.33	1.45	I	0	prompt
ALF2	R3, R2	1.5	2.89500	1.84	yes	1.30	1.39	I	0	prompt
ALF2	R3, R2	1.5	2.90000	1.84	yes	1.23	1.31	I	0	prompt
ALF2	R3, R2	1.5	2.91000	1.86	yes	1.14	1.23	I	0	prompt
ALF2	R3, R2	1.5	2.92500	1.87	yes	1.04	1.11	I	0	prompt
ALF2	R3, R2	1.5	2.95000	1.89	yes	0.97	1.00	I	0	prompt
ALF2	R3, R2	1.5	3.00000	1.92	yes	0.84	0.87	I	0	prompt
ALF2	R3, R2	1.5	3.10000	1.87	yes	0.69	0.71	I	0	prompt
ALF2	R3, R2	1.5	3.20000	1.73	yes	0.58	0.58	I	0	prompt

4.4.2 Collapse-Time Fits

The definition of a threshold collapse-time is an important part of the threshold-mass method introduced in Ref. [Koe1]. This method has similar, yet different, building blocks compared to the method by Köppel et al., 2019: While Köppel et al. relate M_{thr} to the free-fall time by means of extrapolation based on data points with $M \approx M_{\text{thr}}$, we use a fit of collapse-time data related to a broad range of total masses to find M_{thr} by means of interpolation, cf. Fig. 4.5a. While we fit t_{coll} as a function of M , Köppel et al., 2019, consider dimensionless quantities, fitting M/M_{TOV} as a function of $t_{\text{coll}}/\tau_{\text{TOV}}$, as illustrated in Fig. 4.5b. Their method is based on data points with $M \approx M_{\text{thr}}$ and a Gaussian fit function of the form

$$M/M_{\text{max}} = \tilde{a} \exp \left[-\tilde{b} (t_{\text{coll}}/\tau_{\text{TOV}})^2 \right], \quad (4.12)$$

where τ_{TOV} is the EOS-dependent free-fall time of a maximum mass configuration. In the given example, we apply the free-fall method to a subset of our (ALF2, $q = 1.5$) data, employing R3 data of prompt-collapse and delayed-collapse mergers with small differences in M . As highlighted in Fig. 4.5b, we base our method on data with a typical separation of $\Delta M = 0.1 M_{\odot}$ and a minimal separation of $\Delta M = 0.05 M_{\odot}$, cf. Sect. 5.2.1. Both of the compared methods ignore parts of the collapse-time curve.

A detailed discussion of our fitting procedure is given in Sect. 5.2.3. We may take a moment to reflect upon the two methods which are portrayed in Fig. 4.5. At first glance one may conclude that the method depicted on the right is computationally cheaper as the fit is based on only four data points. In practice one probably has to conduct more than a handful of simulations to obtain points to the left of the second dotted line to find suitable data, as we will discuss in Sect. 5.3. We point out, that the free-fall method is especially sensitive to data of the prompt-collapse regime. Provided that data sufficiently close to the threshold have been found, i.e. prompt-collapse and delayed-collapse data with little difference in M , we expect the free-fall method and the bracketing method to be more robust compared to the method introduced in Ref. [Koe1]. We point out that provided with this kind of data, the same fit may be used to determine M_{thr} by interpolation instead of extrapolation. In Fig. 4.5b, this alternative approach based on the threshold collapse-time (Eq. 4.11) is indicated by the second dotted line. In Sect. 5.3, we discuss whether this change of procedure can provide results for M_{thr} that satisfy Eq. 4.6. Furthermore, we discuss an alternative idea for a fit of data with $M \approx M_{\text{thr}}$. A discussion of our own method is given in Sect. 5.2.4.

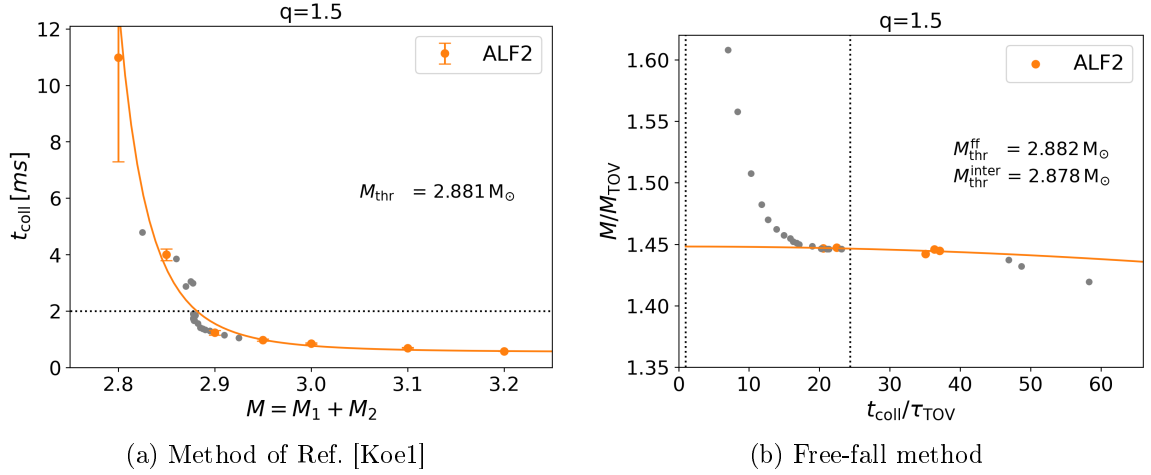


Figure 4.5: Comparison of methods based on the example data set from Tab. 4.1. Panel (A): Method introduced in Ref. [Koe1]; t_{coll} as a function of M . The fit is based on data for a broad range of total masses with a minimal separation of $\Delta M = 0.05 M_{\odot}$. The threshold mass is determined by interpolation, intersecting the fit curve with the dotted ($t_{\text{coll}} = \tau_{\text{thr}}$)-line. Panel (B): Free-fall method by Köppel et al., 2019; M/M_{TOV} as a function of $t_{\text{coll}}/\tau_{\text{TOV}}$. The threshold mass $M_{\text{thr}}^{\text{ff}}$ is determined by extrapolation to $t_{\text{coll}}/\tau_{\text{TOV}}$ (left dotted line) based on an exponential fit of data with $M \approx M_{\text{thr}}$. Using the same fit, the threshold mass $M_{\text{thr}}^{\text{inter}}$ may be determined by interpolation at $t_{\text{coll}}/\tau_{\text{TOV}} = \tau_{\text{thr}}/\tau_{\text{TOV}}$ (second dotted line). In both panels points not used for the fit are marked with gray color. Plot in subfigure (A) adapted from [Koe1].

4.5 Threshold Mass Coefficient k_{thr}

The threshold mass coefficient k_{thr} is defined as the fraction

$$k_{\text{thr}} = \frac{M_{\text{thr}}}{M_{\text{max}}} , \quad (4.13)$$

where $M_{\text{max}} = M_{\text{max}}(\text{EOS})$ is the maximum mass of an isolated non-rotating NS. Various studies relate M_{thr} to M_{max} in this way, for example Hotokezaka et al., 2011; Bauswein et al., 2013; Köppel et al., 2019; Kashyap et al., 2021. The coefficient k_{thr} has been found to be limited to the interval

$$1.3 \lesssim k_{\text{thr}}(q = 1) \lesssim 1.7 , \quad (4.14)$$

e.g., Hotokezaka et al., 2011; Bauswein et al., 2013; Radice et al., 2018c; Agathos et al., 2020. Including unequal mass binaries, Eq. 4.13 becomes

$$M_{\text{thr}}(\text{EOS}, q) = k_{\text{thr}}(\text{EOS}, q) \cdot M_{\text{max}} . \quad (4.15)$$

Investigating the effect of mass ratio on the threshold mass, neither Perego et al., 2021, nor Ref. [Koe1] find Eq. (4.14) to be violated, although broad mass ratio interval were considered. The large set of EOSs studied by Bauswein et al., 2021 on the other hand contains threshold mass coefficients in the range $1.258 \leq k_{\text{thr}} \leq 1.580$.

4.6 Collapse Types

We categorize BNS mergers based on the lifetime of the remnant, distinguishing between four merger types: prompt-collapse mergers (type I), delayed-collapse mergers (type II, III), and long-lived remnants which did not collapse within simulation time (type IV).

- Type I: prompt collapse ($t_{\text{coll}} < \tau_{\text{thr}}$)
- Type II: short-lived HMNS ($\tau_{\text{thr}} < t_{\text{coll}} < 5 \text{ ms}$)
- Type III: long-lived remnants ($t_{\text{coll}} > 5 \text{ ms}$)
- Type IV: long-lived remnants (no collapse within simulation time)

This classification is an extension of a classification originally used by Hotokezaka et al., 2011. In Ref. [Koe1] we specified the distinction between type I and type II in relation to the threshold collapse time, and added type IV for convenience.

Chapter 5

Collapse Time Fits and Threshold Mass

In this chapter, after a discussion of mass-ratio effects on the collapse time (Sect. 5.1), we take up the discussion on methods to determine M_{thr} based on collapse time data, which we started in Sect. 4.4.2. With respect to the method introduced in Ref. [Koe1], we take a closer look at the building blocks of the threshold mass that remain to be discussed (Sect. 5.2). Once more, we make use of the example data-set (ALF2, $q = 1.5$) as a test bed, taking the respective value of M_{thr} obtained by bracketing as a reference (Sect. 5.2.4). Furthermore, we use this set of data to examine the free-fall method by Köppel et al., 2019. As mentioned in Sect. 4.4.2 and demonstrated in Fig. 4.5, the same fit function and data may be used to determine M_{thr} by means of interpolation instead of extrapolation. We are going to explore this idea. Finally, we investigate ideas for alternative fits of data close to threshold (Sect. 5.3).

5.1 Collapse Time - The Effect of Mass Ratio

In Sect. 4.4, based on an example case with given EOS and mass ratio, we have discussed the relation between the collapse time t_{coll} and the total mass M focussing on the behaviour of t_{coll} in the vicinity of M_{thr} . However, resolving the sensitive dependence of the collapse time on small changes of total masses close to the threshold mass is a costly endeavour which we did not undertake in the simulation campaign of Ref. [Koe1], cf. Chap. 3. Instead we settled for a structured parameter-grid spanned by sets of mass ratios and total masses, which allowed us to explore properties of merger remnants over a broader range of total masses compared to the small window provided by data with $M \approx M_{\text{thr}}$.

Fig. 5.1 shows the dependence of t_{coll} on both q and M . The figure is split in two rows to properly present both small (lower row) and high collapse times (upper row). Over the full range of considered mass ratios, we rediscover the qualitative relation between t_{coll} and M which we encountered in the example case of the ALF2 with $q = 1.5$: For a given mass ratio, the collapse time decreases with increasing total mass. For a given total mass on the other hand, the picture is more diverse. In the case of the highest simulated total masses, the effect of q is relatively small, affecting t_{coll} to decrease for high q (ALF2, H4) or to develop a maximum at an intermediate mass ratio (SLy). In the case of the smallest simulated total masses on the other hand, the collapse-time curve has at least one maximum and does not appear to follow a systematic rule. The existence of a maximum at intermediate mass ratios may be the result of competing effects. Considering the edges of the studied mass-ratio interval, we find high mass ratios to reduce t_{coll} , while close to $q = 1$, t_{coll} increases with increasing asymmetry. As we are going to discuss in Sect. 6.3, increasing q leads to increasing deformations of the secondary component, cf. Fig. 6.7. This probably decreases the strength of the star cores' impact, causing the merger remnant's lifetime to increase. At high mass ratios on the other hand, another effect dominates: Almost all of the simulated total masses induced collapse within 2 ms in case of highly asymmetric binaries¹, causing $t_{\text{coll}}(q)$ to decrease with increasing q . Considering the binary's more massive component (M_1) in the case of high q , this comes with little surprise as the primary star is already highly compact (with M_1 reaching values close to M_{max}). In summary these two effects cause $t_{\text{coll}}(q)$ to fall off towards the endpoints of the investigated mass-ratio interval, providing for at least one maximum at intermediate mass ratios. At high M , we find the second effect to dominate.

The depicted error bars are determined as the difference between results of the respective highest and second highest simulated resolution. Typically these are R3(*) and R2(*). These differences appear to be larger for smaller M . Alternatively stated, higher collapse times are less certainly determined compared to small ones. This is due to the more complicated dynamics in connection with HMNS remnants. One extreme case in this context is the SLy configuration with $M = 2.8 M_{\odot}$ and $q = 1.25$. The collapse times are 15 ms (R3) and 2.3 ms (R2). Seeking to determine this data point more precisely, we conducted an R4 simulation for this configuration, obtaining a collapse time of 2.5 ms and an error bar of almost the same size.

¹Performing additional simulations of low-mass configurations exclusively in the case of $q \in \{1.625, 1.75\}$, it was possible to add a small number of data points with $t_{\text{coll}} > 2$ ms in the regime of high mass ratios, e.g. in the case of ALF2 and $M = 2.75$.

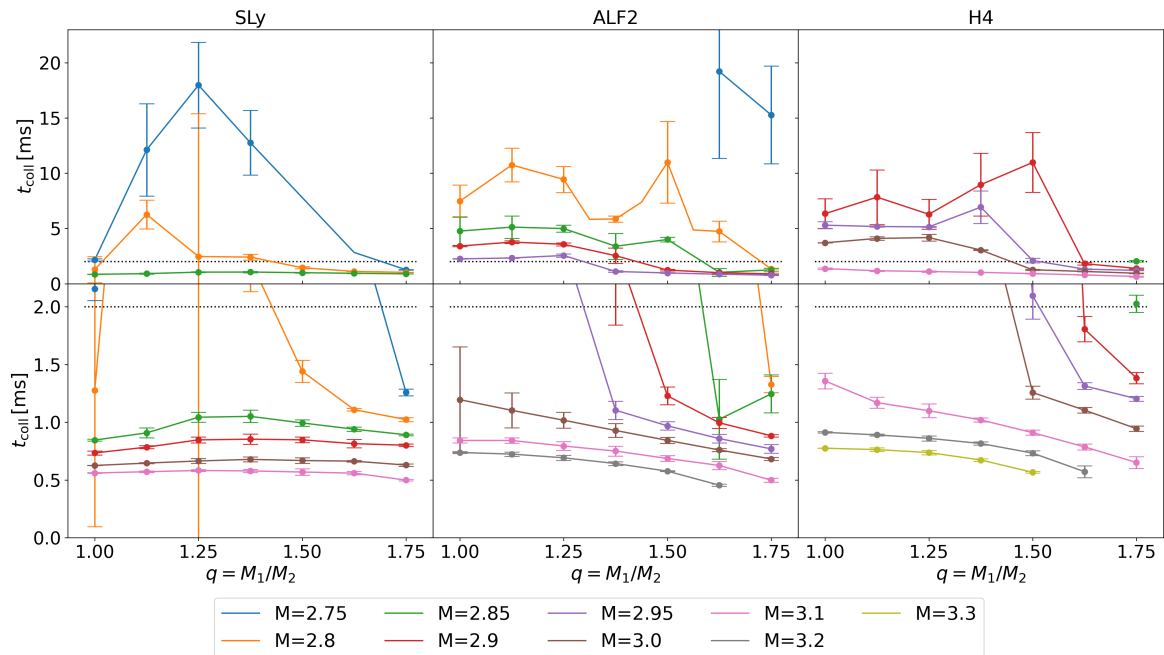


Figure 5.1: t_{coll} as a function of q for different total masses M . Columns: Data subsets defined by the EOS. The curves either decrease for increasing M or show a maximum for $q > 1$. For fixed mass ratio, t_{coll} decreases when we increase the total mass M . First row: Full range of t_{coll} . Second row: Small collapse times. Plots adapted from Ref. [Koe1].

5.2 M_{thr} by Means of Interpolation of t_{coll} Data

Based on the steep behaviour of the collapse-time curve at threshold (cf. Fig. 4.4a), and on the analysis of more than 300 simulations (cf. Fig. 4.4b), we have defined a *threshold collapse-time* τ_{thr} , related to the threshold mass by condition (4.10). Based on this condition, different methods can be developed to determine M_{thr} by means of interpolation. One possibility is the method introduced in Ref. [Koe1]. As discussed in Sect. 4.4.2, there are three essential differences to the method by Köppel et al., 2019: The first difference concerns the time scales related to M_{thr} , i.e., τ_{thr} and τ_{TOV} , respectively. Secondly, Köppel et al., 2019, determine the threshold mass by means of extrapolation as opposed to interpolation in the case of the method of Ref. [Koe1]. A third difference is highlighted in Fig. 4.5. It concerns the considered mass intervals. We point out that a method build upon the concept of determining M_{thr} by means of interpolation (related to τ_{thr}), may be completed with different kinds of fits of collapse time data. In any case, a method to determine M_{thr} based on the collapse time curve always comes as a package containing a fit function/ fitting procedure, a time scale (e.g. τ_{thr} or τ_{ff}), and a selection of data (e.g. data with $M \approx M_{\text{thr}}$).

5.2.1 Mass Interval

Compared to approaches usually taken in the literature, the method introduced in Ref. [Koe1] includes an unusual selection of data points. Typically, methods to determine M_{thr} involve a search for a set of BNS configurations which includes both prompt-collapse and delayed-collapse mergers with $M \approx M_{\text{thr}}$. While we adopt the goal to include both prompt-collapse and delayed-collapse mergers, we do not seek to narrow down the interval containing M_{thr} . In the case of the bracketing method for example new configurations are chosen based on previous results, and the search is continued until the desired accuracy is reached, i.e., once the interval containing M_{thr} has sufficiently been reduced in size. By means of bisection the interval may be cut in half with each additional simulation.

For our method, a broader interval of total masses is considered. As discussed in chapter 3, the investigated parameter space includes data points with a typical separation of $\Delta M = 0.1 M_{\odot}$, where additional data may be placed at half-steps with $\Delta M = 0.05 M_{\odot}$.² Tab. 3.6 provides an overview of the studied parameter space. The investigated mass intervals have a typical width of $0.4 M_{\odot}$. They are intended to include both prompt-collapse and delayed-collapse mergers over the whole spectrum of mass ratios. Since the EOS strongly affects the outcome of the merger, we consider different intervals of total masses for each EOS. In some cases the investigated mass interval does not contain type II or type III mergers. Furthermore, we point out that by setting the minimal mass step to $0.05 M_{\odot}$, the behaviour of the collapse-time curve close to threshold remains unresolved within our data set, cf. Figs. 4.5a and 5.2.

5.2.2 Fit Function

To determine M_{thr} by means of interpolation, we introduced an empirically motivated three-parameter fit formula in Ref. [Koe1]:

$$t_{\text{coll}}(M) = (\tau_{\text{thr}} - c) \cdot \exp \left[-a \frac{M - b}{M - M_s} \right] + c, \quad (5.1)$$

which is constructed such that $t_{\text{coll}}(M = b) = \tau_{\text{thr}}$, i.e.,

$$b = M_{\text{thr}}. \quad (5.2)$$

²In the study including the largest number of EOSs up to now, Bauswein et al., 2021, M_{thr} is determined using the bracketing method with a minimal accuracy of $\pm 0.025 M_{\odot}$. This accuracy corresponds to an interval $(M_{\text{upper}}^{\text{delayed}}, M_{\text{lower}}^{\text{prompt}})$ of length $0.05 M_{\odot}$.

Eq. (5.2) may seem insignificant at a first glance, however, this relation implies two advantages compared to more generic fit formulae:

1. We do not need to invert Eq. (5.1) to determine M_{thr} and its error. In fact, we identify ΔM_{thr} with the error estimate for the parameter b , i.e., $\Delta M_{\text{thr}} = \Delta b$.
2. As the threshold mass is de facto a parameter of Eq. (5.1), bounds can easily be applied to M_{thr} , i.e., we may limit b to meet the bracketing condition (4.6).

To apply bounds on b in terms of the bracketing method, a distinction between prompt and delayed collapse may simply be based on t_{coll} , i.e., $b_{\text{min}} = M_{\text{upper}}^{\tau_{\text{coll}} < \tau_{\text{thr}}}$ and $b_{\text{max}} = M_{\text{lower}}^{\tau_{\text{coll}} > \tau_{\text{thr}}}$. However, taking uncertainties into account, as determined by simulations with different numerical resolutions, we will not implement the suggested bounds strictly. In its asymptotic behaviour, function (5.1) is consistent with the following assumptions and observations about the collapse time curve:

1. The collapse time increases strongly as the total mass of a BNS approaches the maximum mass of rigid rotation $M_{\text{max}}^{\text{rot}}$.³ We assume this mass to mark the threshold to stable remnant NS configurations, i.e., $t_{\text{coll}} \rightarrow \infty$, for $M \rightarrow M_{\text{max}}^{\text{rot}}$.
2. The collapse time decreases monotonously for increasing M .
3. Concerning the selection of data underlying the fits shown in Fig. 5.2, we assume the second derivative of $t_{\text{coll}}(M)$ not to change its sign, ignoring the unresolved change of slope in vicinity of M_{thr} .
4. The collapse time does not become arbitrarily small. Beyond the allowed range of total masses⁴, we expect $t_{\text{coll}}(M)$ to asymptotically approach a minimal value.

The asymptotic behaviour at high M is assured by the primary building block the of fit function, which is an exponential function with negative exponent. Therefore, function (5.1) provides a lower bound $c > 0$:

$$t_{\text{coll}}(M) \rightarrow c, \quad M \rightarrow \infty. \quad (5.3)$$

The EOS-dependent asymptotic behaviour for $M \rightarrow M_{\text{max}}^{\text{rot}}$ is implemented in the exponent's denominator which has a pole at $M = M_s$:

$$t_{\text{coll}}(M) \rightarrow \infty, \quad M \rightarrow M_s = M_{\text{max}}^{\text{rot}}(\text{EOS}). \quad (5.4)$$

³The maximum masses $M_{\text{max}}^{\text{rot}}$ of rigid rotation of SLY, ALF2 and H4 are $2.507342 M_{\odot}$, $2.510254 M_{\odot}$, and $2.476984 M_{\odot}$, respectively; cf. Dietrich et al., 2018.

⁴The allowed range of M depends on q and the EOS. It is limited by the condition $M_1 < M_{\text{max}}$, i.e., the primary component cannot exceed the maximum mass of an irrotational NS of given EOS.

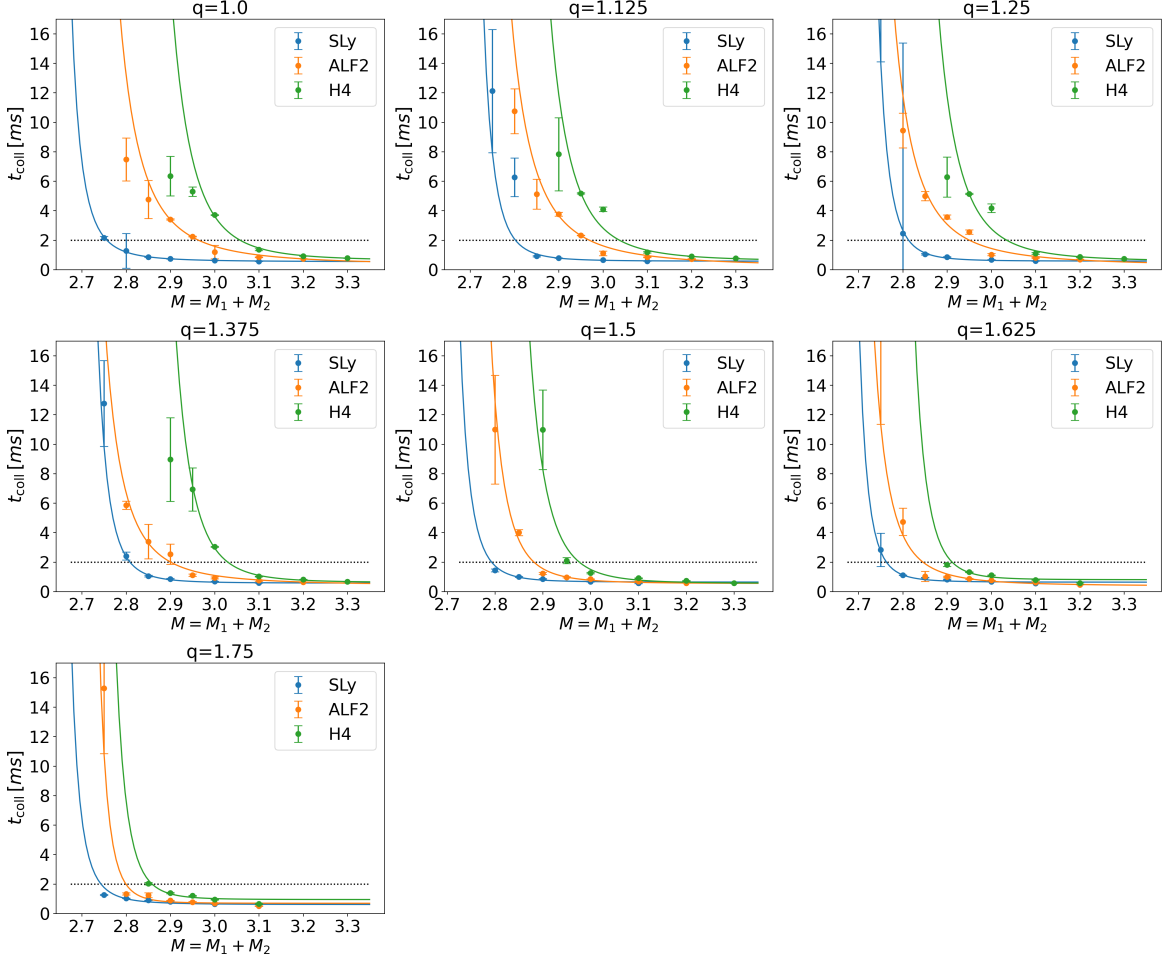


Figure 5.2: Collapse time t_{coll} as a function of the total mass M for given mass-ratios. For each EOS, the data are fitted based on Eq. (5.1). SLy, ALF2, and H4 are presented in blue, orange, and green respectively. The collapse time increases strongly for decreasing M and levels off for increasing M . The horizontal line at $t_{\text{coll}} = \tau_{\text{thr}} = 2$ ms marks the threshold to prompt collapse. The total mass corresponding to this intersection, M_{thr} , increases with higher tidal deformability. Plots adapted from Ref. [Koe1].

5.2.3 Fitting Procedure and Results

For each EOS and each mass ratio, we determine M_{thr} by means of a least-squares approach, applying the fit formula (5.1) discussed in Sect. 5.2.2, while considering all simulations for which the remnant collapsed to a BH within simulation time. In unclear cases where a collapse took place for one numerical resolution, while this was not the case for the second resolution, we trust the result obtained for the higher resolution. In practice, applying the fit to the data presents a few obstacles that need to be overcome. In cases where no delayed-collapse data ($t_{\text{coll}} > \tau_{\text{thr}}$) is available, the

parameters a and b would become weakly determined if no measures are taken, cf. for example SLy with $q = 1.5$ or $q = 1.75$, or H4 with $q = 1.625$. The same problem occurs due to large error bars in delayed-collapse cases, cf. for example SLy with $q = 1.125$ or $q = 1.25$. In comparison to the precisely determined prompt-collapse data, these data points become virtually invisible to the least-squares algorithm. To solve this problem, we include a penalty term into the fitting procedure, demanding the fit function to reach a minimum value at low masses. In case of large error bars, this minimum value is identified with the lower end of the of the leftmost error bar. In case of absent delayed-collapse data, we rely on type-IV data, demanding the fit function to reach a minimum value (equal to the highest collapse-time found over all simulations) at the respective total mass related to type-IV data. In cases where neither delayed-collapse data nor type-IV data are available, we assume the type-IV regime to be valid over all mass ratios, inferring its location from adjacent data of the same EOS, e.g. $M = 2.7 M_{\odot}$ in the case of SLY and ALF2, or $M = 2.8 M_{\odot}$ in the case of H4, cf. Tab. 3.6. In the described problematic cases, this procedure balances the overweight of type-I data. In cases where delayed-collapse data are present, this procedure has no noticeable effect.

As mentioned in connection with Eq. (5.2), bounds may be set on the parameter b to limit the allowed M_{thr} -range according to condition (4.6). In doing so, we assure our threshold-mass results to have a maximum error of $\Delta M_{\text{thr}} = 0.05 M_{\odot}$ or $0.1 M_{\odot}$, depending on the respective local resolutions of the total-mass interval. In cases, characterized by $|t_{\text{coll}} - \tau_{\text{thr}}| < \epsilon$, where the merger type is either I or II depending on the resolution (Tab. 3.6), these bounds are weakened, cf. for example H4 with $q = 1.5$ (Fig. 5.2). All 21 fits performed on the data set of Ref. [Koe1] are presented in Fig. 5.2. The $\tau_{\text{thr}} = 2$ ms-line in each panel marks the threshold to prompt collapse. M_{thr} is located at the intersections between the fits and the 2 ms-line.

Results obtained for the threshold mass are given in Tab. 5.1. Besides M_{thr} , three related quantities are shown: The threshold mass coefficient k_{thr} , and two quantities characterising the tidal deformability of the BNS: κ_2^{T} and $\tilde{\Lambda}$, cf. Sect. 3.1.3. The indicated accuracies of k_{thr} , κ_2^{T} and $\tilde{\Lambda}$ are calculated based on the uncertainty ΔM_{thr} determined for the parameter b . While it is consequent to use the error Δb as an estimate of M_{thr} , discussing our method with respect to our fine-resolved example data set (ALF2, $q = 1/5$), we may come to the conclusion that this error estimate is too optimistic, cf. Sect. 5.2.4. In chapter 6 we compare our data to results of other studies. Furthermore, we will discuss and refine models for threshold quantities.

Table 5.1: Quantities at the threshold to prompt collapse for all 21 cases (EOS, q). Presented in columns 3-10 are the threshold mass M_{thr} , the threshold mass coefficient k_{thr} , the tidal polarizability parameter κ_2^{T} and the tidal polarizability coefficient $\tilde{\Lambda}$ at threshold, and their respective errors. Table taken from Ref. [Koe1].

EOS	q	M_{thr} [M_{\odot}]	ΔM_{thr} [M_{\odot}]	k_{thr}	Δk_{thr}	κ_2^{T}	$\Delta \kappa_2^{\text{T}}$	$\tilde{\Lambda}$	$\Delta \tilde{\Lambda}$
SLy	1.000	2.756	0.003	1.338	0.001	31.9	0.9	341	18
SLy	1.125	2.802	0.006	1.360	0.003	29.1	1.9	310	36
SLy	1.250	2.813	0.011	1.365	0.005	29.6	3.4	314	64
SLy	1.375	2.808	0.003	1.363	0.002	31.6	1.2	334	23
SLy	1.500	2.793	0.003	1.356	0.002	34.9	1.3	367	25
SLy	1.625	2.763	0.017	1.341	0.008	39.8	7.8	416	145
SLy	1.750	2.743	0.001	1.332	0.001	44.2	0.6	461	11
ALF2	1.000	2.963	0.002	1.489	0.001	38.9	0.6	415	11
ALF2	1.125	2.969	0.001	1.492	0.001	38.7	0.4	412	8
ALF2	1.250	2.950	0.004	1.482	0.002	41.3	1.6	439	31
ALF2	1.375	2.900	0.008	1.457	0.004	47.2	3.7	499	72
ALF2	1.500	2.881	0.002	1.448	0.001	50.3	1.2	530	22
ALF2	1.625	2.845	0.006	1.430	0.003	56.1	3.6	589	67
ALF2	1.750	2.799	0.002	1.407	0.001	63.5	1.0	664	20
H4	1.000	3.057	0.001	1.507	0.000	46.6	0.4	498	8
H4	1.125	3.037	0.003	1.497	0.001	49.6	1.4	528	26
H4	1.250	3.034	0.004	1.496	0.002	51.5	1.9	546	37
H4	1.375	3.029	0.001	1.494	0.001	54.3	0.6	574	11
H4	1.500	2.976	0.003	1.467	0.001	64.0	2.0	673	35
H4	1.625	2.911	0.002	1.435	0.001	77.4	1.7	810	32
H4	1.750	2.858	0.002	1.409	0.001	91.4	1.8	954	34

5.2.4 Proof of Principle and Conclusion

Investigating to what extent the threshold mass determined by our method is consistent with results obtained by application of the bracketing method, we once more make use of our finely resolved example of ALF2 with $q = 1.5$. Considering the data set of Ref. [Koe1] from the viewpoint of the bracketing method, in most cases we locate M_{thr} within intervals of length $0.05 M_{\odot}$. In the extended data set of the (ALF2, $q = 1.5$) example case on the other hand, we narrow down the interval containing M_{thr} much further, cf. Tab. 4.1). This comparison of methods is presented in Fig. 5.3. The first panel shows the application of our method to seven data points. As discussed before, the fit does not model the change of slope at $M \approx M_{\text{thr}}$ that is underresolved in the data set depicted in the first panel.

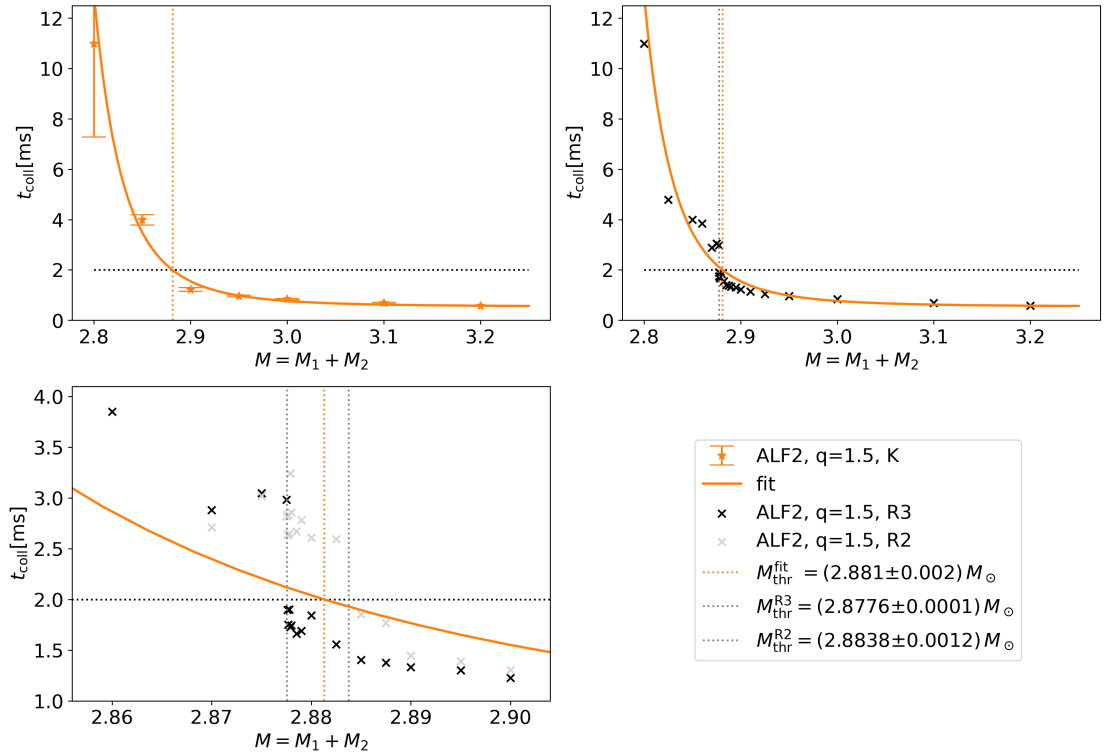


Figure 5.3: Collapse time in the case of ALF2 with $q = 1.5$. Upper left: Fit of seven data points as presented in Fig. 5.2. The orange vertical dotted line marks the threshold mass as determined by interpolation. The gray vertical dotted lines in the second and third panel mark threshold masses determined by application of the bracketing method for resolutions R3 and R2. Upper right: displayed are the same data and fit as in the first panel together with results of additional R3 simulations of total masses close to the threshold mass (black crosses). Lower left: Close-up of the second panel; additionally R2 data (gray crosses) are presented together with the respective threshold mass determined by application of the bracketing method. Figure adapted from Ref. [Koe1].

In the second and third panel of Fig. 5.3 the additional data (crosses) and their evaluation with respect to the bracketing method (gray vertical lines) are included in comparison to the curve fitted to the seven data points of the first panel. In the lower left panel, data of resolutions R3 and R2 are distinguished being coloured black and gray, respectively. A comparison of data of these two resolutions shows that the transition from delayed to prompt collapse is shifted to higher M going from R3 to R2. Furthermore, the R3 data appear to be more systematic. Applying the bracketing method to data of either resolution, we obtain two threshold-mass values: $M_{\text{thr}}^{\text{R3}} = 2.8776 \pm 0.0001$ and $M_{\text{thr}}^{\text{R2}} = 2.8838 \pm 0.0012$, cf. Fig. 5.3. Assuming the value determined by the bracketing method applied to the R3 data to be the correct value of M_{thr} , we find the difference to the value found by means of the depicted fit to be

smaller than $0.005 M_{\odot}$. This is a small deviation. Yet, it is higher than the error indicated in Tab. 5.1. While the threshold mass determined by interpolation is not contained within the uncertainty interval of the threshold mass obtained by bracketing for the R3 resolution, $M_{\text{thr}}^{\text{R3}}$, it lies well within the interval spanned by the threshold masses of different resolutions, cf. lower left panel of Fig. 5.3. Bearing in mind that uncertainty estimates used within the fitting procedure take both of these resolutions into account, this appears to be a valid result. Although the investigation of one case does not constitute a proof, it is at least a proof of principle.

We come to the conclusion that in this case the threshold mass determined by means of interpolation is, to some degree, consistent with the bracketing method. Yet, we can not exclude inconsistencies in other cases. In practice, we have to assume the bracketing method to be the more stable and reliable method. Applying the bracketing method, the interval containing M_{thr} can in theory be narrowed down until the desired accuracy is reached. However, this statement has to be taken with a pinch of salt. In practice, increasing the accuracy means to conduct more simulations while choosing the next configuration's total masses based on the preceding simulations. Computationally and in terms of time, this can become a costly endeavour. Furthermore, going to high accuracy, deviations between resolutions become notable. This raises the question of how to deal with results of different numerical resolutions in the context of the bracketing method. These two points motivate the search for methods that determine M_{thr} based on interpolation and a finite number of simulations. Our method is not the perfect solution to this problem, but it seems to be a reasonable compromise to achieve two goals based on the same set of data: determining a value of M_{thr} , and studying properties of BNS mergers over a comparatively large interval, cf. Chap. 6.

5.3 Discussion of Collapse-Time Methods

After the discussion of our method to determine M_{thr} based on interpolation of collapse-time data, we conclude this chapter by discussing the method by Köppel et al., 2019 (free-fall method), and two different attempts to determine M_{thr} by means of interpolation. On the one hand, we will use the same fit that Köppel et al., 2019, use to extrapolate onto the free-fall time τ_{TOV} . On the other hand, we will consider an alternative fit to data $t_{\text{coll}}(M)$ with $M \approx M_{\text{thr}}$. Again, we will make use of the (ALF2, $q = 1.5$) data set as a test bed.

5.3.1 Method by Köppel et al.

In Sect. 4.4.2, in comparison to our method, we have introduced the free-fall method by Köppel et al., 2019, which has also been applied in a follow-up study by Tootle et al., 2021. Using the usual data set as a test bed, i.e., ALF2 with $q = 1.5$, we try to reproduce the free-fall method. Guided by the respective figures in their works that illustrate their method, we plot M/M_{\max} against $t_{\text{coll}}/\tau_{\text{TOV}}$, and use Eq. (4.12) to fit different sets of four data points in each panel of Fig. 5.4. Each selection of data points contains two delayed-collapse mergers and two prompt-collapse mergers with $M \approx M_{\text{thr}}$.⁵ Considering the shape of M/M_{\max} as a function of $t_{\text{coll}}/\tau_{\text{TOV}}$, it seems plausible that this is what Köppel et al., 2019, and Tootle et al., 2021, have done.⁶

Going from 5.4a to 5.4d, we use different subsets of the example data set with increasing the mass step ΔM from panel to panel. The step sizes are $\Delta M = 0.0025$ in (A), $\Delta M = 0.005$ in (B), $\Delta M = 0.01$ in (C) and $\Delta M = 0.025$ in (D). While panels (A) through (C) show cases with data related to the steep regime of $t_{\text{coll}}(M)$, panel 5.4d obviously shows an example of inadequate data. Considering the first three panels, we find that in each case the threshold mass determined by extrapolation to $t_{\text{coll}}/\tau_{\text{TOV}} = 1$ has a value higher than the highest total mass M_{\max}^{data} contained in the respective data set, i.e.,

$$M_{\text{thr}}^{\text{ff}} > M_{\max}^{\text{data}}, \quad (5.5)$$

cf. data presented in the upper right of each panel. We have already advertised a similar relation in Eq. (4.9), stating that the results by Köppel et al., 2019, show only small differences from results by Bauswein et al., 2021. Considering that we interpreted M_{\max}^{data} to be related to a delayed-collapse merger, Eq. (5.5) implies that the threshold mass, $M_{\text{thr}}^{\text{ff}}$, determined by the free-fall method is not consistent with the threshold-mass definition by Bauswein et al., 2013, if we look at inequality (4.6).

⁵As indicated by Fig. 2 of the respective reference, Köppel et al., 2019, sometimes used less than 4 data points. Furthermore, it is not clearly stated by Köppel et al., 2019, how the data for their fits are selected. Here we rely on Fig. 4 of Tootle et al., 2021, which shows three examples of minimum-lapse data. Interpreting these curves with respect to the criteria discussed in Sect. 4.3.2, we find at least two prompt-collapse mergers and one delayed-collapse merger in each of the three panels.

⁶There is one characteristic which we cannot reproduce: The data portrayed in the works by Köppel et al., 2019, and Tootle et al., 2021, exclusively contain collapse times with $t_{\text{coll}} \lesssim 12\tau_{\text{TOV}}$ ($\lesssim 6\tau_{\text{TOV}}$ in the case of Köppel et al., 2019). This range is notably different from the $t_{\text{coll}}/\tau_{\text{TOV}}$ -range of our data, cf. Fig. 5.4. We will shortly analyse this issue, arguing that the axis scale in Fig. 5.4 is not an error. Considering Tab. 1 of Köppel et al., 2019, we find that the free-fall times of the applied EOSs are smaller than $100\mu\text{s}$. With this estimate, a normalised collapse time $t_{\text{coll}}/\tau_{\text{TOV}} \leq 10$ corresponds to a collapse time $t_{\text{coll}} \leq 1$ ms. This estimate stands in conflict with the threshold collapse-time (4.11) and the data depicted in panels 1-3 of Fig. 4 of Tootle et al., 2021. In the following analysis, we will ignore this issue as it does not seem to be of consequence to the qualitative discussion of this method.

Even though the error is small in each of the cases (A)-(C), we have to point out that data which can be adequately used for the free-fall method, i.e., data with $M \approx M_{\text{thr}}$, can alternatively be used to determine M_{thr} applying the bracketing method, obtaining a threshold mass with small uncertainty which is consistent with definition (4.6).

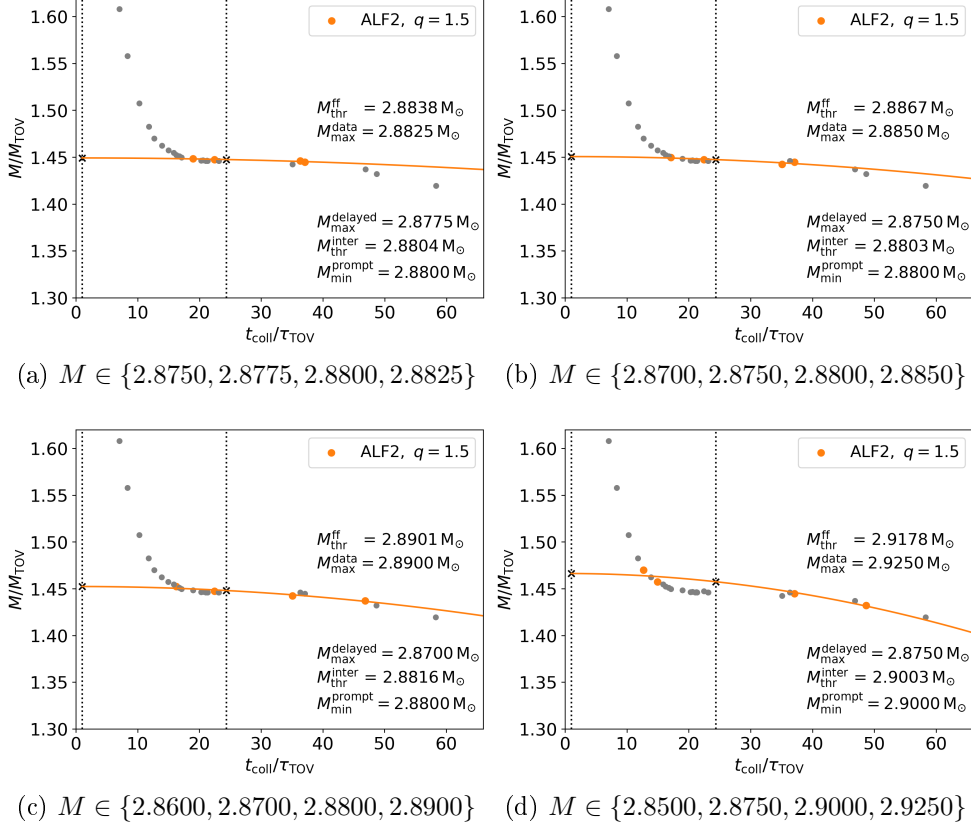


Figure 5.4: Examination of the free-fall method. For each plot, a different subset (orange) of the example data-set (Tab. 4.1) has been used for the fit (Eq. (4.12)). Points that are not considered for the fit are marked with gray color. In each case, four data points are used: two prompt-collapse and two delayed-collapse mergers. Crosses mark where the threshold mass is localized by means of extrapolation ($M_{\text{thr}}^{\text{ff}}$, free-fall method, $t_{\text{coll}}/\tau_{\text{TOV}} = 1$), or interpolation ($M_{\text{thr}}^{\text{inter}}$, $t_{\text{coll}} = \tau_{\text{thr}}$). The extrapolation results are compared to the highest total mass $M_{\text{max}}^{\text{data}}$ considered for the fit. The interpolation results are compared to the bracketing masses $M_{\text{max}}^{\text{delayed}}$ and $M_{\text{min}}^{\text{prompt}}$.

5.3.2 Modification of Köppel's Method

Having discovered that the free-fall method produces results that are inconsistent with the employed data, we will try to use the same fit to determine a threshold mass

$M_{\text{thr}}^{\text{inter}}$ consistent with inequality (4.6) by means of interpolation. This attempt is also demonstrated in Fig. 5.4. In the lower right of each panel we compare $M_{\text{thr}}^{\text{inter}}$ to the bracketing masses $M_{\text{max}}^{\text{delayed}}$ and $M_{\text{min}}^{\text{prompt}}$. However, in none of the presented cases, we find $M_{\text{thr}}^{\text{inter}}$ to be contained in the bracketing interval $[M_{\text{max}}^{\text{delayed}}, M_{\text{min}}^{\text{prompt}}]$. We explain this with the way the graph of the fit function is curved compared to the local curvature indicated by the data points. While the collapse-time curve has an inflection point localized at τ_{thr} or close by, the graph of the fit function (4.12) does not.

5.3.3 Alternative Fitting Procedure

We conclude our discussion of collapse time fits designed to determine M_{thr} with thoughts about alternative fitting methods. As pointed out earlier, the bracketing method is a computationally expensive method when it comes to achieving low uncertainties. Furthermore, it does not provide a straightforward way to account for differences in results of different resolutions. These points aside, it is the natural way to determine M_{thr} and probably the most reliable one. However, it appears to be desirable to find an economic compromise, i.e., a method which allows to abort the process of conducting simulations and choosing new parameters earlier while determining M_{thr} with high accuracy. The fitting procedure of Köppel et al., 2019, appeared to be promising in that regard. However, we have discussed reservations about this method and its modification in Sects. 5.3.1 and 5.3.2. To formulate a goal, we are looking for a fit to collapse-time data that respects the local shape of $t_{\text{coll}}(M)$ in the vicinity of the threshold to prompt collapse that is based on a small number of data points which include both prompt-collapse and delayed-collapse mergers. The method would be required to take into account data of different numerical resolutions and determine M_{thr} with higher accuracy compared to the bracketing method applied to the same set of data. While we cannot present a fit function that achieves all of these goals, we are going to at least consider an attempt that illustrates what we are looking for. The function

$$t_{\text{coll}}(M) = -A \cdot \tanh[a(M - b)] + \tau_{\text{thr}} \quad (5.6)$$

$$A = \begin{cases} c & , M < b \\ d & , M > b \end{cases} ,$$

steeply decreases at $M \approx b$ and cuts the $t_{\text{coll}} = \tau_{\text{thr}}$ line at $M = b$. It is constructed similarly to Eq. (5.1), allowing us to put constraints on the parameter b in accordance

with the condition in Eq. (4.6). We test this fit function, employing sets of four data points with varying bracketing interval, cf. Fig. 5.5. As indicated in each panel, the accuracy of these fits does not surpass the one of the bracketing method applied to the respective data sets, i.e., the uncertainty interval is larger than the limits enforced on the parameter b . While this disqualifies the presented attempt, it does not exclude the possibility that a more clever ansatz proves to be an effective tool in determining M_{thr} with high accuracy in a computationally less expensive way compared to the bracketing method.

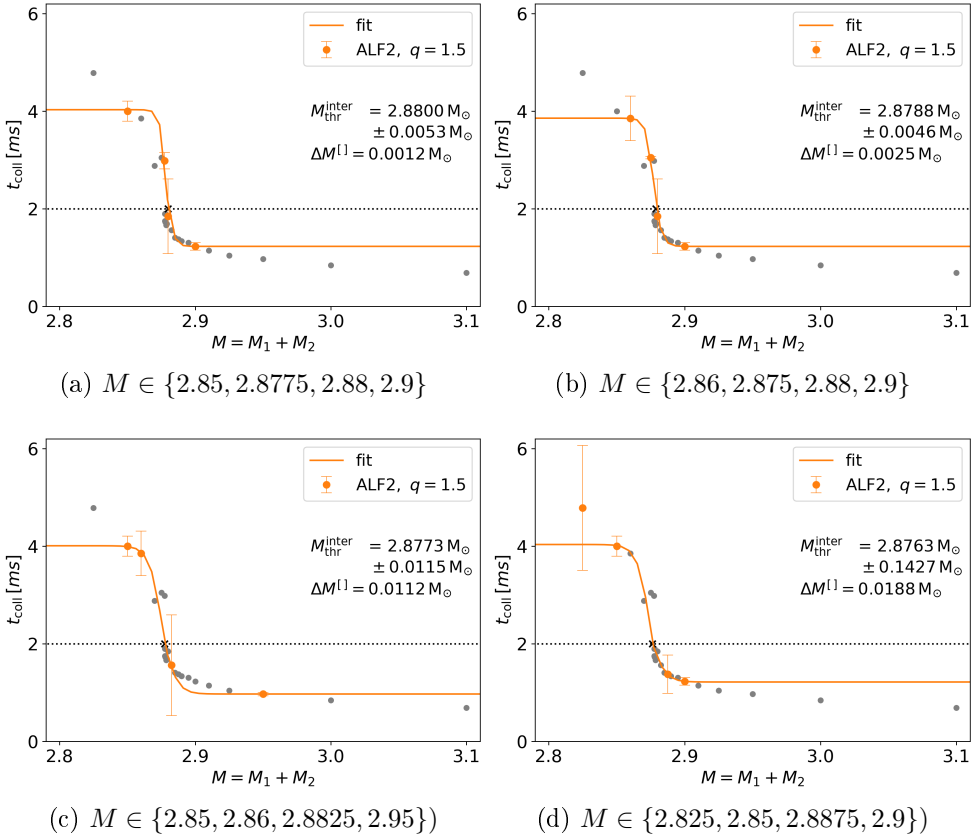


Figure 5.5: Examination of an alternative fit of collapse-time data with $|M - M_{\text{thr}}| < 0.1$. For each plot, a different subset (orange) of the example data-set (Tab. 4.1) has been used for the fit (Eq. (5.6)). Points that are not considered for the fit are marked with gray color. In each case, the sample contains prompt-collapse and delayed-collapse mergers. The data and sample size are varied. Crosses mark where the threshold mass is localized by means of interpolation ($M_{\text{thr}}^{\text{inter}}, t_{\text{coll}} = \tau_{\text{thr}}$). The error, identified with the error estimate of the employed least-squares routine for the parameter b , is compared to the error of bracketing method in the respective case.

Chapter 6

Modelling Properties of Threshold Configurations

In this chapter, we will investigate the effect of mass ratio on the threshold to prompt collapse taking into account recent studies on M_{thr} . We will consider the threshold mass and threshold values of the tidal parameters $(\kappa_2^T)_{\text{thr}}$ and $\tilde{\Lambda}_{\text{thr}}$, discussing existing models and developing new models that in particular take into account the effect of mass ratio on quantities at threshold. As we review findings of the simulation campaign of Ref. [Koe1], we will, in places, enrich the discussion with additional material. We will compare these findings to available data and fits of other studies. Furthermore, we will present fits of combined data sets that base models on a larger number of EOSs.

Distinguishing the cases of prompt and delayed collapse, we will discuss the effect of mass ratio on merger dynamics, and how these influence properties of the remnant systems. The quantities considered in this context are the disk mass, and the remnant BH's mass and spin. In the case of BH mass and disk mass we will approximate lower and upper limits for the case of prompt collapse, respectively.

6.1 Threshold Mass - The Effect of Mass Ratio

While early studies of the threshold mass to prompt collapse focussed on equal-mass binaries of irrotational stars, asymmetric binaries have gained more attention in recent studies. In a small but growing number of systematic studies, factors aside from the EOS are considered, i.e., the effect of mass ratio and, in one case, the effect of spin.

6.1.1 Recent Studies

To give a short overview over these studies, we list a selection of recent studies with minimal summaries, indicating their individual foci by reporting important models introduced or developed in these works.

- Bauswein et al., 2021, consider 40 EOS and three mass ratios, $\tilde{q} \in \{1.0, 0.85, 0.7\}$. With respect to the number of investigated EOSs it is the largest study so far. In their work, Bauswein et al. consider fit formulae of the type

$$M_{\text{thr}} = \alpha (1 - \tilde{q})^n + \gamma \quad (6.1)$$

finding $n = 3$ to be a good compromise with respect to all of their data. In this context they distinguish between different samples of EOSs, including hadronic EOSs, hybrid models and excluded EOSs. Developing their model further, they suggest fit formulae with two stellar parameters (X, Y) of the type

$$M_{\text{thr}}(\tilde{q}, X, Y) = c_1 X + c_2 Y + c_3 + c_4 \delta\tilde{q}^3 X + c_5 \delta\tilde{q}^3 Y, \quad (6.2)$$

with $\delta\tilde{q} = 1 - \tilde{q}$ and $\tilde{q} = 1/q \leq 1$. For different pairs of parameters (X, Y) , i.e., $X = M_{\text{max}}$ and $Y \in \{R_{1.6}, R_{\text{max}}, \Lambda_{1.4}, \Lambda_{\text{thr}}\}$, Bauswein et al. present fits based on different samples of EOSs.

- The work by Tootle et al., 2021, addresses both the effect of mass ratio and the effect of spin χ . They consider three EOS. The investigated mass-ratio interval reaches up to the extreme case of $\tilde{q} = 0.5$. It contains four mass ratios in total, i.e., $\tilde{q} \in \{1.0, 0.9, 0.7, 0.5\}$. Tootle et al. follow the ansatz

$$M_{\text{thr}}(\text{EOS}, \tilde{q}, \chi) = \kappa(\text{EOS}) f(\tilde{q}, \chi), \quad (6.3)$$

assuming the effect of mass ratio and spin to be independent of the EOS. The ansatz for $f(\tilde{q}, \chi)$ is a second order polynomial of type

$$f(\tilde{q}, \chi) = a_1 + a_2 (1 - \tilde{q}) + a_3 \chi + a_4 (1 - \tilde{q})\chi + a_5 (1 - \tilde{q})^2 + a_6 \chi^2, \quad (6.4)$$

where a_1 is set to 1 and additional assumptions are made for a_6 , leaving four coefficients to be determined based on simulation data.

- Perego et al., 2021, explored a parameter space spanned by six EOSs and six mass ratios, $\tilde{q} \in \{1.0, 0.85, 0.75, 0.7, 0.65, 0.6\}$, suggesting piecewise linear fits to model the fraction

$$f(\tilde{q}) = \frac{M_{\text{thr}}(\tilde{q})}{M_{\text{thr}}(\tilde{q} = 1)} = \alpha(\tilde{q})\tilde{q} + \beta(\tilde{q}) = \begin{cases} \alpha_l \tilde{q} + \beta_l, & \tilde{q} < \hat{q} \\ \alpha_h \tilde{q} + \beta_h, & \tilde{q} > \hat{q} \end{cases}, \quad (6.5)$$

where \hat{q} is assumed to be 0.725, and the incompressibility K_{max} is used as an EOS-dependent parameter.

- The simulation campaign presented in Ref. [Koe1] and in this thesis covers three EOSs and seven mass ratios, $q \in \{1.0, 1.125, 1.25, 1.375, 1.5, 1.625, 1.75\}$. To model the effect of mass ratio over a broader mass-ratio interval than the one considered by Bauswein et al., 2021, we extended the fit function of Bauswein et al., adding two linear terms to their fit formula:

$$M_{\text{thr}}(q, X, Y) = c_1 X + c_2 Y + c_3 + c_4 \delta\tilde{q} X + c_5 \delta\tilde{q} Y + c_6 \delta\tilde{q}^3 X + c_7 \delta\tilde{q}^3 Y. \quad (6.6)$$

While the original fit function has its maximum or minimum at $\tilde{q} = 1$, the extra terms in the extended version allow for extrema at $q > 1$ (i.e., $\tilde{q} < 1$).

Reviewing Ref. [Koe1], we will discuss the mass-ratio dependence of M_{thr} in this section, comparing our findings to results of those studies, which cover a larger fraction of the EOS parameter space. We will examine and develop fits modelling the mass ratio and EOS dependence of M_{thr} .

6.1.2 Effect of Mass Ratio and Fits

To examine the effect of mass ratio on M_{thr} , we compare two of the models mentioned at the beginning of this section, i.e. Eq. (6.2) and Eq. (6.6). Fig. 6.1 shows the application of the two fit formulae to our data: In the first column, Eq. (6.2) (Bauswein et al., 2021) is applied, in the second column it is the extended version, Eq. (6.6) ([Koe1]). In both of these cases, we follow Bauswein et al., 2021 in the choice of stellar-parameter pairs, i.e., $X = M_{\text{max}}$ and $Y \in \{R_{1.6}, R_{\text{max}}, \Lambda_{1.4}\}$. The coefficients and measures of confidence of the fits depicted in the first column of Fig. 6.1 are given in Tab. 6.3 (sample K). The respective quantities of the fits depicted in the second column are given in columns 2-4 of Tab. 6.1.

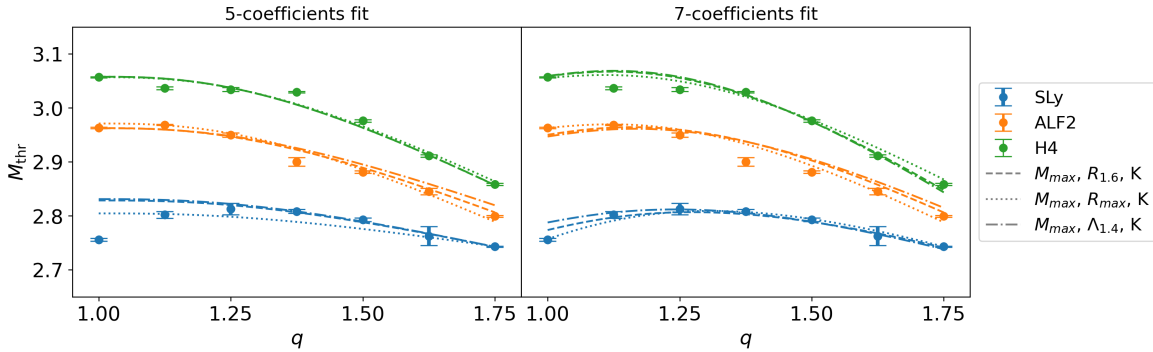


Figure 6.1: Data points: threshold mass M_{thr} , as determined here and in Ref. [Koe1], plotted as a function of the mass ratio q . At the upper end of the mass ratio interval, M_{thr} decreases for increasing q . In the case of SLy, the data clearly exhibit a maximum at $q \approx 1.375$.

First column: Dashed/dotted lines: Fits to the data points, for different stellar parameters, as given in the legend, based on the fit formula proposed by Bauswein et al., 2021 (reproduced in Eq. (6.2)). The respective coefficients are given in Tab. 6.3.

Second column: Dashed/dotted lines: Fits to the data points depending on pairs of stellar parameters as given in the legend, based on Eq. (6.6) with coefficients given in Tab. 6.1. Figure adapted from Ref. [Koe1].

The five-coefficients fit by Bauswein et al. distinguishes two cases: monotonously decreasing and monotonously increasing $M_{\text{thr}}(q)$. In most cases, Bauswein et al., 2021, find $M_{\text{thr}}(q)$ to decrease with increasing $q > 1$. In the case of soft EOSs they observe only a weak mass-ratio effect and sometimes increasing $M_{\text{thr}}(q)$. Considering our softest EOS (SLy), our data appears to stand in contrast to this categorization, since our SLy data decreases for high q . However, Bauswein et al., 2021, considered a smaller range of mass ratios, i.e., $q < 1/0.7 \approx 1.4$. For high mass ratios ($q \gtrsim 1.4$) we always find $M_{\text{thr}}(q)$ to be a decreasing function in q . This observation is backed up by results of Perego et al., 2021, for six more EOSs. In the broader picture, the cases of EOSs for which Bauswein et al., 2021, find $M_{\text{thr}}(q)$ to increase (for small to medium mass ratios) may, in general, be cases for which $M_{\text{thr}}(q)$ has a maximum at intermediate values of q . The seven-coefficients fit (Eq. (6.6)) provides for the possibility of such a maximum at $q > 1$. However, as we will see in Sect. 6.1.3, due to the small number of studied EOS, the fits given in Tab. 6.1 are of limited predictive power regarding the threshold-mass curve of other EOSs. Therefore, we will discuss the extension of these fits to combined data sets in Sect. 6.1.4.

A feature which we do not model, is the small dip of $M_{\text{thr}}(q)$ at small mass-ratios that we find in the case of H4, cf. Fig. 6.1. This is also depicted in Fig. 4 of Bauswein et al., 2021, for the example of DD2F.

Table 6.1: Coefficients c_1 to c_7 fitting M_{thr} data (21 data points as reported in Tab. 5.1) for three pairs of stellar parameters (X, Y) by means of a least-squares approach. In column four, the threshold mass of the $q = 1$ case is used as a parameter. The following measures of variation are given: the maximal absolute residual (max.), the mean absolute residual (av.), and the coefficient of determination, (R^2). Table adapted from Ref. [Koe1].

$M_{\text{thr}}(q, X, Y) = c_1 X + c_2 Y + c_3 + c_4 \delta\tilde{q} X + c_5 \delta\tilde{q} Y + c_6 \delta\tilde{q}^3 X + c_7 \delta\tilde{q}^3 Y, \delta\tilde{q} = 1 - \tilde{q}$				
(X, Y)	$(M_{\text{max}}, R_{1.6})$	$(M_{\text{max}}, R_{\text{max}})$	$(M_{\text{max}}, \Lambda_{1.4})$	$(M_{\text{max}}, M_{\text{thr}}(q = 1))$
c_1	-0.645 ± 0.02	0.831 ± 0.021	-0.48 ± 0.019	$(5.724 \pm 2.156) \cdot 10^{-2}$
c_2	0.127 ± 0.001	0.19 ± 0.001	$(4.425 \pm 0.039) \cdot 10^{-4}$	0.998 ± 0.008
c_3	2.658 ± 0.038	-0.837 ± 0.045	3.641 ± 0.038	-0.11 ± 0.043
c_4	0.388 ± 0.057	0.789 ± 0.062	0.105 ± 0.013	1.042 ± 0.09
c_5	$(-4.994 \pm 0.881) \cdot 10^{-2}$	-0.131 ± 0.011	$(-9.525 \pm 3.231) \cdot 10^{-5}$	-0.663 ± 0.06
c_6	3.241 ± 0.287	1.333 ± 0.304	-0.334 ± 0.062	3.05 ± 0.441
c_7	-0.734 ± 0.045	-0.477 ± 0.054	$(-3.116 \pm 0.169) \cdot 10^{-3}$	-2.978 ± 0.298
max.	0.0377	0.0329	0.0374	0.0342
av.	0.0107	0.00821	0.0123	0.00813
R^2	0.979	0.986	0.972	0.986

6.1.3 Comparison of Results and Fits

In this section, we compare data from four different studies, i.e., Bauswein et al., 2021; Kashyap et al., 2021; Perego et al., 2021, and [Koe1]. Apart from the work by Kashyap et al., 2021, who investigated M_{thr} for a sample of 23 EOSs in the case of equal-mass binaries, these works have been introduced in Sect. 6.1. Out of convenience, we use the following designations: In the case of the large sample of EOSs of Bauswein et al., 2021, we adopt their denominations, i.e., 'b' (hadronic EOSs), 'e' (excluded hadronic EOSs), 'h' (hybrid EOSs). Sometimes we simply refer to their data as the sample 'B'. Further, we label the data of Kashyap et al., 2021, with 'Ka', the data of Perego et al., 2021, with 'P', and data from Ref. [Koe1], with 'K'.

The data sets B, Ka and K all include the EOSs SLy, ALF2 and H4. This allows for a direct comparison of results, which is shown in the right column of Fig. 6.2. In the equal-mass case, we find threshold masses from 'B', to have systematically higher values than those from 'K' and 'Ka', while a similar systematic is not apparent between the data sets 'K' and 'Ka'. The largest difference are $\Delta M_{\text{thr}} \approx 0.07$ between 'B' and 'K', and $\Delta M_{\text{thr}} \approx 0.03$ between 'Ka' and 'K'. Comparing their data to those of 'B', Kashyap et al., 2021, find systematic deviations. However, considering mass ratios $q > 1$, we do not find this observation to hold. The sets 'K' and 'B' appear to be compatible at $\tilde{q} = 0.85$ compared to adjacent data, while threshold masses from 'B' at $\tilde{q} = 0.7$ tend to have lower values compared to adjacent data from 'K'.

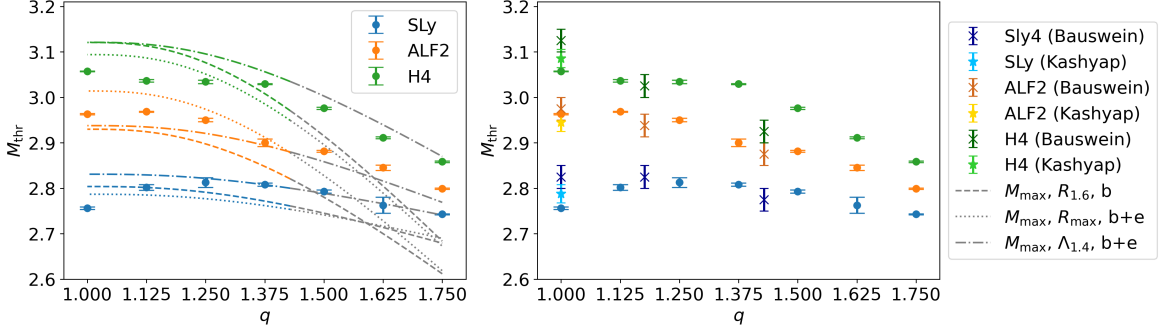


Figure 6.2: Comparison of data and fits. First column: Comparison to fits by Bauswein et al., 2021. Dashed/dotted lines: Fits as found by Bauswein et al. (cmp. Eq. (10), Fig. 5 and TABLE. VI of Bauswein et al., 2021) plotted for the stellar parameters of SLy, ALF2 and H4. The fits are based on different subsets (b, b+e) of data for $\tilde{q} = 1/q \in [0.7, 1.0]$ given in Bauswein et al., 2021. The transition to extrapolation beyond $q = 1/0.7$ is marked by a change to gray color.

Second column: Direct comparison of data. Data points: As in Fig. 6.1. Crosses: Data by Bauswein et al., 2021. Stars: Data by Kashyap et al., 2021.

Figure adapted from Ref. [Koe1].

The data sets 'B', 'Ka', 'K' are based on different numerical codes, and treatments of Einstein's equations and physics relevant after merger (e.g., neutrino treatment): Bauswein et al., 2021 use a conformally flat approximation for the strong regime, Kashyap et al., 2021 applied the WhiskyTHC code (e.g., Radice et al., 2018a), and simulations of Ref. [Koe1] were conducted with BAM. Simulations of the sets 'Ka' and 'K' have been conducted with comparable numerical resolution. While Bauswein et al., 2021, and Kashyap et al., 2021, used the bracketing method, we have used a new approach. The discussed deviations may be related to both the applied codes and threshold-mass methods.

In the left column of Fig. 6.2, we compare data from 'K' to fits from Bauswein et al., 2021, Eq. (6.2). Depicted is a sample of fits to different data subsets and pairs of stellar parameters as given in the legend. Coefficients depend on the subsets of data from 'B', cf. Bauswein et al., 2021, stellar parameters of our EOSs are given in Tab. 3.1. Extrapolations beyond the mass-ratio interval investigated by Bauswein et al. are marked with gray color. It is no surprise to find that for many of the fits given in Bauswein et al., 2021 deviations from our data are the highest for high mass ratios. However, in the case of 'b+e' sample with $Y = \Lambda_{1.4}$ the fit is accurate at high mass ratios. At mass ratios $q < 1/0.7$ we observe unsystematic deviations between our data and the depicted fits to data from 'B'. The highest differences are smaller than $0.2 M_{\odot}$ at high q , in the case $q \leq 1.375$ they smaller than $0.08 M_{\odot}$.

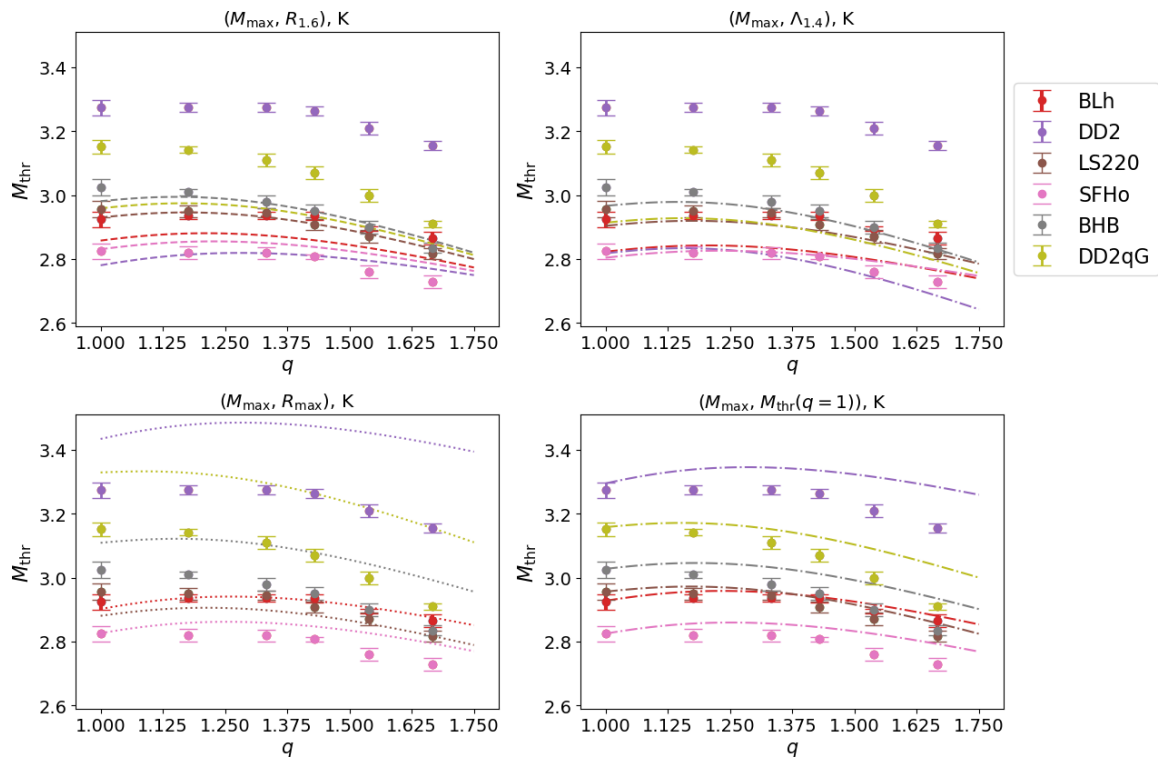


Figure 6.3: Data points: Data of Perego et al., 2021 ('P'). Dashed lines: Fits (Tab. 6.1) using Eq. (6.6) based on data of Ref. [Koe1] ('K'). In each panel a different pair of parameters is used, i.e., $X = M_{\text{max}}$ and $Y \in \{R_{1.6}, \Lambda_{1.4}, R_{\text{max}}, \hat{M}_{\text{thr}}(q=1)\}$. Fits based on the stellar parameters $R_{1.6}$, $\Lambda_{1.4}$ and R_{max} show large deviations from data of 'P'.

We find considerably higher deviations between data and fits, when we use the fits from Tab. 6.1 to predict data from Perego et al., 2021, cf. Fig. 6.3. In each panel of Fig. 6.3, we show fits to Eq. (6.6) based on the same 21 data points (Tab. 5.1), using a different pair of parameters X and Y in each case. Fits based on the stellar parameters $R_{1.6}$, $\Lambda_{1.4}$ and R_{max} , which are extractable from GW signals, show large deviations compared to the respective 'P' data. In the fourth panel we use the threshold mass of the equal-mass case as a parameter, i.e. $Y = \hat{M}_{\text{thr}}(q=1)$. Here we use the respective $q=1$ data points for this purpose, which explains the comparably good agreement between fits (based on 'K') and data (based on 'P'). If no simulation data for the $q=1$ case is available, it is also possible to compute $M_{\text{thr}}(q=1)$ using relations between M_{thr} and stellar parameters, cf. for example Kashyap et al., 2021.

In summary, we do not find our fits to predict threshold masses of different EOSs properly. This can be explained with the small sample of EOSs used for our fits. Therefore, we will combine our data with available data, like those of Perego et al., 2021, to construct more promising models in the next section.

6.1.4 Fits to Combined Sets of Data

To improve the $M_{\text{thr}}(q)$ model, which employs the fit function in Eq. (6.6), we will increase the number of considered EOSs by including data from Perego et al., 2021. In Ref. [Koe1], we have also considered fits based on the combined data set 'B' + 'K' and Eq. 6.2, cf. 'K+b+e+h' sample in Tab. 6.3. While in the case of 'K' and 'P', similar mass-ratio intervals are covered, this is not the case for 'B' and 'K'. In the 'K+b+e+h' case, the large uncertainties of the fits' coefficients, cf. Tab. 6.3, may be a result of the mass-ratio interval's dissimilarity. Individual fits of 'B' (cf. Bauswein et al., 2021) and 'K' (cf. Tab. 6.3) data based on Eq. (6.2) lead to much smaller uncertainties of the coefficients.

Combining the data sets 'K' and 'P', we fit 21 + 36 data points of 3 + 6 EOSs by means of a least-squares approach. We ignore error estimates of the individual methods used to determine M_{thr} and use the same four pairs of parameters as in Sect. 6.1.3. The fits are presented in Fig. 6.4 in comparison to the employed data. The fits' coefficients are reported in Tab. 6.2.

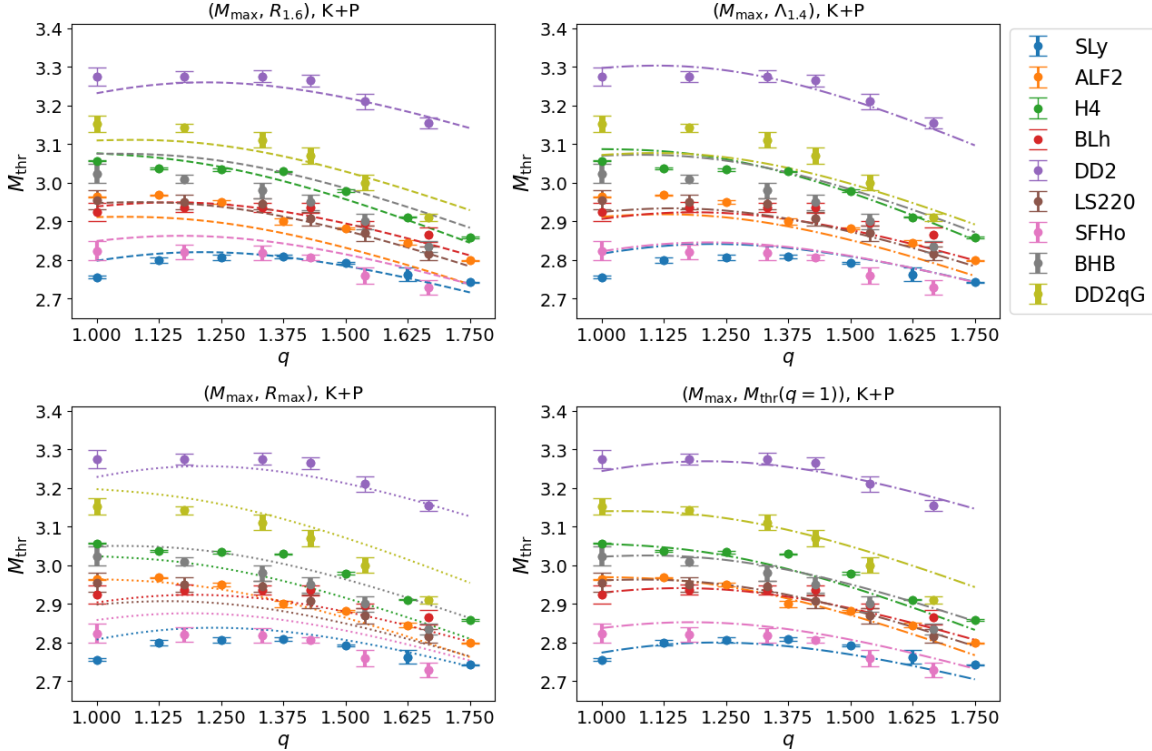


Figure 6.4: Fit of the data set K+P, which includes data by Perego et al., 2021. The fit is based on Eq. (6.6) and the parameter pair $(X, Y) = (M_{\text{max}}, M_{\text{thr}}(q = 1))$. Coefficients are given in Tab. 6.2. Plot in the lower right taken from Ref. [Koe1].

With respect to R^2 , fits based on parameters $Y \in \{R_{1.6}, \Lambda_{1.4}, R_{\max}\}$ are in good agreement with the data. However, comparing data and fits in the first column of Fig. 6.4, we take notice of the case of BHB and H4. While all data related to H4 have higher values of M_{thr} , we find the opposite relation for the respective fit curves. An explanation for this may be found in the similarity of the respective radii, i.e., $(R_{1.6}, R_{\max}) = (13.2 \text{ km}, 11.59 \text{ km})$ in the case of BHB compared to $(R_{1.6}, R_{\max}) = (13.5 \text{ km}, 11.62 \text{ km})$ in the case of H4. Considering the upper right panel of Fig. 6.4 ($Y = \Lambda_{1.4}$), we find sets of two to three fit curves to be packed together tightly, i.e., (BHB, DD2qG, H4), (ALF2, BLh, LS220) and (SFHo, SLy). The groups of EOSs with closely packed fit curves are characterized by maximum masses and tidal parameters of similar magnitude, cf. Tab. B.1 (appendix) for the complete set of parameters.

For the fourth panel of Fig. 6.4, we again employ M_{\max} together with $\hat{M}_{\text{thr}}(q=1)$ as parameters, using the respective $q=1$ data point for $\hat{M}_{\text{thr}}(q=1)$. Predictably, we obtain fits that are in good agreement with the data low mass ratios. Considering R^2 , the fit is notably improved compared with the ones employing the stellar parameters $R_{1.6}$, $\Lambda_{1.4}$ and R_{\max} , cf. Tab. 6.2. Employing only the sample 'K', cf. Tab. 6.1, fits with parameters $R_{1.6}$, $\Lambda_{1.4}$ and R_{\max} are of comparable quality to the one with $Y = \hat{M}_{\text{thr}}(q=1)$. In either case, the coefficient c_1 becomes neglectable and c_2 takes on values close to 1.0 when $\hat{M}_{\text{thr}}(q=1)$ is employed. This indicates that a different strategy may be preferable for fits with $\hat{M}_{\text{thr}}(q=1)$ as a parameter. In this context, it is worth mentioning that in the case of $q=1$, the fit formula (6.6) takes the form

$$M_{\text{thr}}(1, X, Y) = c_1 X + c_2 Y + c_3 , \quad (6.7)$$

i.e., the first three coefficients model the threshold mass of equal-mass binaries. However, applying a least-squares method to Eq. (6.6), also data of mass ratios greater than one are taken into consideration to determine these coefficients. On the path to Eq. (6.2), Bauswein et al., 2021, also consider fits of the form

$$M_{\text{thr}}(q) = -\frac{\Delta M_{\text{thr}}}{0.3^3} \delta \tilde{q}^3 + M_{\text{thr}}(q=1) , \quad (6.8)$$

with $\Delta M_{\text{thr}} = M_{\text{thr}}^{\tilde{q}=1} - M_{\text{thr}}^{\tilde{q}=0.7}$, and 0.3 being the width of the mass-ratio interval considered in their work. Considering that fits in Fig. 6.4 tend to be off at either end of the considered mass-ratio interval, we conclude that an analogous term, i.e., $\Delta M_{\text{thr}}^{1.75} = M_{\text{thr}}^{q=1} - M_{\text{thr}}^{q=1.75}$, might be used in a more clever ansatz where a stronger emphasis is put on the endpoints of the interval.

Table 6.2: Same as Tab. 6.1, but for the combined set (K+P) of 57 threshold mass data points; (K, 21 data points) together with data from Ref. Perego et al., 2021 (P, 36 data points). The best fit is achieved for the parameter pair $(X, Y) = (M_{\max}, \hat{M}_{\text{thr}}(q = 1))$. Table taken from Ref. [Koe1].

$M_{\text{thr}}(q, X, Y) = c_1 X + c_2 Y + c_3 + c_4 \delta\tilde{q} X + c_5 \delta\tilde{q} Y + c_6 \delta\tilde{q}^3 X + c_7 \delta\tilde{q}^3 Y, \delta\tilde{q} = 1 - \tilde{q}$				
(X, Y)	$(M_{\max}, R_{1.6})$	(M_{\max}, R_{\max})	$(M_{\max}, \Lambda_{1.4})$	$(M_{\max}, \hat{M}_{\text{thr}}(q = 1))$
c_1	0.462 ± 0.094	0.428 ± 0.094	0.686 ± 0.049	$(-3.627 \pm 8.917) \cdot 10^{-2}$
c_2	0.14 ± 0.016	0.134 ± 0.017	$(5.049 \pm 0.655) \cdot 10^{-4}$	0.93 ± 0.064
c_3	0.251 ± 0.107	0.602 ± 0.104	1.249 ± 0.093	0.285 ± 0.067
c_4	0.76 ± 0.638	0.886 ± 0.62	0.162 ± 0.136	1.149 ± 0.626
c_5	-0.12 ± 0.106	-0.16 ± 0.117	$(-3.921 \pm 4.616) \cdot 10^{-4}$	-0.78 ± 0.44
c_6	0.00817 ± 3	-0.539 ± 3.396	-0.808 ± 0.735	0.932 ± 3.353
c_7	-0.188 ± 0.573	-0.112 ± 0.638	$(-1.406 \pm 2.471) \cdot 10^{-3}$	-1.447 ± 2.353
max.	0.0843	0.0848	0.0800	0.0704
av.	0.0287	0.0341	0.0303	0.0182
R^2	0.938	0.926	0.934	0.974

Table 6.3: Results for coefficients c_1 to c_5 : fitting threshold mass data (sample K: 21 data points as reported in Tab. 5.1) for three pairs of stellar parameters (X, Y) to $M_{\text{thr}}(q, X, Y) = c_1 X + c_2 Y + c_3 + c_4 \delta\tilde{q}^3 X + c_5 \delta\tilde{q}^3 Y, \delta\tilde{q} = 1 - \tilde{q}$ by means of a least squares approach. Combined fits are given for $Y \in \{R_{1.6}, \Lambda_{1.4}\}$ based on the sample 'K' and the data of Bauswein et al. presented in Tab. IX of Bauswein et al., 2021. In columns seven to nine we present the following measures of variation: the maximal absolute residual (max.), the mean absolute residual (av.), and the coefficient of determination (R^2). Table taken from Ref. [Koe1].

$M_{\text{thr}}(q, M_{\max}, R_{1.6}) = c_1 M_{\max} + c_2 R_{1.6} + c_3 + c_4 \delta\tilde{q}^3 M_{\max} + c_5 \delta\tilde{q}^3 R_{1.6}$									
K	-0.374 ± 0.047	0.104 ± 0.002	2.413 ± 0.086	3.087 ± 0.176	-0.655 ± 0.027	0.072	0.0109	0.9632	21
K+b+e+h	0.675 ± 0.559	0.15 ± 0.106	-0.315 ± 1.191	5.313 ± 25.98	-1.031 ± 4.371	0.148	0.0365	0.9602	141
$M_{\text{thr}}(q, M_{\max}, R_{\max}) = c_1 M_{\max} + c_2 R_{\max} + c_3 + c_4 \delta\tilde{q}^3 M_{\max} + c_5 \delta\tilde{q}^3 R_{\max}$									
K	0.871 ± 0.039	0.164 ± 0.003	-0.612 ± 0.069	3.969 ± 0.383	-0.903 ± 0.075	0.048	0.0106	0.9762	21
$M_{\text{thr}}(q, M_{\max}, \Lambda_{1.4}) = c_1 M_{\max} + c_2 \Lambda_{1.4} + c_3 + c_4 \delta\tilde{q}^3 M_{\max} + c_5 \delta\tilde{q}^3 \Lambda_{1.4}$									
sample	c_1	$c_2/10^{-4}$	c_3	c_4	$c_5/10^{-4}$	max.	av.	R^2	N
K	-0.371 ± 0.044	3.71 ± 0.05	3.481 ± 0.087	-0.177 ± 0.037	-2.47 ± 0.093	0.075	0.0126	0.9568	21
K+b+e+h	0.67 ± 0.495	5.338 ± 4.097	1.271 ± 0.986	-0.042 ± 5.759	-3.347 ± 19.33	0.131	0.0456	0.9512	141

6.2 Tidal Polarizability

For a given mass ratio, the tidal polarizability parameters κ_2^T and $\tilde{\Lambda}$ are decreasing functions in M , cf. Fig. 3.2. Therefore, it is possible to uniquely relate the threshold mass to a q -dependent threshold value of the tidal polarizability parameters, i.e., configurations with a given mass ratio and $\kappa_2^T < (\kappa_2^T)_{\text{thr}}(q)$, or respectively $\tilde{\Lambda} < \tilde{\Lambda}_{\text{thr}}(q)$, will undergo prompt collapse. For our highest-resolution data, this relation is visualized in the first row of Fig. 6.5, where prompt collapse (coloured points) and delayed collapse (gray points) are distinguished based on the collapse-time criterion applied to R3-data, i.e., all data with $t_{\text{coll}}^{(R3)} > \tau_{\text{thr}}$ are marked as delayed-collapse mergers.¹ Tidal parameters of threshold configurations ($M = M_{\text{thr}}$) are marked with crosses.

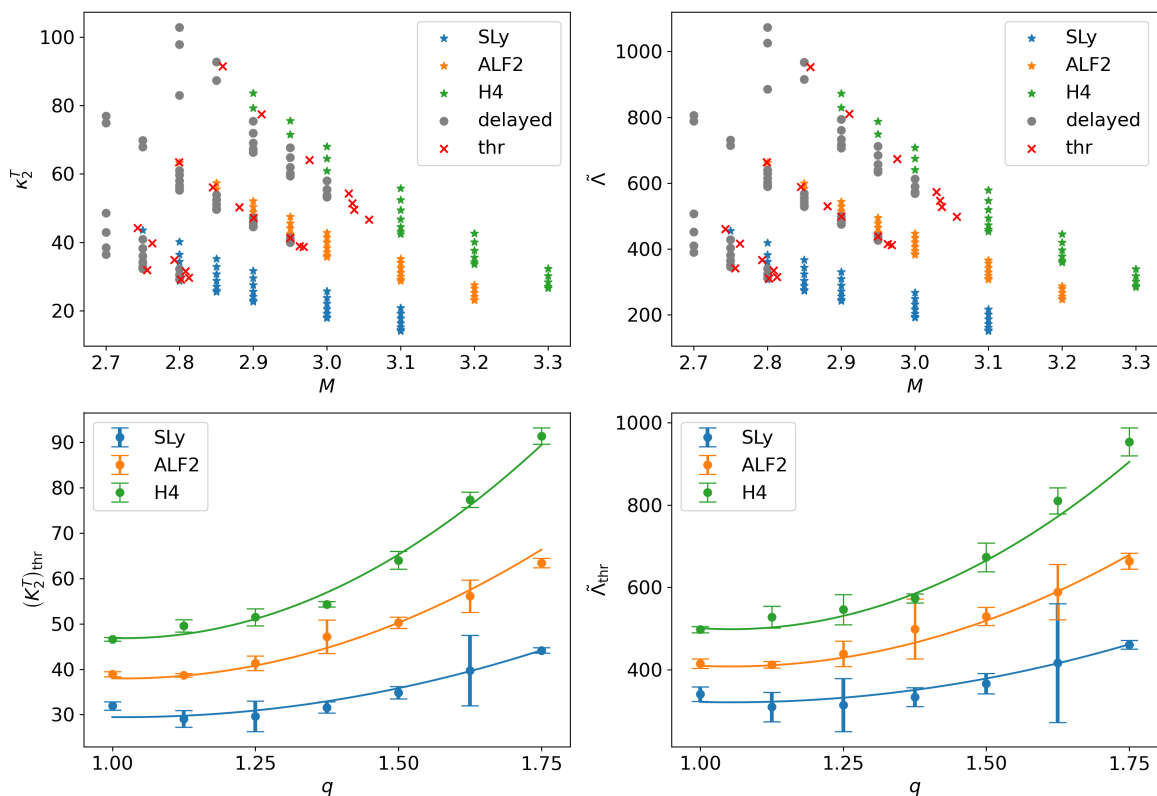


Figure 6.5: Upper row: Tidal polarizability parameters κ_2^T (first column) and $\tilde{\Lambda}$ (second column) plotted against the total mass M . Included are all collapse scenarios. Prompt-collapse scenarios (coloured) are distinguished from delayed-collapse scenarios (gray). Crosses mark quantities at the threshold to prompt collapse as determined for $M = M_{\text{thr}}$. Lower row: Tidal parameters at the threshold to prompt collapse as a function of the mass ratio q . Solid lines are fits over all data using Eq. (6.11). Plots taken from Ref. [Koe1].

¹This is not necessarily equivalent to $M > M_{\text{thr}}$, cf. discussion in Sect. 5.2.3.

Analysing merger simulations from the CoRe collaboration of binaries with comparable mass, Bernuzzi, 2020, found (q -independent) relations describing the tidal parameters of prompt collapse mergers. In Ref. [Koe1], we examined these relations. Bernuzzi, 2020, state that the tidal polarizability parameters $\tilde{\Lambda}$ and κ_2^{T} of prompt-collapse mergers are characterized by the inequalities

$$\kappa_2^{\text{T}} < (\kappa_2^{\text{T}})_{\text{thr}} \sim 80 \pm 40 , \quad (6.9)$$

$$\tilde{\Lambda} < \tilde{\Lambda}_{\text{thr}} \sim 362 \pm 24 , \quad (6.10)$$

where $(\kappa_2^{\text{T}})_{\text{thr}}$ and $\tilde{\Lambda}_{\text{thr}}$ mark the upper limit in the prompt-collapse case. Comparing these findings to our data, cf. first row of Fig. 6.5, we made two observations with regards to our data:

- Relation (6.9) is met by all data points presented in Fig. 6.5 (cmp. panel on the upper left).
- Relation (6.10) captures only a small number of our threshold data points (cmp. panel on the upper right of Fig. 6.5).

Table 6.4: Fits describing the EOS dependence of the tidal polarizability parameter κ_2^{T} and the tidal polarizability coefficient $\tilde{\Lambda}$ of BNS configurations at the threshold to prompt collapse as a function of the mass ratio q . We also present the following measures of variation: the maximal relative residual (max.), the mean absolute residual (av.), and the coefficient of determination (R^2). Table adapted from Ref. [Koe1].

$Z_{\text{tidal}}^{\text{thr}} = c_1 + c_2 \tilde{\Lambda}_{1.4} + c_3 \tilde{\Lambda}_{1.4} q + c_4 \tilde{\Lambda}_{1.4} q^2$								
$Z_{\text{tidal}}^{\text{thr}}$	c_1	c_2	c_3	c_4	max.	av.	R^2	
$(\kappa_2^{\text{T}})_{\text{thr}}$	20.221 ± 1.363	0.124 ± 0.019	-0.184 ± 0.029	0.090 ± 0.011	7.75%	1.18	0.991	
$\tilde{\Lambda}_{\text{thr}}$	226.867 ± 21.162	1.359 ± 0.310	-1.997 ± 0.484	0.947 ± 0.183	6.71%	14.6	0.986	

Seeking to improve and to generalize these inequalities with respect to mass-ratio effects, in Ref. [Koe1], we developed empirically motivated fits of the form

$$Z_{\text{tidal}}^{\text{thr}} = c_1 + c_2 \Lambda_{1.4} + c_3 \Lambda_{1.4} q + c_4 \Lambda_{1.4} q^2, \quad (6.11)$$

where Z_{tidal} may stand for either of the tidal parameters κ_2^{T} and $\tilde{\Lambda}$. The fit function is designed to model the value of the tidal deformability parameters $Z_{\text{tidal}}^{\text{thr}}$ at threshold to prompt collapse. Fits are performed by application of a least-squares method to all 21 data points. The fit curves are portrayed in the second row of Fig. 6.5. The respective

coefficient c_1 to c_4 are given in Tab. 6.4. The fit formula applied to $Z_{\text{tidal}} \in \{\kappa_2^T, \tilde{\Lambda}\}$ is a polynomial of second order in q . Properties of different EOSs are factored in via a linear dependence on the stellar parameter $\Lambda_{1.4}$. Based on this model for threshold values $Z_{\text{tidal}}^{\text{thr}}(q)$, prompt-collapse and delayed-collapse scenarios can be distinguished for different mass ratios and EOSs, i.e.,

$$Z_{\text{tidal}}^{\text{delayed}} > Z_{\text{tidal}}^{\text{thr}}(q) > Z_{\text{tidal}}^{\text{prompt}}. \quad (6.12)$$

In the case of our small sample of EOSs, and for each mass ratio, we find the $Z_{\text{tidal}}^{\text{thr}}$ to be linearly related to $\Lambda_{1.4}$. The equal-mass case is illustrated in the first panel of Fig. 6.6, where $\tilde{\Lambda}_{\text{thr}}$ data are plotted against $\Lambda_{1.4}$. Our data are marked with their usual colours, and the purple line is the fit function of Eq. (6.11) with coefficients of Tab. 6.4, interpreted as a function of $\Lambda_{1.4}$ in the case of $q = 1$. We compare this fit to threshold tidal parameters determined by Kashyap et al., 2021 (black data points), for 23 EOSs. Our fit lies within the error bars of more than half of these data points. In some cases there are, however, large deviations which suggest a more complex picture. Equipped with a data set containing a larger set of EOSs, this shortcoming may be corrected by including dependencies on a second stellar parameter. In Sect. 6.1.4, we discussed combined fits of our M_{thr} data and data by Perego et al., 2021 to generate more general models. It would be interesting to compare results over a broader range of mass ratios. However, due to lack of data regarding the tidal parameters of the EOSs studied by Perego et al., 2021, we cannot take the same approach here.

The second panel of Fig. 6.6 shows threshold values of the tidal polarizability coefficients as determined in Ref. [Koe1] (cf. Tab. 5.1) as a function of the threshold mass. For each EOS and at high mass ratios (lighter coloring), $\tilde{\Lambda}_{\text{thr}}(M_{\text{thr}})$ increases linearly for decreasing M_{thr} . At low mass ratios (darker colouring), the $\tilde{\Lambda}_{\text{thr}}$ -line may curve within the $(\tilde{\Lambda}_{\text{thr}}, M_{\text{thr}})$ -plane; this is especially noticeable in the case of SLy. Bauswein et al., 2021, and Kashyap et al., 2021, consider critical lines of the form

$$M_{\text{thr}} = a M_{\text{max}} + b \tilde{\Lambda}_{\text{thr}} + c, \quad (6.13)$$

that divide the $(M_{\text{thr}}, \tilde{\Lambda}_{\text{thr}})$ -plane into allowed and excluded regimes. The dashed lines in the second panel of Fig. 6.6 are based on the large set of EOSs studied by Bauswein et al., 2021.² In accordance with the mass-ratio sample studied by Bauswein et al.,

²The critical lines given in Fig. 6.6 are based on the sample b+h+e. Coefficients are taken from lines 49-51 of Tab. II of Bauswein et al., 2021.

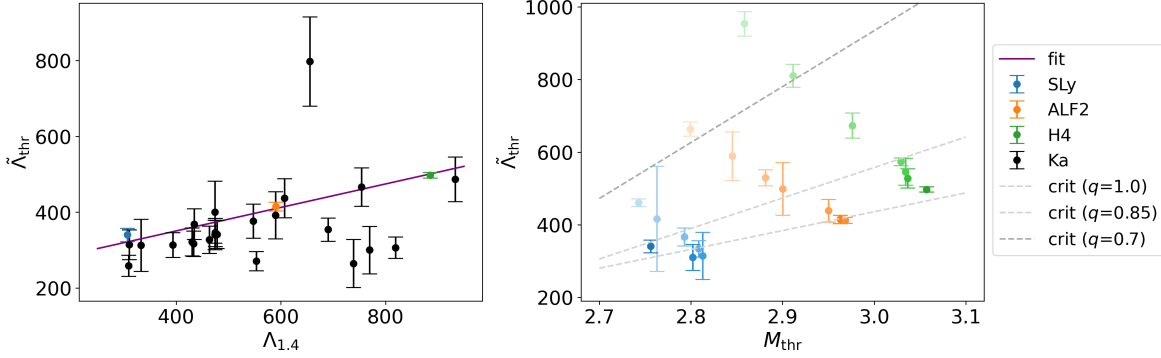


Figure 6.6: First column: Equal-mass case: Tidal polarizability coefficient $\tilde{\Lambda}$ at threshold as a function of the stellar parameter $\Lambda_{1.4}$. Black data points: data from Kashyap et al., 2021, ('Ka'). Coloured data points: $q = 1$ data from Ref. [Koe1], ('K'). Purple line: Fit function (6.11), with coefficients of Tab. 6.4, for fix mass ratio $q = 1$ interpreted as a function of $\Lambda_{1.4}$. Second column: Tidal polarizability coefficient $\tilde{\Lambda}_{\text{thr}}$ as a function of M_{thr} ; data of different mass ratios are distinguished by colour shades (darkest at $q = 1$). Dashed lines: Critical lines as determined by Bauswein et al., 2021, for $q \in \{1.0, 0.85, 0.7\}$ and a maximum mass of $M_{\text{max}} = 1.97 M_{\odot}$. Threshold values above the critical lines ($M_{\text{max}} < M_{\text{max}}^{\text{obs}}$) are excluded.

2021, three critical lines are included, i.e., $q \in \{1.0, 0.85, 0.7\}$. For the maximum-mass parameter, we use the constraint found by Abbott et al., 2018, i.e., $M_{\text{max}} = 1.97 M_{\odot}$, which is the minimal value of M_{max} considered by Bauswein et al., 2021, in this context, cf. for example Fig. 8 of their work. With respect to the gray lines, two of our $q = 1$ data points appear to be in the excluded regime above the $q = 1$ line, which is characterized by maximum masses smaller than $M_{\text{max}} = 1.97 M_{\odot}$, cf. discussions in Bauswein et al., 2021 and Kashyap et al., 2021. However, all three of the considered EOSs are compatible with the employed maximum-mass parameter, cf. Tab. 3.1. Therefore, we do not consider this a problematic issue. In the case of unequal-mass binaries, our data are without exception compatible with the respective critical lines.

Kashyap et al., 2021, consider universal, i.e., EOS independent, relations between stellar properties to calibrate a set of two million phenomenological EOSs obtaining constraints on NS properties. Particularly, compactness and tidal polarizability are related to M_{max} to determine upper and lower limits. Furthermore, Kashyap et al., 2021, include the threshold mass in their considerations. The identification of future BNS-merger observations as prompt or delayed will put upper and lower limits to the allowed regions in the $(M_{\text{thr}}, M_{\text{max}})$ plane. With increasing number of BNS observations, tight constraint on the NS EOS are expected.

6.3 Properties of Remnant Systems

Properties of the remnant system strongly depend on dynamics at merger, which in turn are effected by multiple factors. Considering simulations of BNS mergers which lead to the formation of a BH within simulation time, we will focus our attention on the remnant BH's mass and the disk mass. We will discuss the qualitative effects of M , q and the EOS on the remnant system. In this context, we will often distinguish between the cases of prompt-collapse and delayed-collapse mergers. Following the approach of Ref. [Koe1], we will review a sample of studies on ejection mechanisms with regard to the effect of mass ratio. Subsequently, we compare data of our simulation campaign to these findings. In closing, we approximate properties of remnant systems with $M \approx M_{\text{thr}}$.

6.3.1 Ejection Mechanisms and Mass-Ratio Effects

The multi-messenger observation of GW170817, AT2017gfo, and GRB170817A, cf. Abbott et al., 2017c; Abbott et al., 2017a, proves that the GW signal of a BNS merger may be followed by counterparts in the electromagnetic (EM) spectrum. These EM signals are connected to the amount of matter ejected from the system, or accumulated in a disk surrounding the merger remnant, in consequence of the neutron stars' coalescence, cf. for example Shibata et al., 2006; Metzger et al., 2012; Piran et al., 2013. In the case of GW190425 on the other hand, no EM signature has been observed, cf. for example Coughlin et al., 2020; Dudi et al., 2021. While the non-detection may have other causes, cf. discussion by Coughlin et al., 2020, the likely explanation in this case can be found in the binary's high total mass which has most likely caused a prompt collapse, Abbott et al., 2020a. The spectrum and the origin of EM emissions, e.g. optical and infrared emissions due to rapid neutron capture or radio emissions due to the interaction of merger ejecta with the ambient medium, cf. Abbott et al., 2017b, are a major topic, which we will forgo in our discussion. Instead, we will leave it at the simple relation that more ejected material entails stronger EM signals. Focussing our attention on mechanisms causing the ejection of matter³, we will approach this topic from the viewpoint of simulation campaigns treating BNS mergers of asymmetric binaries.

³We do not limit the use of the term *ejection of matter* to the case where matter becomes unbound, rather any process which causes matter to become disconnected from the original stars or the merger remnant may be implied. This especially includes the case of matter accumulated in a disk around the remnant.

An early study identifying different ejection mechanisms is the one by Hotokezaka et al., 2013, who investigated the mass ejection from BNS mergers for small mass ratios, $1 \leq q \leq 1/0.8$, and 4 different EOSs. The BNS configurations considered in their study either lead to the formation of HMNS or BH remnants. Comparing these two cases, they find larger amounts of ejected material in the case of HMNS remnants. With respect to the mass ratio, they find unequal-mass binaries to eject larger amounts of matter. Analysing snapshots of the density and the specific internal energy, they identify two ejection mechanisms: Shock heating (heated-up material is pushed outwards, see also Bauswein et al., 2010) and angular momentum transport (e.g. torque exerted by the HMNS to the surrounding material). They find the first mechanism to be efficient to eject matter from HMNSs in the phase after merger, particularly in the case of binaries with $q \approx 1$. Naturally, it plays no important role in the case of BH remnants, i.e., in the case of prompt collapse, cf. Fig. 4.1. Considering the second mechanism in case of a HMNS remnant at the time after merger, Hotokezaka et al., 2013, find the rapidly rotating HMNS an efficient torque supplier which increases the angular momentum of surrounding material. Eventually velocities exceed the escape velocity and matter becomes unbound. In the early phase of merger, and in case of unequal-mass binaries, the less massive component gets tidally elongated due to torque exerted by the primary component. This effect is especially important in the case of prompt BH formation. In any case, tidal tails formed due to the tidal elongation in the case of asymmetric binaries will not completely be ejected from the remnant system. Parts of the tidal tails will remain in a rotationally supported disk, cf. Radice et al., 2018a.

Considering BNS configurations over a broader mass-ratio range (up to $q = 2.06$), Dietrich et al., 2017, make out two effects causing mass ejection in their simulations. There is ejection of matter due to shocks following the collision of the NS cores. And there are centrifugal effects causing the matter to be expelled from the tidal tail of the secondary component, or in more asymmetric cases, ejection due to the partial tidal disruption of the secondary component. The production of large amounts of ejected material, due to tidal disruption, has also been observed by Bernuzzi et al., 2020. To mention another interesting finding connected to high mass ratios: Bernuzzi et al., 2020, argue that there are different mechanisms defining the dynamics of prompt collapse in the case of high q compared to the equal-mass case. In the case of highly asymmetric binaries, prompt collapse is induced by accretion onto the primary component.

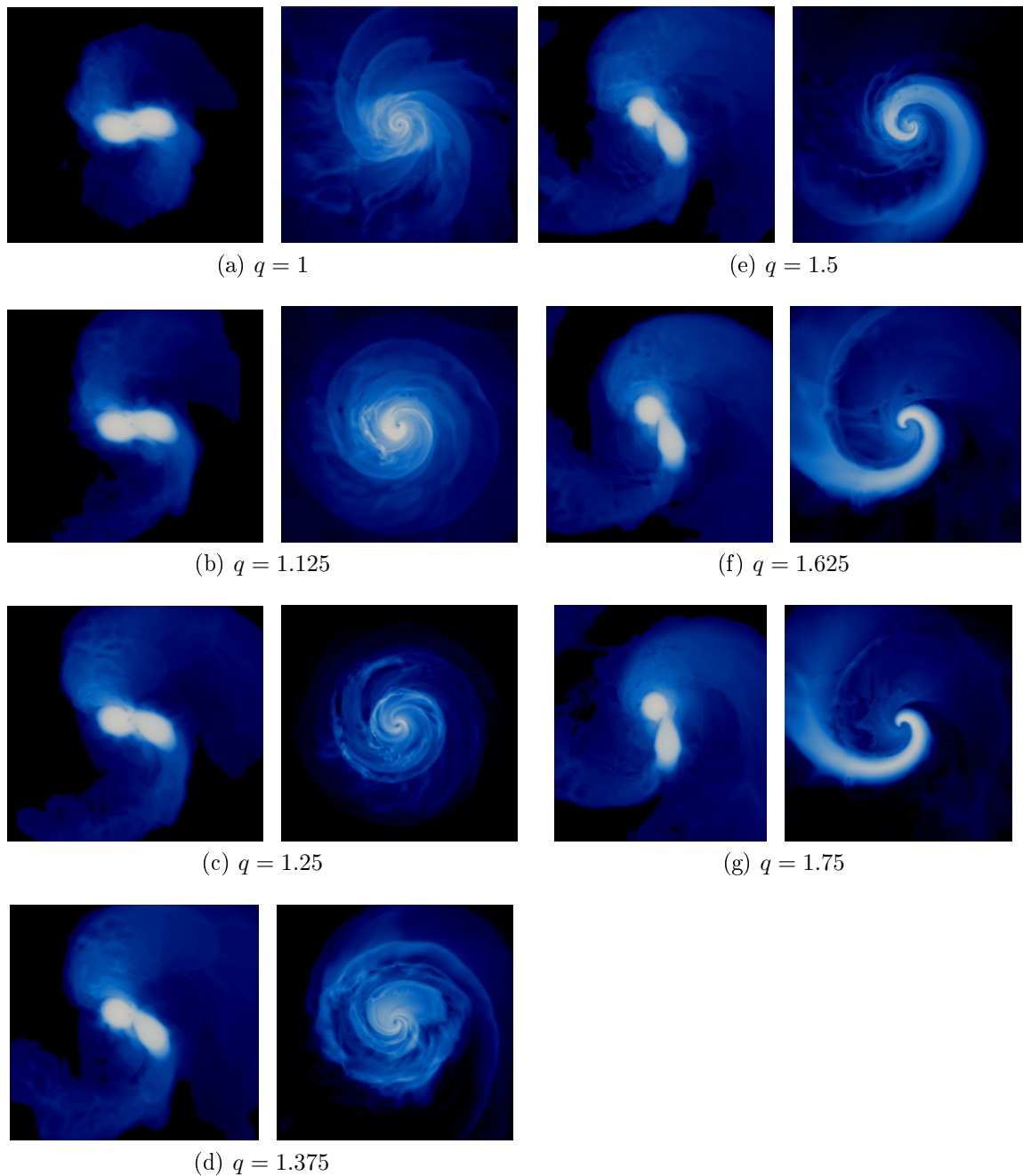


Figure 6.7: Snapshots of $\log_{10} \varrho$ within the orbital plane close to the time of merger for varying mass ratio, a fix total mass, $M = 2.8 M_{\odot}$, and the EOS SLy. For each mass ratio, two times are shown: The onset of merger $t_1 \approx t_{\max}$, and a time t_2 shortly after t_{AH} when the major part of NS matter has been swallowed by the remnant BH. For increasing q , the tidal deformation of the binary's less massive component increases. In the case of high mass ratios, this results in the formation of a tidal tail and a more massive disk. (Due to rescaling, colour maps are not comparable.)

Distinguishing between prompt-collapse and delayed-collapse scenarios, Dietrich et al., 2017, find no massive disks in the case of prompt BH formation. This coincides with conclusions of Bernuzzi et al., 2020, and Radice et al., 2018a, who argue that the bulk of dynamical ejecta is connected to the bounce of NS cores. Considering this effect while bearing in mind that the absence of a core-bounce, i.e., monotonically decreasing maximum-density, is a criterion for prompt collapse, we conclude that only small amounts of ejected material are to be expected in any prompt-collapse scenario.

The discussed tidal effects at merger are visualized in Fig. 6.7, which shows an example case of given total mass and EOS. The depicted series of snapshots of the density shows the increasing tidal effects at merger due increasing asymmetry. For each mass ratio, two times are shown: The onset of merger $t_1 \approx t_{\max}$, and a time t_2 shortly after BH formation, i.e. $t \approx t_{\text{AH}}$.⁴ Going from $q = 1$ to $q = 1.75$, we observe the increasing tidal elongation of the binary's less massive component at the time of merger. At high mass ratios (right side of Fig. 6.7), the secondary component has been tidally disrupted leaving behind a tidal tail winding round the freshly formed BH in a long spiral. In the case of intermediate mass ratios, we find the tidal tails wound up at a tighter distance.

6.3.2 Remnant Properties - Qualitative Effects

Total mass, mass ratio and EOS affect the properties of the remnant system, cf. Figs. 3.5 and 3.6. Furthermore, there are notable differences between the cases of prompt-collapse and delayed-collapse mergers, cf. Fig. 6.8. Following our approach in Ref. [Koe1], and to aid our discussion, we define the mass ratios Q_{disk} and Q_{BH} ,

$$Q_{\text{disk}} := \frac{M_{\text{disk}}}{M^{\text{b}}}, \quad (6.14)$$

$$Q_{\text{BH}} := \frac{M_{\text{BH}}}{M}, \quad (6.15)$$

where we relate the disk mass to the total baryonic mass and the remnant BH's gravitational mass to the total mass. Considering the third and fourth row of Fig. 3.6, where M_{BH} and Q_{BH} are plotted against M , we find the ratio Q_{BH} to be a helpful quantity to investigate the effect of M on the remnant BH's mass. Distinguishing between prompt and delayed collapse, cf. second column of Fig. 6.8, we find that in

⁴The time interval $t_2 - t_1$ does not have a constant length throughout the series. In fact, the series contains prompt-collapse cases ($q = 1.0, 1.5, 1.625, 1.75$) and delayed-collapse cases ($q = 1.125, 1.25, 1.375$).

the case of prompt collapse, the remnant BH's mass varies only by a few percent with respect to the initial total mass of the binary, while its ratio of M is notably smaller in the case of delayed-collapse mergers. Considering the quantities M_{disk} and Q_{disk} on the other hand, we find no striking differences between the curves $M_{\text{disk}}(M)$ and $Q_{\text{disk}}(M)$. However, it seems convenient to present the disk mass as a percentage of the initial baryonic mass.

Naturally, we find the disk mass and the BH mass to behave in a complementary way. Fig. 6.8 shows, that the same is true for M_{disk} and χ_{BH} : The more material is accumulated in the disk, the less material spins up the remnant BH. With this statement, we do not intent to imply that only an insignificant part of the ejected material becomes unbound. At lower mass ratios, this would probably even be a false statement, cf. for example $q = 1.125$ with EOS SLy or ALF2 in Fig. 6.8: In the case of delayed collapse mergers, there is a steep drop in Q_{BH} , which is not accompanied by a proportionate increase of the disk mass. Concluding from the discussion in Sect. 6.3.1, we can expect the amount of ejected material to grow with the survival time of the HMNS remnant. While we limit our discussion to properties of the remnant system, it may be interesting to study the effect of mass ratio on the distribution of ejecta onto the categories of bound and unbound matter, i.e., determining the ratio of ejecta becoming unbound to those accumulated in the disk around the remnant BH. Comparing M_{disk} and Q_{BH} we suspect an increasing dominance of bound material for increasing asymmetry of BNSs. In the case of highly symmetric binaries and long-lived HMNS remnants unbound material may be predominant.

Considering the disk mass over the investigated mass ratio range, we find M_{disk} to be orders of magnitude smaller in the case of small mass ratios compared to the case of intermediate and high mass ratios. This is especially true in the case of prompt collapse, where M_{disk} often is negligible, cf. panels one and two in the first column of Fig. 6.8. Going from small to high mass ratios, the disk mass grows non-linearly with q . However, in the case of lowest investigated total masses, we find that the maximum of $M_{\text{disk}}(q)$ can be located at intermediate mass ratios, cf. the case of SLy and ALF2 in first row of Fig. 3.5. This change of behaviour at low M resembles the behaviour of the collapse that we have discussed in Sect. 5.1. We note that with increasing survival time of the HMNS remnant, the continuous ejection of matter due to shock heating and angular momentum transport starts to dominate, compared to tidal effects at the time of merger, and even compared to tidal disruptions in the case of highly asymmetric binaries.

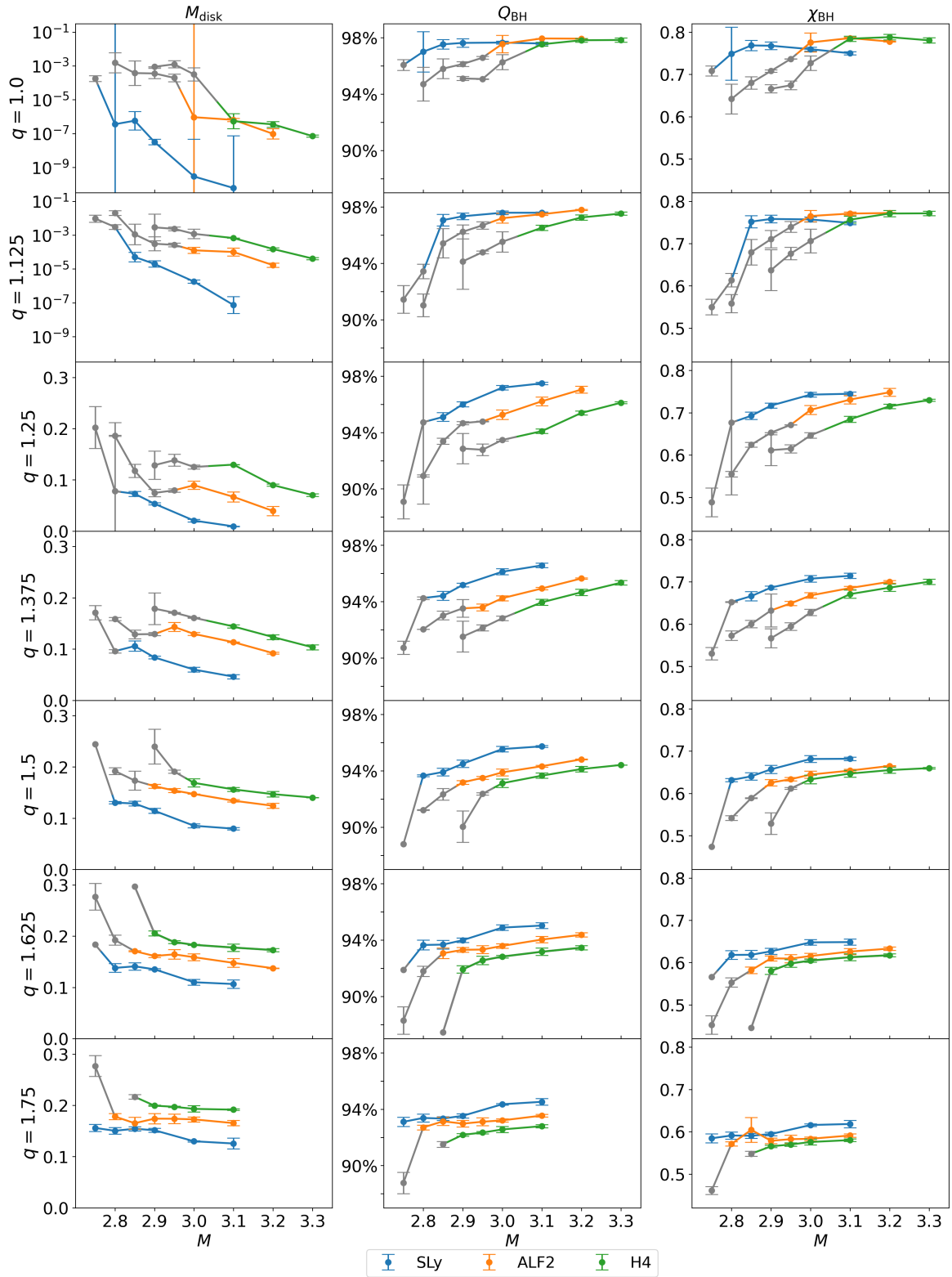


Figure 6.8: M_{disk} , Q_{BH} , and χ_{BH} at $t = t_{\text{AH}} + 5$ ms plotted against M for varying q . Connected data points belong to the same EOS. Delayed-collapse mergers are marked in gray. For given EOS and q , the disk mass is smaller in the case of prompt collapse compared to the case of delayed collapse, while Q_{BH} and χ_{BH} are larger in the case of prompt collapse. A subset of plots of the first and second column are taken from Ref. [Koe1].

Regarding the impact of the EOS, we find the qualitative ordering of properties of the remnant system in accordance with the stiffness of the investigated EOSs. For given q and M , the disk mass is always the smallest in the case of our softest EOS, SLy. The largest disk masses are always related to our stiffest EOS, H4, cf. Fig. 6.8. This is in accordance with findings by previous studies. In the case of highly asymmetric binaries, Bernuzzi et al., 2020, find the largest tails to be produced by the softest EOSs. Hotokezaka et al., 2013, found stronger shocks in the case of soft EOSs. Unsurprisingly, we find the opposite ordering compared to the case of the disk mass for Q_{BH} and χ_{BH} . Considering small mass ratios, there is a notable exception to this rule, as $Q_{\text{BH}}(M)$ and $\chi_{\text{BH}}(M)$ appear to decline at large M . Considering the BH spin, we note that for all of our simulations χ_{BH} is smaller than 0.8. As discussed by Bernuzzi et al., 2020, this may be an upper limit to the BH spin, see also Dietrich et al., 2017; Bernuzzi et al., 2016b; Bernuzzi et al., 2014.

6.3.3 Approximating Remnant Properties at Threshold

Concluding this chapter, we consider approximate models of remnant properties at threshold. Due to the structure of our parameter space, cf. Sect. 3.2 and discussion in Sect. 5.2.1, the vicinity of the threshold to prompt collapse remains underresolved within our set of data. Seeking to estimate masses of the disk and the remnant BH of BNS configurations with $M \approx M_{\text{thr}}$, we have to manage with the available data. Considering the often steep transition from the prompt-collapse to the delayed-collapse regime, cf. Fig. 6.8 and discussion in Sect. 6.3.2, we are going to employ data of the prompt-collapse regime to estimate quantities at threshold. Thereby we will introduce small systematic errors (of a few percent). Motivated by the discussion in Sect. 6.3.2, we presume the following inequalities

$$Z_{\text{disk}}^{\text{delayed}} \geq Z_{\text{disk}}^{\text{thr}} \geq Z_{\text{disk}}^{\text{prompt}}, \quad (6.16)$$

$$Z_{\text{BH}}^{\text{delayed}} \leq Z_{\text{BH}}^{\text{thr}} \leq Z_{\text{BH}}^{\text{prompt}}, \quad (6.17)$$

to hold for the quantities considered in connection with the disk and the BH mass, i.e., $Z_{\text{disk}} \in \{M_{\text{disk}}, Q_{\text{disk}}\}$ and $Z_{\text{BH}} \in \{M_{\text{BH}}, Q_{\text{BH}}\}$. In each case given by mass ratio and EOS, we find a lower estimate of the disk mass at threshold, $Z_{\text{disk}}^{\text{thr}}$, employing the maximal disk-mass value of the prompt-collapse regime. In the case of the BH mass, we find an upper estimate of $Z_{\text{BH}}^{\text{thr}}$ employing the minimal value found within the prompt-collapse regime. We use these lower and upper estimates to approximate

M_{disk} and M_{BH} at threshold. Alternatively, we could try to interpolate. However, this approach would rely on less certain data as the physical and numerical situation are more complicated in the case of delayed-collapse mergers. The longer the HMNS remnant withstands collapse, the more shocks have to be simulated, and the more matter is ejected. To support this argument with an example, we point to the SLy configuration with $q = 1.25$ and $M = 2.8 M_{\odot}$. Simulated with resolution R4 and R2, the merger of this binary produced a remnant HMNS which collapsed after about 2.5 ms. In the case of resolution R3 on the other hand, the remnant survived for more than 15 ms, accumulating about 2.7 times the amount of matter in the disk. Uncertainties are notably smaller in the case of prompt-collapse mergers. Furthermore, this approach would fail in a few cases due to the lack of delayed-collapse data.

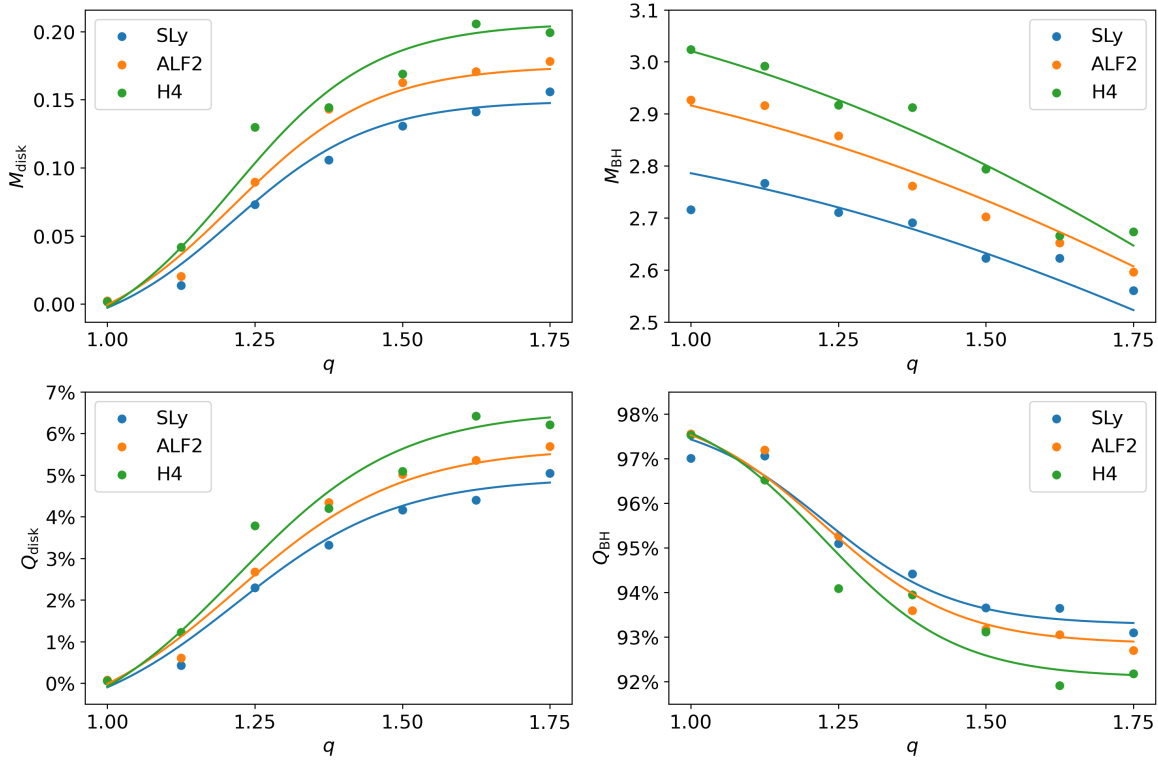


Figure 6.9: First column: Fits of the disk-mass estimates, M_{disk} , and mass ratio Q_{disk} , close to threshold. The fit formula given in Eq. (6.18) depends on the pair of stellar parameters: $(X, Y) = (M_{\text{max}}, \Lambda_{1.4})$. Data points: maximum value of M_{disk} (upper panel) and Q_{disk} (lower panel) for given EOS and mass ratio for the case of prompt collapse.

Second column: Fits of the BH-mass estimates, M_{BH} , and mass ratio, Q_{BH} , close to threshold. The fit formulae given in Eqs. (6.19) and (6.20) depend on a pair of stellar parameters: $(X, Y) = (M_{\text{max}}, \Lambda_{1.4})$. Data points: minimum values of M_{BH} (upper panel) and Q_{BH} (lower panel) for given EOS and mass ratio for the case of prompt collapse. Plots taken from Ref. [Koe1].

Employing empirically motivated fit functions introduced in Ref. [Koe1], we model the relation between the mass ratio and the estimated quantities at threshold.

$$Z_{\text{disk}}^{\text{thr}} = A \cdot \{1.0 + \tanh [M_{\text{max}} (c_3 + c_4 q)] + c_5 M_{\text{max}}\}, \quad (6.18)$$

$$M_{\text{BH}}^{\text{thr}} = A \cdot \{2.5 - c_3 \tanh [M_{\text{max}} (c_4 + c_5 q)] - c_6 \Lambda_{1.4}\}, \quad (6.19)$$

$$Q_{\text{BH}}^{\text{thr}} = A \cdot \{1.0 + c_3 \tanh [M_{\text{max}} (c_4 + c_5 q)] - c_6 \Lambda_{1.4}\}, \quad (6.20)$$

$$A = (c_1 M_{\text{max}} + c_2 \Lambda_{1.4}).$$

The respective fits are presented in Fig. 6.9, and coefficients are reported in Tabs. 6.5 and 6.6. These fits provide approximate lower and upper limits of M_{disk} and M_{BH} in the case of prompt collapse, i.e.,

$$Z_{\text{disk}}^{\text{delayed}} \gtrsim Z_{\text{disk}}^{\text{thr}}(q) \gtrsim Z_{\text{disk}}^{\text{prompt}}, \quad (6.21)$$

$$Z_{\text{BH}}^{\text{delayed}} \lesssim Z_{\text{BH}}^{\text{thr}}(q) \lesssim Z_{\text{BH}}^{\text{prompt}}. \quad (6.22)$$

Regarding the impact of the studied EOSs on the disk mass, we find the same ordering at threshold that we saw in the general case presented in Fig. 6.8, i.e., the smallest upper limit to M_{disk} in the prompt-collapse case is connected to the softest EOS (SLy), the highest limit to the stiffest EOS (H4). In the case of Q_{BH} , we find corresponding inverse relation. However, considering the BH mass itself, we find the same ordering as for the disk mass, i.e., smallest lower limit to M_{BH} is related to the the softest EOS (SLy), the highest lower limit to M_{BH} is related to the the stiffest EOS (H4). This is in no way a contradiction. Considering our results for M_{thr} , cf. for example Fig. 6.1, we find the effect of the EOS on the absolute value of the threshold mass to be stronger than the one on the ratio Q_{BH} .

Picking up the discussion of ejection mechanisms, we interpret the data presented in the first column of Fig. 6.9. In the case of prompt collapse ejection mechanisms except for tidal effects at the onset of merger are suppressed. Therefore, column one of Fig. 6.9 displays once more, how the tidal effects are affected by the mass ratio. The upper limit to M_{disk} in the prompt-collapse case strongly increases at intermediate mass ratios before the incline becomes weaker at high mass ratios.

Table 6.5: Fits describing the estimates for the behaviour of the disk mass close to the threshold to prompt collapse. For each EOS and mass ratio, the disk mass at threshold is approximated by the maximal disk mass value for the case of prompt-collapse mergers. The fit formula given below depends on a pair of stellar parameters: $(X, Y) = (M_{\max}, \Lambda_{1.4})$. We present the following measures of variation: the maximal relative residual (max.), the mean absolute residual (av.), and the coefficient of determination (R^2). Table adapted from Ref. [Koe1].

$Z_{\text{disk}}^{\text{thr}} = A \cdot \{1 + \tanh [M_{\max} (q c_3 + c_4)] + c_5 M_{\max}\}$								
$Z_{\text{disk}}^{\text{thr}}$	c_1	$c_2/10^{-5}$	c_3	c_4	c_5	max.	av.	R^2
$M_{\text{disk}}^{\text{thr}}$	0.034 ± 0.005	5.968 ± 1.141	2.064 ± 0.43	-0.439 ± 0.146	-0.151 ± 0.09	0.0264	0.0078	0.978
$Q_{\text{disk}}^{\text{thr}}$	0.012 ± 0.002	1.749 ± 0.391	1.782 ± 0.406	-0.389 ± 0.149	-0.179 ± 0.101	0.0078	0.0025	0.978

Table 6.6: Fits describing the estimates for the behaviour of the remnant BH mass close to the threshold to prompt collapse. For each EOS and mass ratio, the BH mass at threshold is approximated by the minimal BH-mass value for the case of prompt-collapse mergers. The fit formula given below depends on a pair of stellar parameters: $(X, Y) = (M_{\max}, \Lambda_{1.4})$. We present the following measures of variation: the maximal relative residual (max.), the mean absolute residual (av.), and the coefficient of determination (R^2). Table adapted from Ref. [Koe1].

Fit formula given in $\begin{cases} \text{Eq. (6.19), } Z_{\text{BH}} = M_{\text{BH}} \\ \text{Eq. (6.20), } Z_{\text{BH}} = Q_{\text{BH}} \end{cases}$									
$Z_{\text{BH}}^{\text{thr}}$	c_1	$c_2/10^{-4}$	c_3	c_4	c_5	$c_6/10^{-4}$	max.	av.	R^2
$M_{\text{BH}}^{\text{thr}}$	0.406 ± 0.278	8.322 ± 3.493	0.5 ± 2.207	0.474 ± 0.428	0.453 ± 1.043	10.58 ± 8.41	0.0696	0.0247	0.948
$Q_{\text{BH}}^{\text{thr}}$	0.432 ± 0.003	6.292 ± 0.309	0.022 ± 0.003	-0.491 ± 0.189	2.188 ± 0.569	3.786 ± 0.119	0.0076	0.0026	0.965

Chapter 7

Conclusion

Summary

In this thesis, we investigated the effect of mass ratio on BNS mergers, paying special attention to the threshold to prompt collapse, properties of the remnant system, and the collapse time. In connection with the development of a method to determine the threshold mass to prompt collapse by means of interpolation instead of bracketing, we have thoroughly discussed related definitions and methods.

These investigations are based on a large set of simulations. Employing the BAM code, we performed 335 fully relativistic simulations, considering 165 configurations of non-rotating BNSs of varying M , q and EOS. The studied parameter space is spanned by seven mass ratios in the range of $q = 1.0$ to $q = 1.75$. Seeking to include both prompt-collapse and delayed-collapse mergers in each of the 21 cases defined by pairs of an EOS and a mass ratio, we considered customized ranges of total masses for each of the 3 employed EOSs. This simulation campaign consists of two subsets: A main set of 295 simulations exploring mass-ratio effects, and a subset of 40 simulations further resolving a single case in the close vicinity of the threshold to prompt collapse which revealed a steep behaviour of the collapse-time curve close to threshold. The analysis of this large number of simulations required automated processing of the simulation output. For this purpose, we developed a workframe tailored specifically for the task of processing data and results of this simulation campaign.

A BNS merger remnant that cannot be stabilized against its own gravitational pull will collapse to a BH. In the case of a binary with comparable properties (mass ratio, spin, ...), but lower total mass, this fate may be delayed due to its thermal pressure and rapid differential rotation. Considering BNS merger simulations, the cases of prompt and delayed collapse are distinguished based on criteria that take into account the number of minima (maxima) of the minimum-lapse function (the

maximum-density function). The application of these criteria to a set of simulations allows us to confine the threshold mass M_{thr} by application of the bracketing method. We have motivated and developed an alternative method based on a fit of collapse-time data. Seeking to establish a quantitative criterion which does not involve the counting of minima/maxima, we have evaluated all of our simulations based on the lapse/density criterion, finding that the collapse time provides suitable qualities. These qualities allow us to define a threshold collapse time that is uniquely related to threshold mass in the sense that collapse times smaller than τ_{thr} imply prompt collapse, and delayed collapse in the complementary case. In this context, the steep behaviour of the collapse-time curve close to threshold implies an insensitive dependence of M_{thr} on the precise definition of τ_{thr} . Employing an empirically motivated fit of collapse time data, we localised the threshold mass by means of interpolation. Deviating from the path taken in other approaches, we did not seek to decrease the interval confining M_{thr} by each additional simulation. Instead, we considered a broad range of total masses. Using the example case of the smaller subset of simulations as a test bed, we gave a critical look at our method, comparing it to the bracketing method and the so called free-fall method by Köppel et al., 2019. Advantages of our method are the use of more than one numerical resolution for error estimates and the broader investigated mass interval. Methods that are based on data close to threshold on the other hand have the advantage of being more reliable.

Analysing our threshold-mass data, we found the dependence of M_{thr} on the mass-ratio to be non-monotonous with a maximum at intermediate q . At high q , the threshold mass tends to decrease. This finding stands in contrast to a model by Bauswein et al., 2021, which is based on a smaller interval of mass ratios and distinguishes between the cases of monotonously increasing or decreasing M_{thr} . To allow for maxima in this model, we have added two terms to the fit function by Bauswein et al., 2021. Employing this extended model, we fit our data and combined data sets, using data by Bauswein et al., 2021, and Perego et al., 2021. In doing so, we compensated for the small number of EOSs considered in our study.

Based on our M_{thr} data, we determined tidal properties of threshold configurations. Modelling the effect of mass ratio on tidal polarizabilities of threshold configurations, we have improved an existing model found by Bernuzzi, 2020, which gives constant upper limits to tidal parameters of prompt-collapse mergers. In our model these constant upper limits are replaced with fits that depend on the mass ratio and the EOS. In the case of our small set of EOSs, we have found the dependence of tidal

parameters at threshold to be properly described by polynomials quadratic in q , with a linear dependence on $\Lambda_{1.4}$. Comparing our finding to results by Kashyap et al., 2021, who considered a broader set of 21 EOSs in the case of $q = 1$, we found this linear dependence of our model on a single stellar parameter to match some, but not all of their data. This indicates a dependence on more than one stellar parameter which cannot be inferred from our data.

Properties of the remnant system depend on dynamics at merger, especially in the case of prompt-collapse mergers. In the case of HMNSs, the final BH + disk system is also affected by the post-merger evolution. Mass-ratio effects at merger arise in the context of tidal distortions or even the tidal disruption of the lower-mass companion. Over the range of studied mass ratios, we have found increasing tidal effects on the secondary component. Considering the case of prompt-collapse mergers, we have also found the amount of matter accumulated in a disk around the remnant BH to increase with q . As no further matter is ejected once a BH is formed, disk mass and tidal effects have to be directly related in the case of prompt collapse. In the case of HMNSs, i.e., in the case of smaller total masses and increasing collapse times, other mechanisms continuously cause the ejection of matter until the NS remnant collapses to a BH. As it is to be expected, we have found the opposite relations regarding mass and spin of the remnant BH. Similarly to the case of tidal properties, we modelled threshold quantities of disk mass and BH mass, approximated by data from the prompt-collapse regime.

Future Prospects

Different approaches may be taken to extend or improve the investigations conducted in this thesis.

- Considering our investigation of methods to determine M_{thr} based on collapse-time fits, we propose to make further efforts to find a fit of data with $M \approx M_{\text{thr}}$ that allows determine M_{thr} with high precision, taking into account different numerical resolutions, while being economic with respect to the number of required data points and computational resources.
- Regarding the definition of a threshold collapse time in the context of methods to determine M_{thr} by means of interpolation, the validity of τ_{thr} with respect to a larger sample of EOSs should be tested.

- In favour of a broad range of investigated mass ratios, we have investigated only three EOSs. In future investigations, computational resources may be applied to extension the parameter space with respect to the number of considered EOSs. A higher number of EOSs would especially be interesting in the case of our models of tidal parameters at threshold.
- In the present work, we considered exclusively irrotational stars. As shown by the work of Tootle et al., 2021, NS spin affects merger dynamics and therefore the threshold mass to prompt collapse. Similarly we expect effects on properties of remnant system.
- Different microphysical aspects have been ignored in the simulations conducted for this work as their implementations in the BAM code is still pending, e.g. magnetic fields and neutrino transport.

With respect to the large number of GW events expected to be observed in connection with BNS mergers, general relativistic simulations will play a crucial role in the effort to determine the NS EOS. Multi-messenger observations of these events will allow to further constraint the threshold mass to prompt collapse. The classification of these observations in terms of prompt and delayed collapse will profit from an understanding of mass-ratio effects on M_{thr} and on the amount of ejected material that can power postmerger signals.

Appendix A

Waveforms, Minimum-Lapse, Maximum-Density

In this appendix, we present waveforms, minimum-lapse functions and maximum-density functions of a subset of our simulations conducted with resolution R3. For each EOS, plots are ordered with respect to mass ratio (columns) and total mass (rows), the time axis is shifted with respect to the time of merger. In each figure the presented time interval is the same over all columns. In each panel showing data of a BNS merger whose remnant collapsed to a BH within simulation time, the times of merger and BH formation are marked, and the collapse time is given. In a small number of cases characterized by large collapse times, the time of BH formation is not within the presented interval. Based on the number of minima in the minimum-lapse function or the number of maxima in the maximum-density function, BNS mergers can be categorized in terms of prompt and delayed collapse, cf. Sect. 4.3.2.

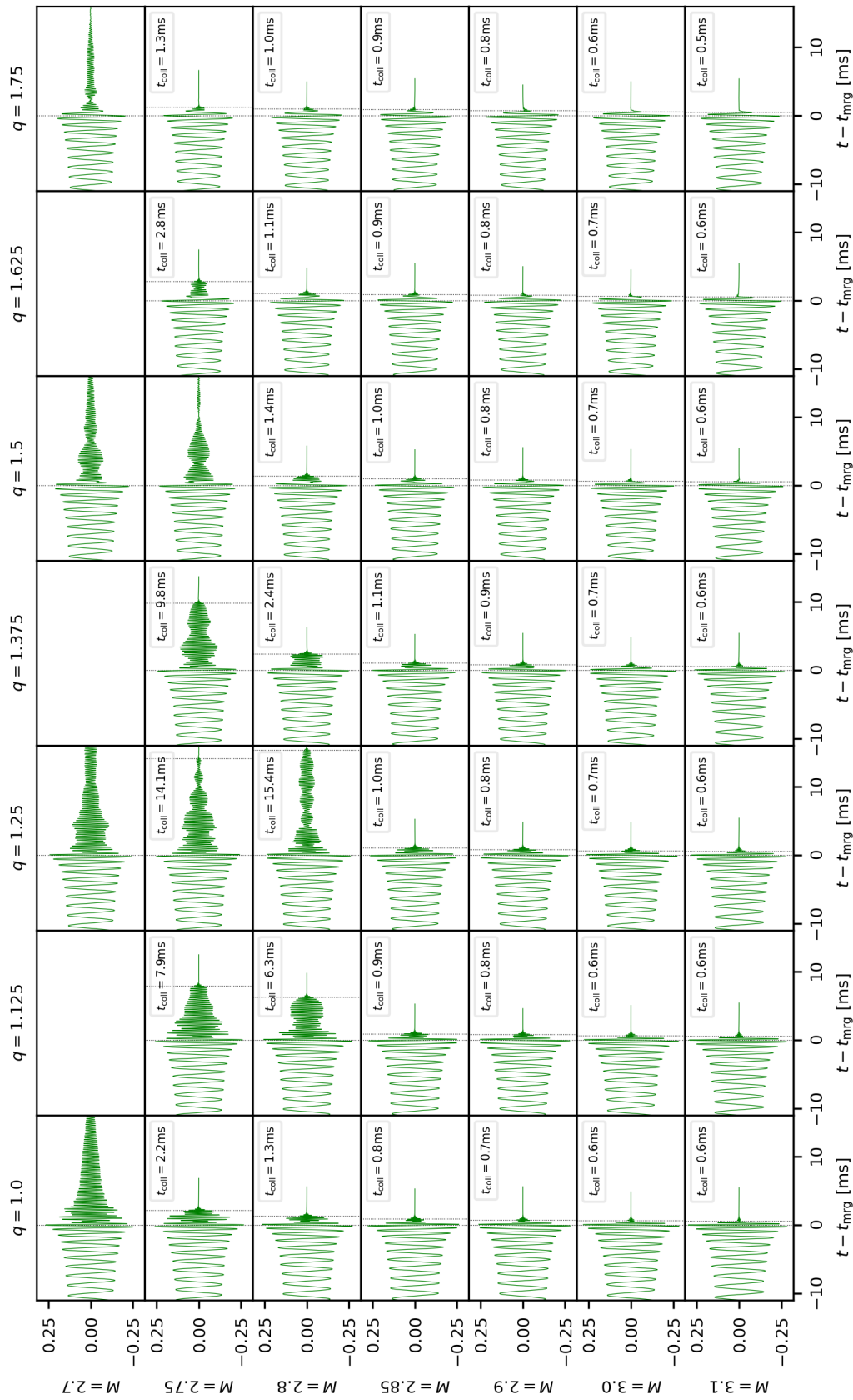


Figure A.1: GW strain (22-mode) and collapse times; Vertical dotted lines mark t_{mrg} and t_{AH} ; EOS SLy.

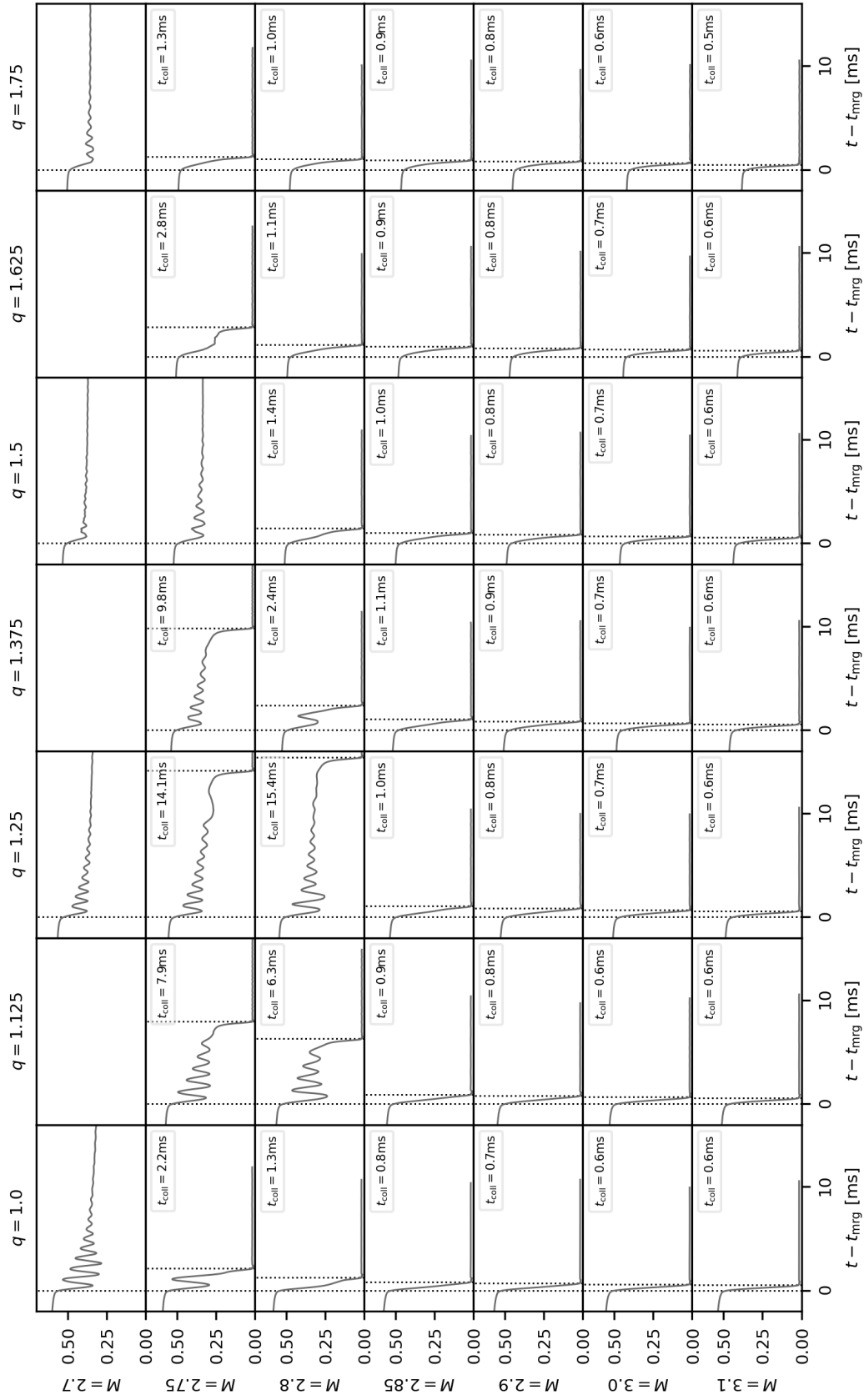


Figure A.2: Minimum-lapse as a function of time; Vertical dotted lines mark t_{mrg} and t_{AH} ; EOS SLy.

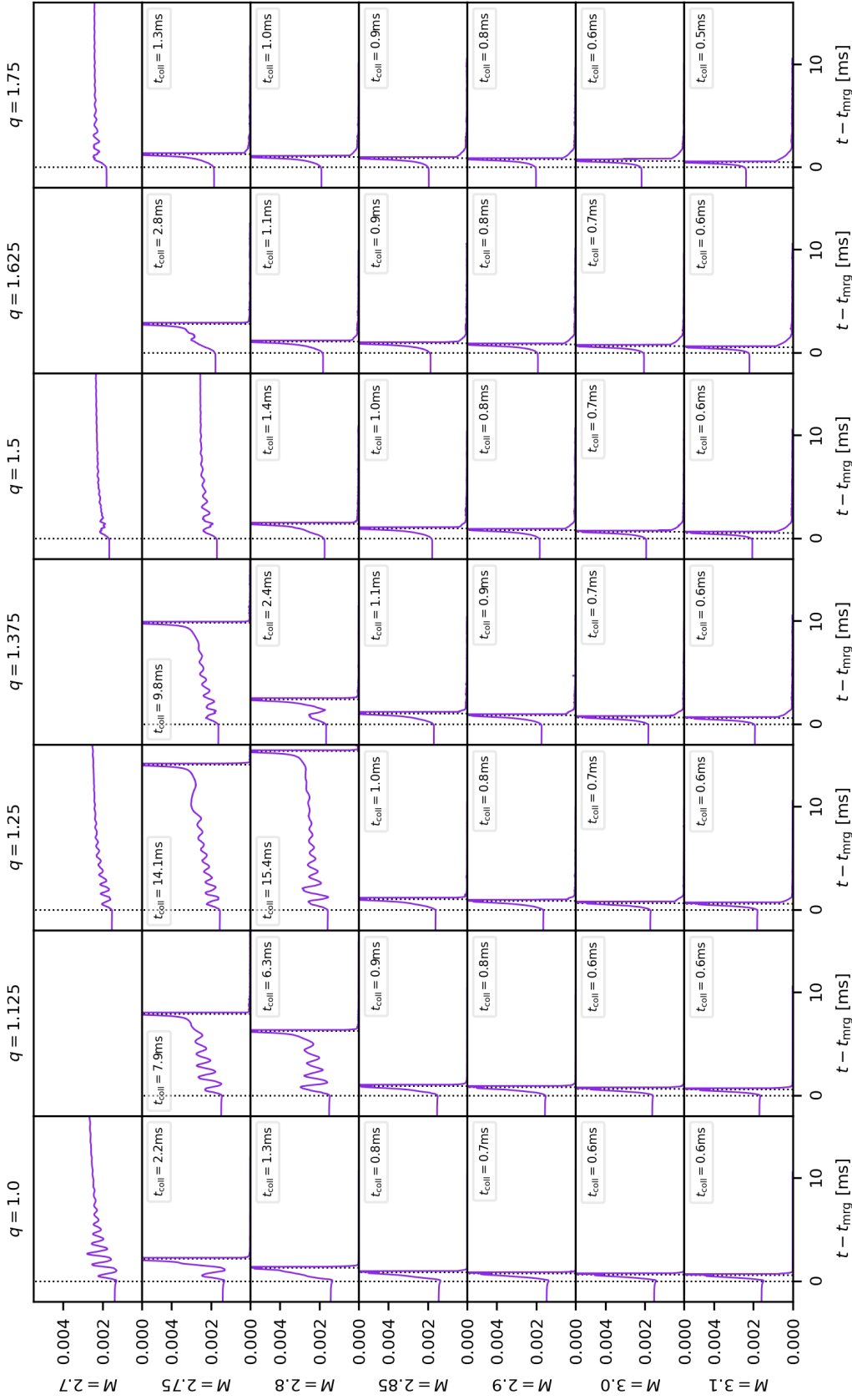


Figure A.3: Maximum-density as a function of time; Vertical dotted lines mark t_{mrg} and t_{AH} ;
EOS SLy.

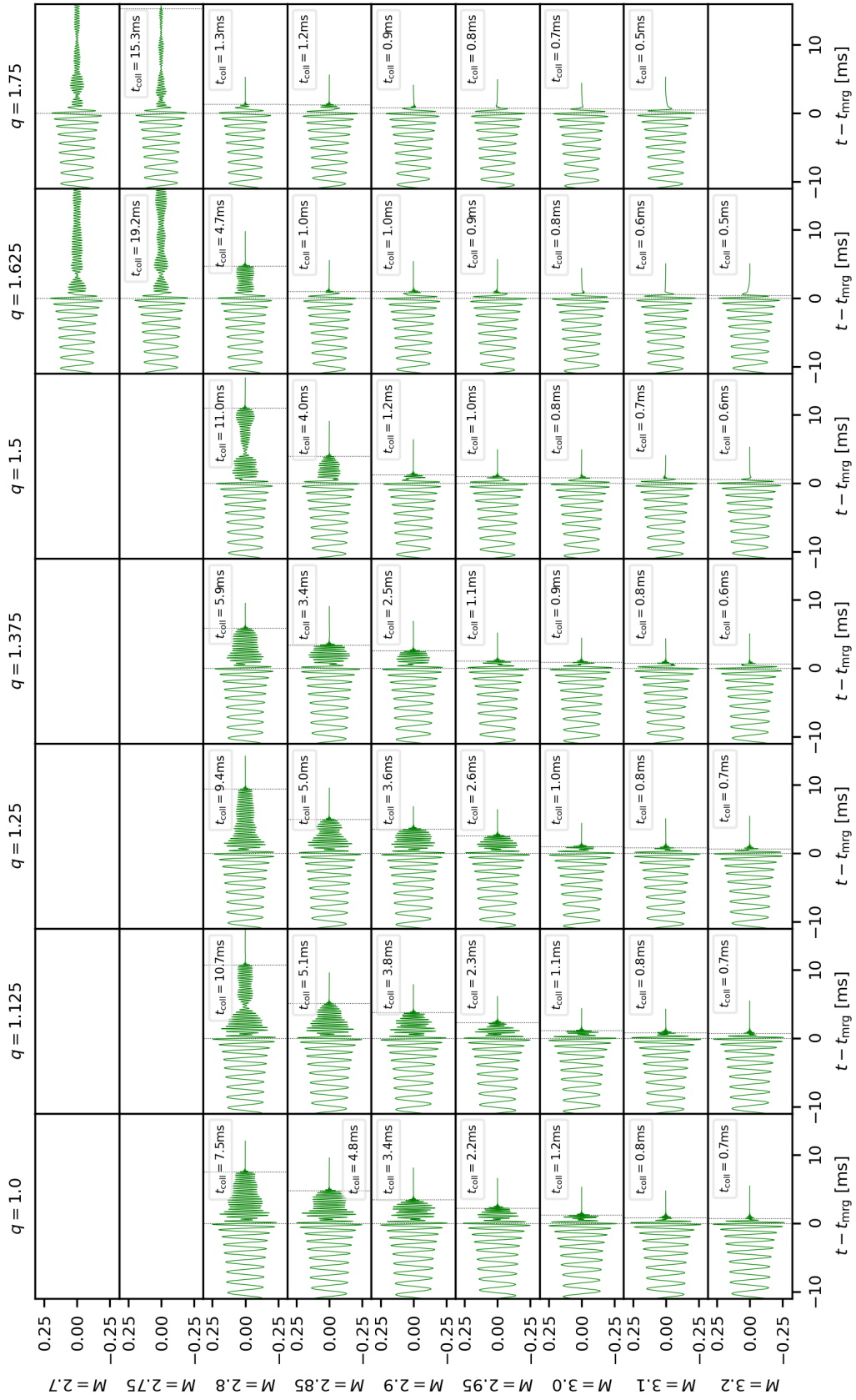


Figure A.4: Same as Fig. A.1, but for ALF2

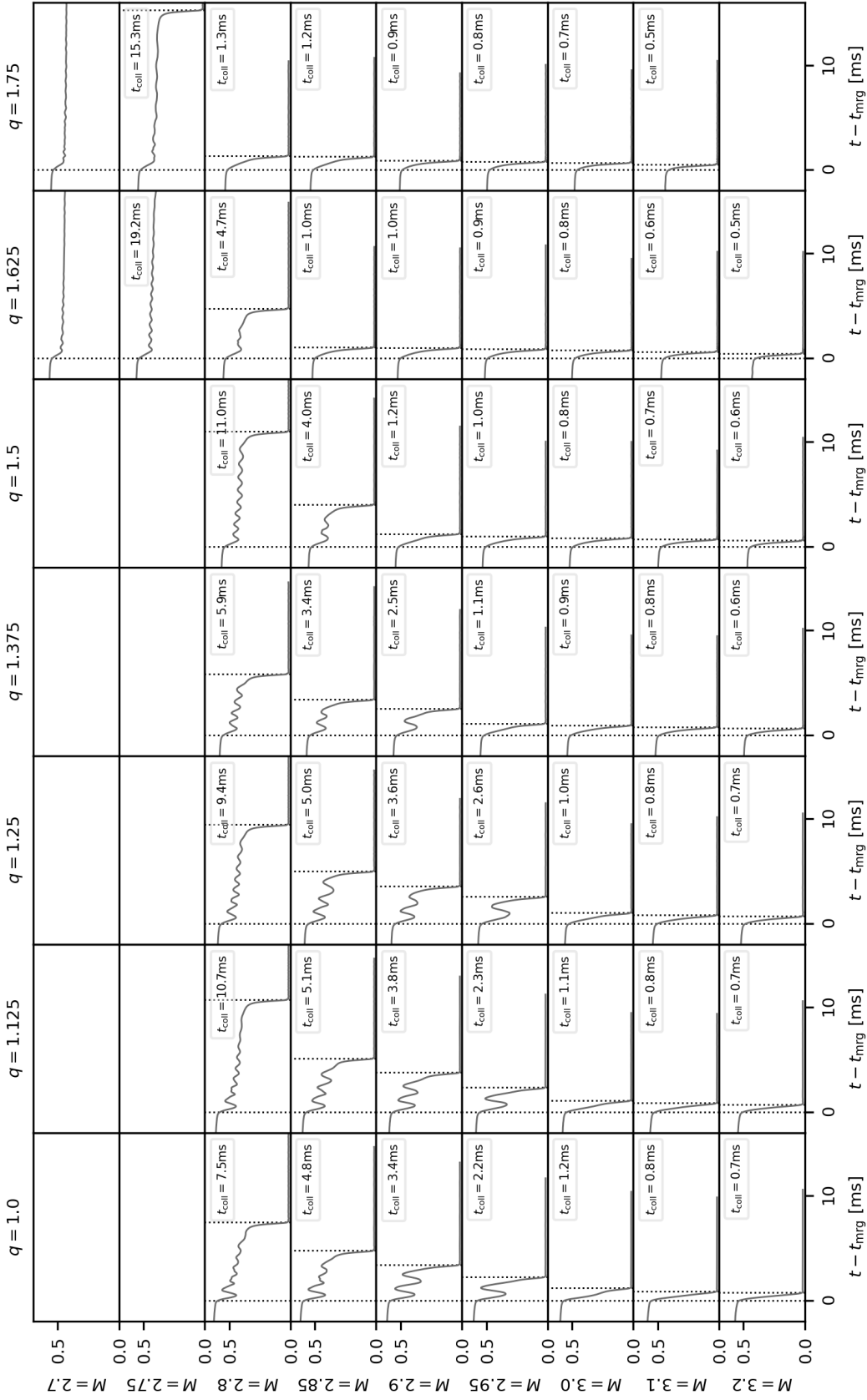


Figure A.5: Same as Fig. A.2, but for ALF2.

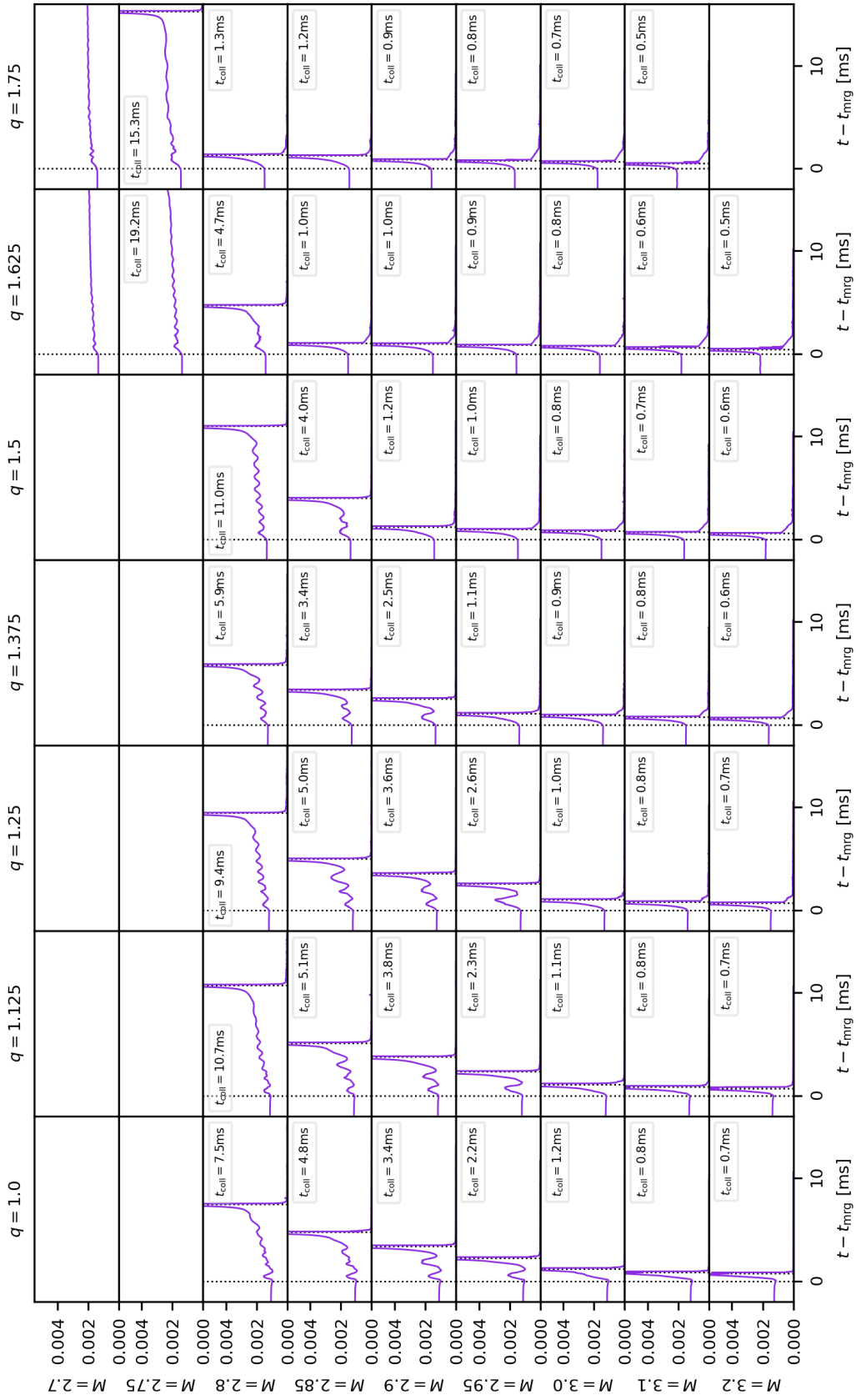


Figure A.6: Same as Fig. A.3, but for ALF2.

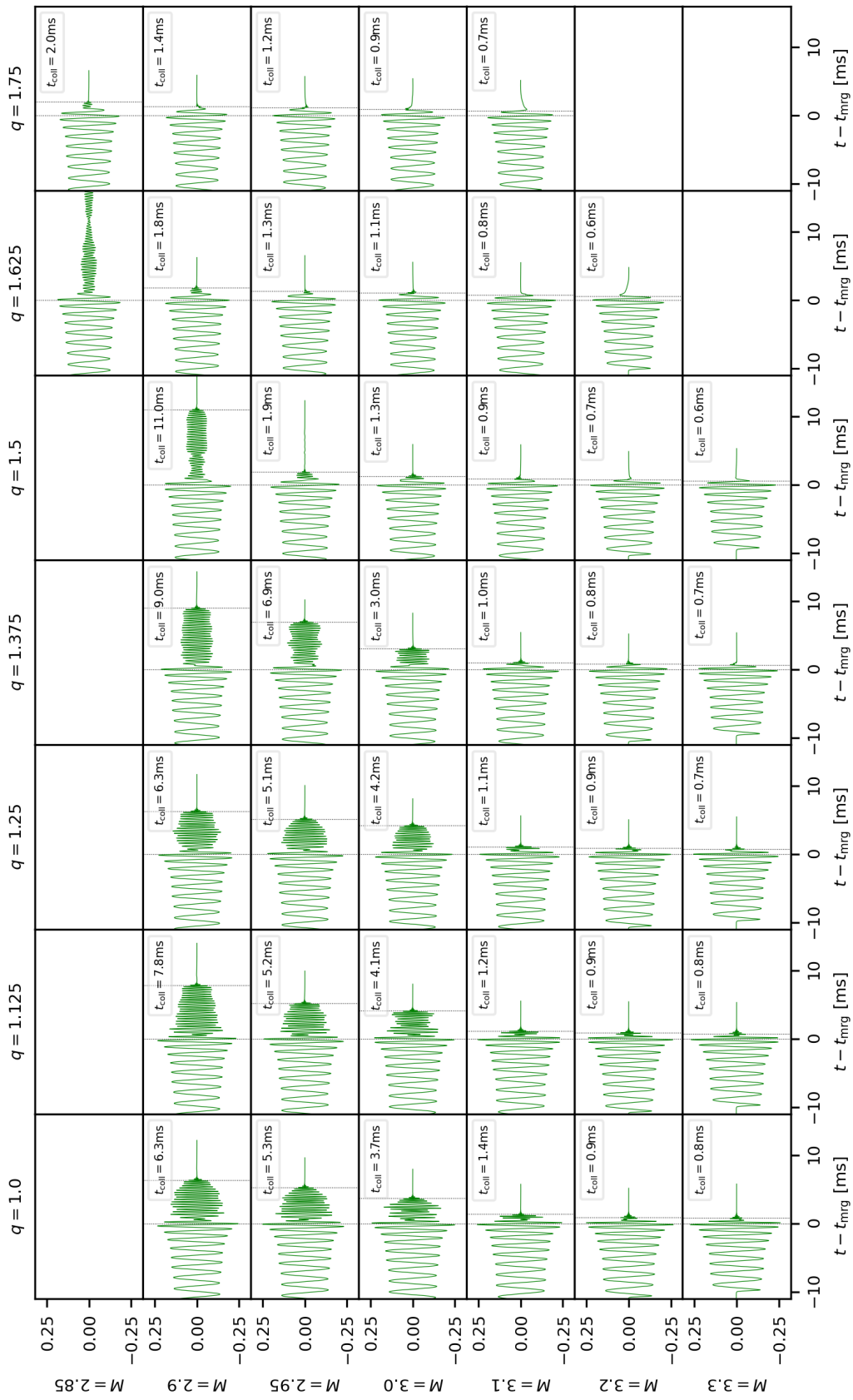


Figure A.7: Same as Fig. A.1, but for H4

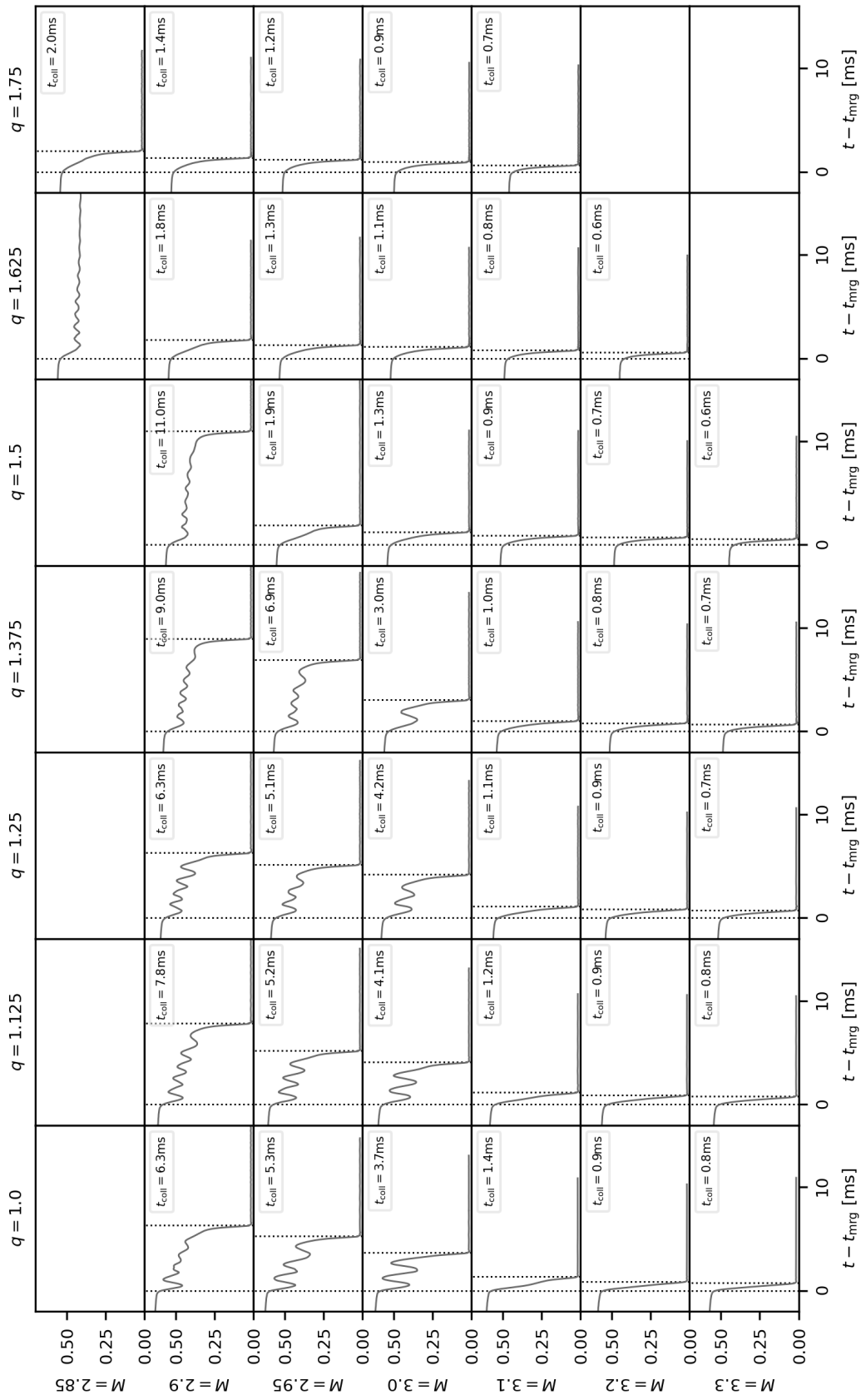


Figure A.8: Same as Fig. A.2, but for H4.

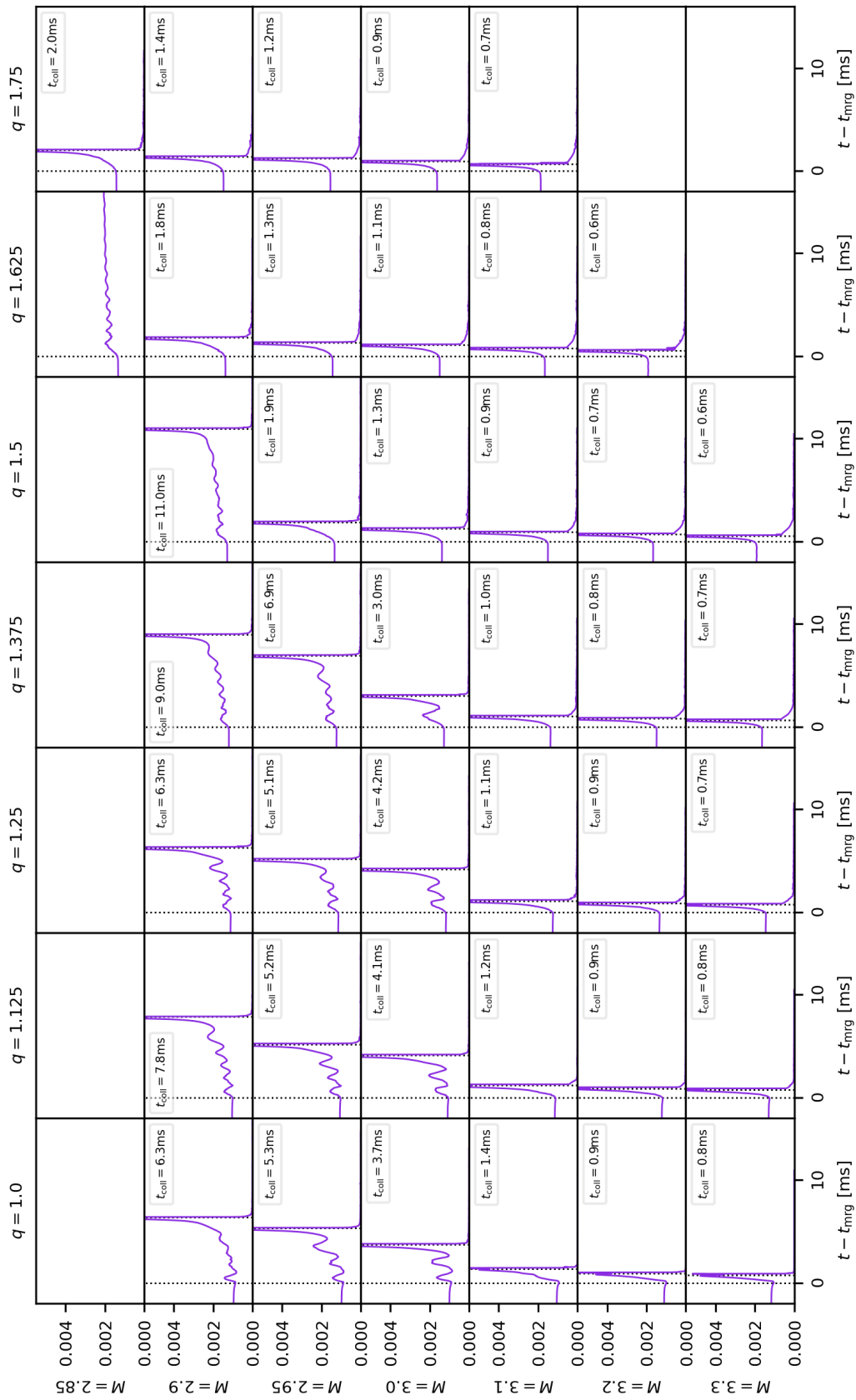


Figure A.9: Same as Fig. A.3, but for H4.

Appendix B

Stellar Parameters

For fits of combined data sets, we have used data of Perego et al., 2021. These fits depend on stellar parameters, which we list in Tab. B.1 for EOSs employed by Perego et al., 2021 and in Ref. [Koe1], respectively.

Table B.1: Columns two to four: Stellar parameters M_{\max} , $R_{1.6}$, R_{\max} and $\lambda_{1.4}$ of EOSs used in the studies, Perego et al., 2021, (P), and [Koe1], (K). Column five: Threshold masses of equal-mass binaries, $\hat{M}_{\text{thr}}(q = 1)$, as determined by simulations in the respective works indicated in the last column.

EOS	M_{\max}	$R_{1.6}$	R_{\max}	$\lambda_{1.4}$	$\hat{M}_{\text{thr}}(q = 1)$	Ref.
H4	2.03	13.46	11.62	886	3.057	K
DD2	2.42	13.27	11.90	769	3.274	P
BHB	2.10	13.21	11.59	754	3.024	P
DD2qG	2.15	13.29	12.53	690	3.152	P
ALF2	1.99	12.41	11.30	591	2.963	K
LS220	2.04	12.50	10.65	547	2.956	P
BLh	2.10	12.24	10.50	430	2.924	P
SFH _o	2.05	11.77	10.32	333	2.824	P
SLy	2.06	11.37	9.91	307	2.756	K

Bibliography

- ABBOTT, B.P. et al., 2020a. GW190425: Observation of a Compact Binary Coalescence with Total Mass $\sim 3.4M_{\odot}$. *Astrophys. J. Lett.* Vol. 892, p. L3. Available from DOI: 10.3847/2041-8213/ab75f5.
- AGATHOS, Michalis et al., 2020. Inferring Prompt Black-Hole Formation in Neutron Star Mergers from Gravitational-Wave Data. *Phys. Rev. D.* Vol. 101, no. 4, p. 044006. Available from DOI: 10.1103/PhysRevD.101.044006.
- ALFORD, Mark et al., 2005. Hybrid stars that masquerade as neutron stars. *Astrophys. J.* Vol. 629, pp. 969–978. Available from DOI: 10.1086/430902.
- ANNALA, Eemeli et al., 2018. Gravitational-wave constraints on the neutron-star-matter Equation of State. *Phys. Rev. Lett.* Vol. 120, no. 17, p. 172703. Available from DOI: 10.1103/PhysRevLett.120.172703.
- ANTONIADIS, John et al., 2013. A Massive Pulsar in a Compact Relativistic Binary. *Science.* Vol. 340, p. 6131. Available from DOI: 10.1126/science.1233232.
- ARNOWITT, Richard L. et al., 2008. The Dynamics of general relativity. *Gen. Rel. Grav.* Vol. 40, pp. 1997–2027. Available from DOI: 10.1007/s10714-008-0661-1.
- BAIOTTI, Luca et al., 2017. Binary neutron star mergers: a review of Einstein’s richest laboratory. *Rept. Prog. Phys.* Vol. 80, no. 9, p. 096901. Available from DOI: 10.1088/1361-6633/aa67bb.
- BAKER, John G. et al., 2002. The Lazarus project: A Pragmatic approach to binary black hole evolutions. *Phys. Rev. D.* Vol. 65, p. 044001. Available from DOI: 10.1103/PhysRevD.65.044001.
- BAKER, John G. et al., 2006b. Gravitational wave extraction from an inspiraling configuration of merging black holes. *Phys. Rev. Lett.* Vol. 96, p. 111102. Available from DOI: 10.1103/PhysRevLett.96.111102.
- BAKER, John G. et al., 2006a. Binary black hole merger dynamics and waveforms. *Phys. Rev. D.* Vol. 73, p. 104002. Available from DOI: 10.1103/PhysRevD.73.104002.

- BARACK, Leor et al., 2019. Black holes, gravitational waves and fundamental physics: a roadmap. *Class. Quant. Grav.* Vol. 36, no. 14, p. 143001. Available from DOI: 10.1088/1361-6382/ab0587.
- BAUMGARTE, Thomas W. et al., 1998. On the numerical integration of Einstein's field equations. *Phys. Rev. D.* Vol. 59, p. 024007. Available from DOI: 10.1103/PhysRevD.59.024007.
- BAUMGARTE, Thomas W. et al., 2010. *Numerical Relativity: Solving Einstein's Equations on the Computer*. Cambridge University Press. Available from DOI: 10.1017/CB09781139193344.
- BAUSWEIN, A. et al., 2010. Testing Approximations of Thermal Effects in Neutron Star Merger Simulations. *Phys.Rev.* Vol. D82, p. 084043. Available from DOI: 10.1103/PhysRevD.82.084043.
- BAUSWEIN, A. et al., 2013. Prompt merger collapse and the maximum mass of neutron stars. *Phys.Rev.Lett.* Vol. 111, no. 13, p. 131101. Available from DOI: 10.1103/PhysRevLett.111.131101.
- BAUSWEIN, Andreas et al., 2017. Neutron-star radius constraints from GW170817 and future detections. *Astrophys. J. Lett.* Vol. 850, no. 2, p. L34. Available from DOI: 10.3847/2041-8213/aa9994.
- BAUSWEIN, Andreas et al., 2021. Systematics of prompt black-hole formation in neutron star mergers. *Phys. Rev. D.* Vol. 103, no. 12, p. 123004. Available from DOI: 10.1103/PhysRevD.103.123004.
- BERNUZZI, Sebastiano et al., 2008. Gravitational waves from pulsations of neutron stars described by realistic Equations of State. *Phys. Rev.* Vol. D78, p. 024024. Available from DOI: 10.1103/PhysRevD.78.024024.
- BERNUZZI, Sebastiano et al., 2010. Constraint violation in free evolution schemes: comparing BSSNOK with a conformal decomposition of Z4. *Phys. Rev.* Vol. D81, p. 084003. Available from DOI: 10.1103/PhysRevD.81.084003.
- BERNUZZI, Sebastiano et al., 2014. Mergers of binary neutron stars with realistic spin. *Phys. Rev. D.* Vol. 89, no. 10, p. 104021. Available from DOI: 10.1103/PhysRevD.89.104021.
- BERNUZZI, Sebastiano et al., 2016b. How loud are neutron star mergers? *Phys. Rev. D.* Vol. 94, no. 2, p. 024023. Available from DOI: 10.1103/PhysRevD.94.024023.

- BERNUZZI, Sebastiano et al., 2016a. Gravitational waveforms from binary neutron star mergers with high-order weighted-essentially-nonscillatory schemes in numerical relativity. *Phys. Rev.* Vol. D94, no. 6, p. 064062. Available from DOI: 10.1103/PhysRevD.94.064062.
- BERNUZZI, Sebastiano, 2020. Neutron Star Merger Remnants. *Gen. Rel. Grav.* Vol. 52, no. 11, p. 108. Available from DOI: 10.1007/s10714-020-02752-5.
- BERNUZZI, Sebastiano et al., 2020. Accretion-induced prompt black hole formation in asymmetric neutron star mergers, dynamical ejecta and kilonova signals. *Mon. Not. Roy. Astron. Soc.* Vol. 497, no. 2, pp. 1488–1507. Available from DOI: 10.1093/mnras/staa1860.
- BISHOP, Nigel T. et al., 2016. Extraction of Gravitational Waves in Numerical Relativity. *Living Rev. Rel.* Vol. 19, p. 2. Available from DOI: 10.1007/s41114-016-0001-9.
- BLANCHET, Luc, 2014. Gravitational Radiation from Post-Newtonian Sources and Inspiralling Compact Binaries. *Living Rev. Rel.* Vol. 17, p. 2. Available from DOI: 10.12942/lrr-2014-2.
- BORGES, Rafael et al., 2008. An improved weighted essentially non-oscillatory scheme for hyperbolic conservation laws. *Journal of Computational Physics.* Vol. 227, no. 6, pp. 3191–3211. ISSN 0021-9991. Available from DOI: 10.1016/j.jcp.2007.11.038.
- BRÜGMANN, Bernd et al., 2008. Calibration of Moving Puncture Simulations. *Phys. Rev.* Vol. D77, p. 024027. Available from DOI: 10.1103/PhysRevD.77.024027.
- BUCHDAHL, Hans A., 1959. General Relativistic Fluid Spheres. *Phys. Rev.* Vol. 116, p. 1027. Available from DOI: 10.1103/PhysRev.116.1027.
- CAMPANELLI, Manuela et al., 2006. Accurate evolutions of orbiting black-hole binaries without excision. *Phys. Rev. Lett.* Vol. 96, p. 111101. Available from DOI: 10.1103/PhysRevLett.96.111101.
- CAPANO, Collin D. et al., 2020. Stringent constraints on neutron-star radii from multimessenger observations and nuclear theory. *Nature Astron.* Vol. 4, no. 6, pp. 625–632. Available from DOI: 10.1038/s41550-020-1014-6.
- CARROLL, Sean M., 2019. *Spacetime and Geometry*. Cambridge University Press. ISBN 978-0-8053-8732-2, ISBN 978-1-108-48839-6, ISBN 978-1-108-77555-7.

- CENTRELLA, Joan et al., 2010. Black-hole binaries, gravitational waves, and numerical relativity. *Rev. Mod. Phys.* Vol. 82, p. 3069. Available from DOI: 10.1103/RevModPhys.82.3069.
- COUGHLIN, Michael W. et al., 2019. Multimessenger Bayesian parameter inference of a binary neutron star merger. *Mon. Not. Roy. Astron. Soc.* Vol. 489, no. 1, pp. L91–L96. Available from DOI: 10.1093/mnras1/slz133.
- COUGHLIN, Michael W. et al., 2018. Constraints on the neutron star equation of state from AT2017gfo using radiative transfer simulations. *Mon. Not. Roy. Astron. Soc.* Vol. 480, no. 3, pp. 3871–3878. Available from DOI: 10.1093/mnras/sty2174.
- COUGHLIN, Michael W. et al., 2020. Implications of the search for optical counterparts during the first six months of the Advanced LIGO’s and Advanced Virgo’s third observing run: possible limits on the ejecta mass and binary properties. *Mon. Not. Roy. Astron. Soc.* Vol. 492, no. 1, pp. 863–876. Available from DOI: 10.1093/mnras/stz3457.
- DAMOUR, Thibault et al., 2009. Relativistic tidal properties of neutron stars. *Phys. Rev. D.* Vol. 80, p. 084035. Available from DOI: 10.1103/PhysRevD.80.084035.
- DAMOUR, Thibault et al., 2010. Effective One Body description of tidal effects in inspiralling compact binaries. *Phys. Rev. D.* Vol. 81, p. 084016. Available from DOI: 10.1103/PhysRevD.81.084016.
- DANIELEWICZ, Pawel et al., 2002. Determination of the equation of state of dense matter. *Science.* Vol. 298, pp. 1592–1596. Available from DOI: 10.1126/science.1078070.
- DIETRICH, Tim et al., 2015b. Numerical relativity simulations of neutron star merger remnants using conservative mesh refinement. *Phys. Rev.* Vol. D91, no. 12, p. 124041. Available from DOI: 10.1103/PhysRevD.91.124041.
- DIETRICH, Tim et al., 2015a. Binary Neutron Stars with Generic Spin, Eccentricity, Mass ratio, and Compactness - Quasi-equilibrium Sequences and First Evolutions. *Phys. Rev.* Vol. D92, no. 12, p. 124007. Available from DOI: 10.1103/PhysRevD.92.124007.
- DIETRICH, Tim et al., 2017. Gravitational waves and mass ejecta from binary neutron star mergers: Effect of the mass-ratio. *Phys. Rev.* Vol. D95, no. 2, p. 024029. Available from DOI: 10.1103/PhysRevD.95.024029.

- DIETRICH, Tim et al., 2018. CoRe database of binary neutron star merger waveforms. *Class. Quant. Grav.* Vol. 35, no. 24, 24LT01. Available from DOI: 10.1088/1361-6382/aaebc0.
- DIETRICH, Tim et al., 2020. Multimessenger constraints on the neutron-star equation of state and the Hubble constant. *Science*. Vol. 370, no. 6523, pp. 1450–1453. Available from DOI: 10.1126/science.abb4317.
- DOUCHIN, F. et al., 2001. A unified equation of state of dense matter and neutron star structure. *Astron. Astrophys.* Vol. 380, p. 151. Available from DOI: 10.1051/0004-6361:20011402.
- DUDI, Reetika et al., 2021. *Investigating GW190425 with numerical-relativity simulations*. Available from arXiv: 2109.04063 [astro-ph.HE].
- EINSTEIN, Albert, 1915b. Zur Allgemeinen Relativitätstheorie. *Sitzungsber. Preuss. Akad. Wiss. Berlin (Math. Phys.)* Vol. 1915, pp. 778–786. [Addendum: *Sitzungsber. Preuss. Akad. Wiss. Berlin (Math. Phys.)* 1915, 799–801 (1915)].
- EINSTEIN, Albert, 1915a. The Field Equations of Gravitation. *Sitzungsber. Preuss. Akad. Wiss. Berlin (Math. Phys.)* Vol. 1915, pp. 844–847.
- EINSTEIN, Albert, 1916. Approximative Integration of the Field Equations of Gravitation. *Sitzungsber. Preuss. Akad. Wiss. Berlin (Math. Phys.)* Vol. 1916, pp. 688–696.
- EINSTEIN, Albert, 1918. Über Gravitationswellen. *Sitzungsber. Preuss. Akad. Wiss. Berlin (Math. Phys.)* Vol. 1918, pp. 154–167.
- FISKE, David R. et al., 2005. Wave zone extraction of gravitational radiation in three-dimensional numerical relativity. *Phys. Rev. D*. Vol. 71, p. 104036. Available from DOI: 10.1103/PhysRevD.71.104036.
- FLANAGAN, Eanna E. et al., 2008. Constraining neutron star tidal Love numbers with gravitational wave detectors. *Phys. Rev. D*. Vol. 77, p. 021502. Available from DOI: 10.1103/PhysRevD.77.021502.
- FONSECA, E. et al., 2021. Refined Mass and Geometric Measurements of the High-mass PSR J0740+6620. *Astrophys. J. Lett.* Vol. 915, no. 1, p. L12. Available from DOI: 10.3847/2041-8213/ac03b8.
- GOURGOULHON, Eric, 2007. 3+1 formalism and bases of numerical relativity. Available from arXiv: gr-qc/0703035.

- HEWISH, A. et al., 1968. Observation of a rapidly pulsating radio source. *Nature*. Vol. 217, pp. 709–713. Available from DOI: 10.1038/217709a0.
- HILDITCH, David et al., 2013. Compact binary evolutions with the Z4c formulation. *Phys. Rev.* Vol. D88, p. 084057. Available from DOI: 10.1103/PhysRevD.88.084057.
- HINDERER, Tanja, 2008. Tidal Love numbers of neutron stars. *Astrophys. J.* Vol. 677, pp. 1216–1220. Available from DOI: 10.1086/533487.
- HOTOKEZAKA, Kenta et al., 2011. Binary Neutron Star Mergers: Dependence on the Nuclear Equation of State. *Phys.Rev.* Vol. D83, p. 124008. Available from DOI: 10.1103/PhysRevD.83.124008.
- HOTOKEZAKA, Kenta et al., 2013. Mass ejection from the merger of binary neutron stars. *Phys. Rev. D.* Vol. 87, p. 024001. Available from DOI: 10.1103/PhysRevD.87.024001.
- HULSE, R. A. et al., 1975. Discovery of a pulsar in a binary system. *Astrophys. J. Lett.* Vol. 195, pp. L51–L53. Available from DOI: 10.1086/181708.
- HUTH, S. et al., 2021. *Constraining Neutron-Star Matter with Microscopic and Macroscopic Collisions*. Available from arXiv: 2107.06229 [nucl-th].
- KASHYAP, Rahul et al., 2021. *Numerical relativity simulations of prompt collapse mergers: threshold mass and phenomenological constraints on neutron star properties after GW170817*. Available from arXiv: 2111.05183 [astro-ph.HE].
- KIDDER, Lawrence E. et al., 2001. Extending the lifetime of 3-D black hole computations with a new hyperbolic system of evolution equations. *Phys. Rev. D.* Vol. 64, p. 064017. Available from DOI: 10.1103/PhysRevD.64.064017.
- KINNERSLEY, William, 1969. Type D Vacuum Metrics. *J. Math. Phys.* Vol. 10, pp. 1195–1203. Available from DOI: 10.1063/1.1664958.
- KÖPPEL, Sven et al., 2019. A General-relativistic Determination of the Threshold Mass to Prompt Collapse in Binary Neutron Star Mergers. *Astrophys. J. Lett.* Vol. 872, no. 1, p. L16. Available from DOI: 10.3847/2041-8213/ab0210.
- KORANDA, Scott et al., 1997. Upper limit set by causality on the rotation and mass of uniformly rotating relativistic stars. *Astrophys. J.* Vol. 488, p. 799. Available from DOI: 10.1086/304714.

- LACKEY, Benjamin D. et al., 2006. Observational constraints on hyperons in neutron stars. *Phys. Rev. D*. Vol. 73, p. 024021. Available from DOI: 10.1103/PhysRevD.73.024021.
- LATTIMER, James M. et al., 2016. The Equation of State of Hot, Dense Matter and Neutron Stars. *Phys. Rept.* Vol. 621, pp. 127–164. Available from DOI: 10.1016/j.physrep.2015.12.005.
- LEGRED, Isaac et al., 2021. *Impact of the PSR J0740+6620 radius constraint on the properties of high-density matter*. Available from arXiv: 2106.05313 [astro-ph.HE].
- ABBOTT, B. P. et al., 2009. LIGO: The Laser interferometer gravitational-wave observatory. *Rept. Prog. Phys.* Vol. 72, p. 076901. Available from DOI: 10.1088/0034-4885/72/7/076901.
- ABBOTT, B. P. et al., 2016. Observation of Gravitational Waves from a Binary Black Hole Merger. *Phys. Rev. Lett.* Vol. 116, no. 6, p. 061102. Available from DOI: 10.1103/PhysRevLett.116.061102.
- ABBOTT, B. P. et al., 2017b. Multi-messenger Observations of a Binary Neutron Star Merger. *Astrophys. J. Lett.* Vol. 848, no. 2, p. L12. Available from DOI: 10.3847/2041-8213/aa91c9.
- ABBOTT, B. P. et al., 2018. GW170817: Measurements of neutron star radii and equation of state. *Phys. Rev. Lett.* Vol. 121, no. 16, p. 161101. Available from DOI: 10.1103/PhysRevLett.121.161101.
- ABBOTT, B. P. et al., 2019. GWTC-1: A Gravitational-Wave Transient Catalog of Compact Binary Mergers Observed by LIGO and Virgo during the First and Second Observing Runs. *Phys. Rev. X*. Vol. 9, no. 3, p. 031040. Available from DOI: 10.1103/PhysRevX.9.031040.
- ABBOTT, R. et al., 2021a. GWTC-2: Compact Binary Coalescences Observed by LIGO and Virgo During the First Half of the Third Observing Run. *Phys. Rev. X*. Vol. 11, p. 021053. Available from DOI: 10.1103/PhysRevX.11.021053.
- ABBOTT, R. et al., 2020b. GW190814: Gravitational Waves from the Coalescence of a 23 Solar Mass Black Hole with a 2.6 Solar Mass Compact Object. *Astrophys. J. Lett.* Vol. 896, no. 2, p. L44. Available from DOI: 10.3847/2041-8213/ab960f.
- ABBOTT, R. et al., 2021c. GWTC-3: Compact Binary Coalescences Observed by LIGO and Virgo During the Second Part of the Third Observing Run. Available from arXiv: 2111.03606 [gr-qc].

- ABBOTT, R. et al., 2021d. Observation of Gravitational Waves from Two Neutron Star–Black Hole Coalescences. *Astrophys. J. Lett.* Vol. 915, no. 1, p. L5. Available from DOI: 10.3847/2041-8213/ac082e.
- ABBOTT, R. et al., 2021b. GWTC-2.1: Deep Extended Catalog of Compact Binary Coalescences Observed by LIGO and Virgo During the First Half of the Third Observing Run. Available from arXiv: 2108.01045 [gr-qc].
- MAGGIORE, Michele, 2007. *Gravitational Waves. Vol. 1: Theory and Experiments.* Oxford University Press. Oxford Master Series in Physics. ISBN 978-0-19-857074-5, ISBN 978-0-19-852074-0.
- MARGALIT, Ben et al., 2017. Constraining the Maximum Mass of Neutron Stars From Multi-Messenger Observations of GW170817. *Astrophys. J. Lett.* Vol. 850, no. 2, p. L19. Available from DOI: 10.3847/2041-8213/aa991c.
- METZGER, B. D. et al., 2012. What is the Most Promising Electromagnetic Counterpart of a Neutron Star Binary Merger? *Astrophys. J.* Vol. 746, p. 48. Available from DOI: 10.1088/0004-637X/746/1/48.
- MILLER, M. C. et al., 2019. PSR J0030+0451 Mass and Radius from *NICER* Data and Implications for the Properties of Neutron Star Matter. *Astrophys. J. Lett.* Vol. 887, no. 1, p. L24. Available from DOI: 10.3847/2041-8213/ab50c5.
- MILLER, M. C. et al., 2021. *The Radius of PSR J0740+6620 from NICER and XMM-Newton Data.* Available from arXiv: 2105.06979 [astro-ph.HE].
- ABBOTT, B. P. et al., 2017a. Gravitational Waves and Gamma-Rays from a Binary Neutron Star Merger: GW170817 and GRB 170817A. *Astrophys. J.* Vol. 848, no. 2, p. L13. Available from DOI: 10.3847/2041-8213/aa920c.
- MOST, Elias R. et al., 2018. New constraints on radii and tidal deformabilities of neutron stars from GW170817. *Phys. Rev. Lett.* Vol. 120, no. 26, p. 261103. Available from DOI: 10.1103/PhysRevLett.120.261103.
- ARZUMANIAN, Zaven et al., 2018. The NANOGrav 11-year Data Set: High-precision timing of 45 Millisecond Pulsars. *Astrophys. J. Suppl.* Vol. 235, no. 2, p. 37. Available from DOI: 10.3847/1538-4365/aab5b0.
- NEWMAN, Ezra et al., 1962. An Approach to gravitational radiation by a method of spin coefficients. *J. Math. Phys.* Vol. 3, pp. 566–578. Available from DOI: 10.1063/1.1724257.

- OPPENHEIMER, J. R. et al., 1939. On massive neutron cores. *Phys. Rev.* Vol. 55, pp. 374–381. Available from DOI: 10.1103/PhysRev.55.374.
- PEREGO, A. et al., 2021. *Probing the incompressibility of nuclear matter at ultra-high density through the prompt collapse of asymmetric neutron star binaries*. Available from arXiv: 2112.05864 [astro-ph.HE].
- PIRAN, Tsvi et al., 2013. The Electromagnetic Signals of Compact Binary Mergers. *Mon. Not. Roy. Astron. Soc.* Vol. 430, no. 3, pp. 2121–2136. Available from DOI: 10.1093/mnras/stt037.
- POGGIANI, Rosa, 2022. Results from the O3 observing run of the LIGO/VIRGO collaboration. *PoS*. Vol. HEASA2021, p. 060. Available from DOI: 10.22323/1.401.0060.
- PRETORIUS, Frans, 2005. Evolution of binary black hole spacetimes. *Phys. Rev. Lett.* Vol. 95, p. 121101. Available from DOI: 10.1103/PhysRevLett.95.121101.
- RAAIJMAKERS, G. et al., 2021. *Constraints on the dense matter equation of state and neutron star properties from NICER’s mass-radius estimate of PSR J0740+6620 and multimessenger observations*. Available from arXiv: 2105.06981 [astro-ph.HE].
- RADICE, David et al., 2018b. GW170817: Joint Constraint on the Neutron Star Equation of State from Multimessenger Observations. *Astrophys. J. Lett.* Vol. 852, no. 2, p. L29. Available from DOI: 10.3847/2041-8213/aaa402.
- RADICE, David et al., 2019. Multimessenger Parameter Estimation of GW170817. *Eur. Phys. J. A*. Vol. 55, no. 4, p. 50. Available from DOI: 10.1140/epja/i2019-12716-4.
- RADICE, David et al., 2018a. Binary Neutron Star Mergers: Mass Ejection, Electromagnetic Counterparts and Nucleosynthesis. *Astrophys. J.* Vol. 869, no. 2, p. 130. Available from DOI: 10.3847/1538-4357/aaf054.
- RADICE, David et al., 2018c. Long-lived Remnants from Binary Neutron Star Mergers. *Mon. Not. Roy. Astron. Soc.* Vol. 481, no. 3, pp. 3670–3682. Available from DOI: 10.1093/mnras/sty2531.
- READ, Jocelyn S. et al., 2009. Constraints on a phenomenologically parameterized neutron-star equation of state. *Phys. Rev. D*. Vol. 79, p. 124032. Available from DOI: 10.1103/PhysRevD.79.124032.

- REISSWIG, Christian et al., 2011. Notes on the integration of numerical relativity waveforms. *Class.Quant.Grav.* Vol. 28, p. 195015. Available from DOI: 10.1088/0264-9381/28/19/195015.
- REZZOLLA, Luciano et al., 2018. Using gravitational-wave observations and quasi-universal relations to constrain the maximum mass of neutron stars. *Astrophys. J. Lett.* Vol. 852, no. 2, p. L25. Available from DOI: 10.3847/2041-8213/aaa401.
- RILEY, Thomas E. et al., 2019. A *NICER* View of PSR J0030+0451: Millisecond Pulsar Parameter Estimation. *Astrophys. J. Lett.* Vol. 887, no. 1, p. L21. Available from DOI: 10.3847/2041-8213/ab481c.
- RILEY, Thomas E. et al., 2021. *A NICER View of the Massive Pulsar PSR J0740+6620 Informed by Radio Timing and XMM-Newton Spectroscopy*. Available from arXiv: 2105.06980 [astro-ph.HE].
- RUIZ, Milton et al., 2018. GW170817, General Relativistic Magnetohydrodynamic Simulations, and the Neutron Star Maximum Mass. *Phys. Rev. D.* Vol. 97, no. 2, p. 021501. Available from DOI: 10.1103/PhysRevD.97.021501.
- RUSSOTTO, P. et al., 2016. Results of the ASY-EOS experiment at GSI: The symmetry energy at suprasaturation density. *Phys. Rev. C.* Vol. 94, no. 3, p. 034608. Available from DOI: 10.1103/PhysRevC.94.034608.
- SCHWARZSCHILD, Karl, 1916. On the gravitational field of a mass point according to Einstein's theory. *Sitzungsber. Preuss. Akad. Wiss. Berlin (Math. Phys.)* Vol. 1916, pp. 189–196. Available from arXiv: physics/9905030.
- SHIBATA, Masaru et al., 1995. Evolution of three-dimensional gravitational waves: Harmonic slicing case. *Phys. Rev. D.* Vol. 52, pp. 5428–5444. Available from DOI: 10.1103/PhysRevD.52.5428.
- SHIBATA, Masaru, 1999. Fully general relativistic simulation of coalescing binary neutron stars: Preparatory tests. *Phys. Rev. D.* Vol. 60, p. 104052. Available from DOI: 10.1103/PhysRevD.60.104052.
- SHIBATA, Masaru et al., 2000a. Simulation of merging binary neutron stars in full general relativity: Gamma = two case. *Phys. Rev. D.* Vol. 61, p. 064001. Available from DOI: 10.1103/PhysRevD.61.064001.
- SHIBATA, Masaru et al., 2000b. Stability and collapse of rapidly rotating, supramassive neutron stars: 3-D simulations in general relativity. *Phys. Rev. D.* Vol. 61, p. 044012. Available from DOI: 10.1103/PhysRevD.61.044012.

- SHIBATA, Masaru et al., 2003. Merger of binary neutron stars of unequal mass in full general relativity. *Phys. Rev. D*. Vol. 68, p. 084020. Available from DOI: 10.1103/PhysRevD.68.084020.
- SHIBATA, Masaru et al., 2006. Magnetized hypermassive neutron star collapse: A Central engine for short gamma-ray bursts. *Phys. Rev. Lett.* Vol. 96, p. 031102. Available from DOI: 10.1103/PhysRevLett.96.031102.
- SHIBATA, Masaru et al., 2005. Merger of binary neutron stars with realistic equations of state in full general relativity. *Phys. Rev.* Vol. D71, p. 084021. Available from DOI: 10.1103/PhysRevD.71.084021.
- SHIBATA, Masaru et al., 2017. Modeling GW170817 based on numerical relativity and its implications. *Phys. Rev. D*. Vol. 96, no. 12, p. 123012. Available from DOI: 10.1103/PhysRevD.96.123012.
- SHIBATA, Masaru et al., 2019. Merger and Mass Ejection of Neutron-Star Binaries. *Ann. Rev. Nucl. Part. Sci.* Vol. 69, pp. 41–64. Available from DOI: 10.1146/annurev-nucl-101918-023625.
- SPERHAKE, Ulrich, 2015. The numerical relativity breakthrough for binary black holes. *Class. Quant. Grav.* Vol. 32, no. 12, p. 124011. Available from DOI: 10.1088/0264-9381/32/12/124011.
- TAYLOR, J. H. et al., 1982. A new test of general relativity: Gravitational radiation and the binary pulsar PS R 1913+16. *Astrophys. J.* Vol. 253, pp. 908–920. Available from DOI: 10.1086/159690.
- TAYLOR, Joseph H. et al., 1989. Further experimental tests of relativistic gravity using the binary pulsar PSR 1913+16. *Astrophys. J.* Vol. 345, pp. 434–450. Available from DOI: 10.1086/167917.
- ABBOTT, Benjamin P. et al., 2017c. GW170817: Observation of Gravitational Waves from a Binary Neutron Star Inspiral. *Phys. Rev. Lett.* Vol. 119, no. 16, p. 161101. Available from DOI: 10.1103/PhysRevLett.119.161101.
- THIERFELDER, Marcus et al., 2011. Numerical relativity simulations of binary neutron stars. *Phys. Rev.* Vol. D84, p. 044012. Available from DOI: 10.1103/PhysRevD.84.044012.
- TICHY, Wolfgang, 2006. Black hole evolution with the BSSN system by pseudo-spectral methods. *Phys. Rev.* Vol. D74, p. 084005. Available from DOI: 10.1103/PhysRevD.74.084005.

- TICHY, Wolfgang, 2009a. A New numerical method to construct binary neutron star initial data. *Class.Quant.Grav.* Vol. 26, p. 175018. Available from DOI: 10.1088/0264-9381/26/17/175018.
- TICHY, Wolfgang, 2009b. Long term black hole evolution with the BSSN system by pseudo-spectral methods. *Phys.Rev.* Vol. D80, p. 104034. Available from DOI: 10.1103/PhysRevD.80.104034.
- TICHY, Wolfgang et al., 2019. Constructing binary neutron star initial data with high spins, high compactnesses, and high mass ratios. *Phys. Rev. D.* Vol. 100, no. 12, p. 124046. Available from DOI: 10.1103/PhysRevD.100.124046.
- TOOTLE, Samuel D. et al., 2021. *Quasi-universal behaviour of the threshold mass in unequal-mass, spinning binary neutron-star mergers.* Available from arXiv: 2109.00940 [gr-qc].
- WEISBERG, J. M. et al., 2010. Timing Measurements of the Relativistic Binary Pulsar PSR B1913+16. *Astrophys. J.* Vol. 722, pp. 1030–1034. Available from DOI: 10.1088/0004-637X/722/2/1030.
- YORK Jr., James W., 1978. Kinematics and Dynamics of General Relativity. In: *Workshop on Sources of Gravitational Radiation*, pp. 83–126.
- ZHAO, Tianqi et al., 2022. Universal Relations for Neutron Star F-Mode and G-Mode Oscillations. Available from arXiv: 2204.03037 [astro-ph.HE].

Publications

- [Koe1] KÖLSCH, Maximilian et al., 2022. Investigating the mass-ratio dependence of the prompt-collapse threshold with numerical-relativity simulations. *Phys. Rev. D*. Vol. 106, no. 4, p. 044026. Available from DOI: [10.1103/PhysRevD.106.044026](https://doi.org/10.1103/PhysRevD.106.044026).

Acknowledgements

I am grateful to Prof. Bernd Brügmann for giving me the opportunity to write my thesis in his group, and for his support during the last years. I appreciated the opportunities to continue exploring the world of physics, and to take part in the group's teaching efforts, which allowed me to deepen my understanding of theoretical physics.

I especially thank Prof. Tim Dietrich for suggesting to conduct a small number of simulations with the goals to make first steps with BAM, and to study mass ratio effects on threshold mass to prompt collapse. As it turned out this was the beginning of a scientific journey that led to hundreds of more simulations and this thesis. I am grateful to him for advising me on this journey, for the fastest reactions to emails even at late times, for regular zoom meetings together with my supervisor and me, and for being a very careful reader. This brings me to Prof. Maximiliano Ujevic Tonino who joined these meetings. I am grateful to him for many helpful discussions, very informative answers, especially when responding to technical questions, and for always being positive.

Of course I should not forget to thank all of my colleagues, who I shared parts of the way and many group meetings with. There are Hannes Rüter and Sarah Renkhoff, who to me were office mates, room mates on the DPG Frühjahrstagung, and fellow tutors. There are Francesco Fabbri, Reetika Dudi, and Vivek Chaurasia who together with Hannes and Sarah welcomed me into the group when I started, and there are Daniela Cors, Ondrej Zelenka, Florian Atteneder, and Roxana Rosca-Mead, who I was allowed to welcome to the group and to Jena. I am thankful for many interesting conversations, help with work-related topics, and shared recreational activities. In this context I want to thank Sarp Akcay for his relentless motivation to pursue our shared hobby, and for motivating me and others to join him. I thank my fellow tutors for interesting discussions and a constructive working climate. In particular, I thank Daniela for being a reliable and motivated partner in our shared endeavour to prepare problem sheets for the GR exercises.

Thinking about the many simulations that I conducted on the ARA cluster, I very much appreciate the help with related problems that I received from Andre Sternbeck.

I am grateful to Wolfgang Tichy for giving me access to SGRID, and for adding a feature to SGRID that made my work a lot easier.

Without the support, patience and love of my partner Chantal Sundqvist and our children, this work would not have been possible. Together we have steered through the challenges that came with the COVID-19 pandemic. I am deeply grateful to them. I am also grateful to my family and my friends. Though many of them do not live close by, they have been and are important to me.

Last, but not least, I thank Chantal, Daniela, and Tim for proofreading this thesis (or parts of it).

Additional Material

Talks

- DPG-Frühjahrstagung SMuK 2021: *Prompt Collapse in Binary Neutron Star Mergers: The Effect of the Mass Ratio*
- DFG-RTG2522 Monitoring Workshop Jena-Leipzig 2021: *Prompt Collapse in Binary Neutron Star Mergers: The Effect of the Mass Ratio*

Conferences and Workshops

- 12.02.2018-16.02.2018 Parallele Programmierung mit MPI und OpenMP, HLRS, Dresden
- 19.02.2018-19.02.2018 Computational Fluid Dynamics, HLRS, Siegen
- 19.03.2018-23.03.2018 DPG-Frühjahrstagung 2018, Würzburg
- 27.09.2021-29.09.2021 DFG-RTG2522 Monitoring Workshop Jena-Leipzig
- 30.08.2021-03.09.2021 DPG-Frühjahrstagung SMuK 2021 (online)

Zusammenfassung

Da beschleunigte Massen gemäß allgemeiner Relativitätstheorie Energie in Form von Gravitationswellen abstrahlen, verringert sich der Abstand massereicher Objekte in Binärsystemen bis diese schließlich kollidieren und verschmelzen. Dieser Verschmelzungsprozess wird, neben weiteren Faktoren, primär durch die Gesamtmasse des Doppelsterns und seine Masseverteilung bestimmt. Besteht ein solches Doppelsternsystem aus zwei Neutronensternen, also aus den dichtesten uns bekannten Objekten im Universum, so wird der Verschmelzungsprozess, anders als bei binären schwarzen Löchern, zudem von den Eigenschaften hochdichter Materie beeinflusst. Da Neutronensterne hinsichtlich ihrer Stabilität eine maximale Masse besitzen, stellt sich die Frage, ob auch das Produkt einer solchen Verschmelzung wieder ein Neutronenstern ist, ob dieser stabil ist, beziehungsweise wie viel Zeit zwischen Verschmelzung und dem Kollaps zu einem schwarzen Loch vergeht (Kollapszeit). In diesem Zusammenhang ist die sogenannte *threshold mass to prompt collapse* M_{thr} , also die Grenzmasse für welche alle massereicheren Verschmelzungsprodukte zweier Neutronensterne direkt zu einem schwarzen Loch kollabieren, eine charakteristische Größe.

Die vorgelegte Dissertationsarbeit beschäftigt sich mit dem Einfluss des Masseverhältnisses q der Komponenten eines Doppelsternsystems von Neutronensternen auf diese Grenzmasse, auf die Kollapszeit und auf Eigenschaften des entstehenden Systems, welches aus einem rotierenden schwarzen Loch und einer Aggregationsscheibe besteht. Die dargelegten Untersuchungen beruhen auf 335 allgemeinrelativistischen Simulationen von 165 Doppelsternkonfigurationen bestehend aus nichtrotierenden Einzelsternen unterschiedlicher Masseverhältnisse und Gesamtmassen. Für die dynamische Simulationen wurde dabei der BAM-Code verwendet, für die Konstruktion der Anfangsdaten wurde der SGRID-Code verwendet. Es wurden drei unterschiedliche Zustandsgleichungen für die Modellierung dichter Materie verwendet und sieben Masseverhältnisse von $q = 1.0$ bis $q = 1.75$ untersucht. Der durch Zustandsgleichungen und Masseverhältnisse aufgespannte Parameterraum umfasst daher 21 Fälle, in denen jeweils fünf bis sieben Gesamtmassen aus angepassten Masseintervallen untersucht worden sind –

jeweils mit dem Ziel, dass sowohl Konfigurationen enthalten sind, welche zu unverzüglichem Kollaps führen, als auch solche für die der Kollaps verzögert eintritt. Diese Untersuchung umfasst 295 dieser Simulationen, wobei für Fehlerabschätzungen typischerweise wenigstens zwei numerische Auflösungen je Konfiguration simuliert worden sind. Mittels der übrigen 40 Simulationen wurde einer der durch Zustandsgleichung und Masseverhältnis beschriebenen Fälle näher untersucht, um den steilen Abfall der Kollapszeitkurve im Bereich der Grenzmasse aufzulösen. Dabei ergab sich aus der großen Anzahl der Simulationen die Notwendigkeit der automatisierten Aufbereitung der Simulationsdaten, für welche ein passendes Workframe entwickelt worden ist.

Eine stichhaltige Analyse der Daten verlangt Klarheit hinsichtlich der verwendeten Definitionen, Kriterien und Methoden. Daher ist der Auswertung der Daten eine detaillierte Diskussion der wichtigsten Größen und Eigenschaften hinsichtlich zugehöriger Definitionen und Methoden für ihre Bestimmung im Kontext numerischer Simulationen, vorangestellt. Unverzüglicher und verzögerter Kollaps lassen sich beispielsweise mit Blick auf die Minimalwerte des Lapse beziehungsweise die Maximalwerte der Dichte auseinanderhalten. In beiden Fällen bezieht sich das Kriterium auf die Existenz von Extrempunkten im Zeitintervall zwischen dem Beginn der Verschmelzung und dem Kollaps zum schwarzen Loch. Alternativ lässt sich die Unterscheidung allein unter Betrachtung der Kollapszeit im Vergleich zu einem Grenzwert vornehmen. Ein entsprechendes Verfahren und ein Wert für diesen Grenzwert wurden in dieser Arbeit auf Grundlage der bestehenden Kriterien, der großen Zahl an Simulationen und der gewonnenen Erkenntnisse über den Verlauf der Kollapszeitkurve motiviert. Weiterhin wurde eine empirisch motivierte Fitfunktion entwickelt, um die Grenzmasse zu unverzüglichem Kollaps mittels Interpolation zu bestimmen. Unter Verwendung des detailliert untersuchten Falles wurde diese Methode im Vergleich zur sogenannten Freifallmethode von Köppel et al., 2019, und im Vergleich zur Methode der Intervallschachtelung diskutiert. Ein Vorteil der hier genannten Methode ist die Betrachtung eines vergleichsweise breiten Gesamtmasseintervalls. Methoden, die auf Datenpunkten dicht an der Grenzmasse beruhen, zeichnen sich hingegen durch größere Verlässlichkeit aus.

Die Analyse der Grenzmasseresultate hinsichtlich ihrer Abhängigkeit vom Masseverhältnis zeigte, dass M_{thr} sich nicht monoton mit q ändert. In allen untersuchten Fällen nahm die Grenzmasse im Bereich hoher Masseverhältnisse ab, bei intermediären Werten von q erreicht $M_{\text{thr}}(q)$ ein Maximum. Diese Entdeckung steht im Kontrast zu Modellen von Bauswein et al., 2021, welche auf Untersuchungen eines schmaleren

Intervalls von Masseverhältnissen beruht. Unter Hinzufügen linearer Terme wurde das Modell von Bauswein et al., 2021, angepasst und sowohl auf Daten, die dieser Arbeit zugrunde liegen, angewendet, als auch auf kombinierte Datensätze unter Verwendung von Resultaten von Bauswein et al., 2021, und Perego et al., 2021. Auf diese Weise wurde eine größere Anzahl an Zustandsgleichungen berücksichtigt. Weiterhin wurden auf Grundlage der Grenzmasseresultate Gezeiteigenschaften von Grenzkonfigurationen bestimmt. Durch die Modellierung ihrer Abhängigkeit vom Masseverhältnis konnte ein Modell von Bernuzzi, 2020, verbessert werden, welches sich durch konstante Obergrenzen für Gezeitenparameter auszeichnet.

Die Eigenschaften des aus dem Verschmelzungsprozess hervorgehenden Systems aus Aggregationsscheibe und rotierendem schwarzen Loch hängen stark von den dynamischen Prozessen während des Aufeinandertreffens der Neutronensterne ab. Dies gilt insbesondere in Fällen, in denen das Verschmelzungsprodukt unverzüglich zu einem schwarzen Loch kollabiert. Im Fall asymmetrischer Masseverteilungen spielen Gezeitenkräfte eine entscheidende Rolle, welche umso größer ausfallen, je größer das Masseverhältnis ist. Dies umfasst starke Verformungen der weniger massereichen Komponente des Doppelsterns bis hin zum Zerreißen der sekundären Komponente im Fall extremer Masseverteilungen. Entsprechend sind für hohes q massereichere Aggregationsscheiben zu erwarten. Dies deckt sich mit den Simulationsresultaten, welche für den Fall unverzüglichen Kollapses gewonnen worden sind. Kollabiert das Verschmelzungsprodukt mit Verzögerung, so sind über die Zeitspanne bis zum Kollaps weitere Prozesse am Werk, die zum Auswurf von Materie und damit zur Anreicherung von Materie in der Aggregationsscheibe führen. Masse und Rotation des entstehenden schwarzen Loches verhalten sich dazu hinsichtlich des Einflusses des Masseverhältnisses, erwartungsgemäß, entgegengesetzt. Effekte des Masseverhältnisses auf die Masse der entstehenden Aggregationsscheibe, die Masse des schwarzen Loches und seiner Rotation wurden in Form von Ober- beziehungsweise Untergrenzen abgeschätzt und modelliert.

Codes Employed or Adapted for this Work

- BAM [Bernuzzi et al., 2016a; Dietrich et al., 2015b; Thierfelder et al., 2011; Brügmann et al., 2008]
- SGRID [Tichy et al., 2019; Dietrich et al., 2015a; Tichy, 2009b; Tichy, 2009a; Tichy, 2006]
- Matlab script by Sebastiano Bernuzzi and Alessandro Nagar to solve TOV equations in GR [Bernuzzi et al., 2008; Damour et al., 2009], <https://bitbucket.org/bernuzzi/tov/src/master/>
- Python script by Tim Dietrich to post-process BAM's $r\Psi_4$ -output (unpublished)
- Python script by Wolfgang Tichy to compute the eccentricity of a BNS, <https://www.physics.fau.edu/~wolf/Research/EccRed/index.html>

Selbstständigkeitserklärung

Ich erkläre hiermit ehrenwörtlich, dass ich die vorliegende Arbeit selbstständig, ohne unzulässige Hilfe Dritter und ohne Benutzung anderer als der angegebenen Hilfsmittel und Literatur angefertigt habe. Die aus anderen Quellen direkt oder indirekt übernommenen Daten und Konzepte sind unter Angabe der Quelle gekennzeichnet.

Bei der Auswahl und Auswertung dieser Arbeit haben mir die nachstehend aufgeführten Personen in beratender Weise unentgeltlich geholfen:

- Prof. Bernd Brüggemann
- Prof. Tim Dietrich
- Prof. Maximiliano Ujevic

In Bereichen, bei denen auf Arbeit anderer zurückgegriffen wurde, ist dies ausdrücklich in der Arbeit erwähnt. Weitere Personen waren an der inhaltlich-materiellen Erstellung der vorliegenden Arbeit nicht beteiligt. Insbesondere habe ich hierfür nicht die entgeltliche Hilfe von Vermittlungs- bzw. Beratungsdiensten (Promotionsberater oder andere Personen) in Anspruch genommen. Niemand hat von mir unmittelbar oder mittelbar geldwerte Leistungen für Arbeiten erhalten, die im Zusammenhang mit dem Inhalt der vorgelegten Dissertation stehen. Die Arbeit wurde bisher weder im In- noch im Ausland in gleicher oder ähnlicher Form einer anderen Prüfungsbehörde vorgelegt. Die geltende Promotionsordnung der Physikalisch-Astronomischen Fakultät ist mir bekannt.

Ich versichere ehrenwörtlich, dass ich nach bestem Wissen die reine Wahrheit gesagt und nichts verschwiegen habe.

Jena, 01.11.2022

Unterschrift